# Topics of Magnetic Field and Turbulence in Star Formation

## 恆星誕生中的湍流與磁場

**TANG, Kwok Sun**

**鄧國燊**

A Thesis Submitted in Partial Fulfilment
of the Requirements for the Degree of
Master of Philosophy
in
Physics

The Chinese University of Hong Kong
September 2016

## Thesis Assessment Comittee

Professor CHU, Ming Chung (Chair)

Professor LI, Hua Bai (Thesis Supervisor)

Professor LI, Gunag Feng Tjoonie (Committee Member)

Professor LIM, Jin Leong Jeremy (External Examiner)

Abstract of thesis entitled:

Topics of Magnetic Field and Turbulence in Star Formation

Submitted by TANG, Kwok Sun

for the degree of Master of Philosophy

at The Chinese University of Hong Kong in September 2016

# 摘要

不論考慮巨型分子雲或原恆星盤的形成，磁流體湍流對於理解恆星形成發揮重要的作用。在第一章中，我們概述磁場和湍流的基本特性。在第二章中，我們提出對密集的分子雲的“偏振洞”現象解釋。利用詹姆斯克拉克麥克斯韋望遠鏡和毫米波天文組合陣研究望遠鏡偏振數據庫，我們嘗試解釋在密集的分子雲觀察到的低熱塵埃偏振比率是由湍流引致而無法被解析的磁場結構。由干涉儀望遠鏡觀察到高偏振率的現象，我們排除了塵埃在密集的分子雲對齊能力降低假説。在第三章，我們呈上最近對貓掌星雲氰化氫($HCN$)/羧甲基正離子($HCO^+$) $J = 4 - 3$ 的觀察。配合李氏等人在不同尺度和密度測量的磁場强度，我們對雙極擴散理論進行測試。我們的分析發現，離子（羧甲基正离子）和中性粒子（氰化氫）的平方速度彌散差異與磁場强度成正比。運用速度坐標頻譜方法，我們求出離子和中性粒子的湍流能譜。最佳擬合參數顯示，當尺度小於0.48秒差距，離子湍流能譜表現出明顯衰減。這是雙極擴散的直接證據。最後，我們提出利用氰化氫與羧甲基正離子的湍流能譜測量磁場强度方法。

# Abstract

Turbulence and magnetic fields are ubiquitous in the context of star formation, ranging from the formation of GMCs to the formation of proto-stellar discs. Magnetohydrodynamic (MHD) turbulence is expected to play an important role to the understanding of star formation. In chapter 1, we give an overview on magnetic fields and turbulence. We try to understand the phenomenon 'polarization hole' in dense molecular clouds in chapter 2. With the data archives from JCMT and CARMA, we interpret the low thermal dust polarization fraction in dense molecular clouds as the consequence of unresolved magnetic field structures induced by turbulence. The high polarization ratio observed by interferometer ruled out the commonly put-forward explanation that attribute 'polarization hole' to the shut down of grain alignment in dense regions (e.g. Padoan et al. (2001)). In chapter 3, we present our recent observation of $HCN/HCO^{+}(4-3)$ towards a massive star forming filament NGC6334, where B-field strength had been measured at regions of different scales (1pc, 0.1pc, 0.01pc) and density ($10^{3}-10^{5}cm^{-3}$) before by Li et al. (2015). It is an ideal testing ground on the theory of turbulent ambipolar diffusion Li &

Houde (2008). Our analyses demonstrate that the difference of squared Velocity Dispersion (VD) between ions ($HCO^+$) and neutrals ($HCN$) is positively correlated with B-field strength, reinforcing the validity of the explanation put forward by Li & Houde (2008) and Li et al. (2010). The turbulent energy spectrum of ions and neutrals would be derived with the velocity coordinate spectrum Lazarian & Pogosyan (2006). The best fit parameters show that ions demonstrated a steeper decay in turbulent energy for scales smaller than $L_{AD} \sim 0.484pc$. This is a direct evidence of turbulent ambipolar diffusion in action. We finally present a recipe for measuring B-field strengths with turbulent energy spectra we derived for $HCN$ and $HCO^+$.

# Acknowledgement

I would like to thank my advisor, Prof. Hua-Bai Li, for his support and encouragement during these years. I am extremely grateful that he maintains a confidence-building approach while inspiring me at the same time with his creative, yet careful way of being a good scientist. One could hardly ask for a better supervisor. I would also like to thank Dr. Po Kin Leung and Dr. Frank Otto for responding my queries on science and advice on academic career paths. I thank Dr. Wing-Kit Lee for his sage comments on my telescopes proposals and scientific writing. It would be remiss of me not to express my gratitude to the graduate students: Ya Peng Zhang, Ka Ho Yuen, Kenny Lau, Chi Yan Law from our star formation research group. I am especially indebted to Kenny Lau for his time on debugging my python codes. Completing this work would have been impossible were it not for the support provided by my parents and brothers who experienced the ups and downs of my research.

# Contents

# List of Figures

# List of Tables

# Chapter 1

# Introduction

Stars form in cold, dense molecular clouds. Gravity is responsible for gathering gas into self-gravitating structures. Free-fall time $t_{ff}$ is a characterisitc time that a body takes during the collapse under its own gravitational attraction in the absence of other supporting force.

$$t_{ff} = \sqrt{\frac{3\pi}{32G\rho}} = \frac{4.4 \times 10^4 yr}{\sqrt{n_H/10^6 \mathrm{cm}^{-3}}} \tag{1.1}$$

where $n_H$ is the number density of hydrogen atom. The total mass of molecular gas in the Milky Way is $\sim 10^9 M_\odot$. Assuming a number density of $n_H \approx 50\mathrm{cm}^{-3}$, the free-fall time would be of the order $t_{ff} \approx 6 \times 10^6 \mathrm{yr}$ (Draine, 2011). This would give a star formation rate of:

$$\dot{M}_{ff} = \frac{M}{\tau_{ff}} \approx 200 \mathrm{M}_\odot \mathrm{yr}^{-1} \tag{1.2}$$

Star formation rate of our Milky Way galaxy is $1.3 \pm 0.2 \mathrm{M}_{\odot} \mathrm{yr}^{-1}$ (Murray & Rahman, 2010) and is 2 orders of magnitude smaller than the one we estimated above. This suggests that most of the mass in molecular clouds are not undergoing free-fall collapse. Mechanisms other than thermal support must be taken into account in order to understand the observed star formation rate.

For a long time, magnetic fields were thought to be the source that counterarcts the gravitioanl contraction. The importance of magnetic fields to the self gravity of the cloud structure is determined by the relative importance of the magnetic energy and the gravitational energy. The magnetic critical mass $M_{\phi}$ is defined to be:

$$M_{\Phi} = c_{\Phi} \frac{\Phi}{G^{1/2}} \tag{1.3}$$

where $\Phi$ is the magneitc flux, $G$ is the gravitational constant, $c_{\Phi}$ is a coefficient which depends on the geometry and density distribution of the cloud respectively. The standard theory assumes clouds are initially subcritical in mass ($M < M_{\Phi}$) where magnetic fields dominates over the self gravity. Star formation proceeds only after the diffusion/drift of neutral species through the charged particles. Magnetic flux would be left behind in the envelope. This effectively lowers the $M_{\Phi}$ of the cloud cores.

Gravitational collapse continues when the $M > M_\Phi$. This process is termed Ambipolar Diffusion, coined by Mestel & Spitzer (1956). Tassis & Mouschovias (2004) predicts a timescale of about $10Myr$. Apart from magnetic fields, supersonic turbulence is thought to play a dual role in regulating star formation McKee & Ostriker (2007). On one hand, it creates overdense regions to initiate gravitational collapse. On the other hand, it provides supports to counteract the effect of gravity. Turbulence naturally explains many observed density and velocity structures in molecular clouds. Studying the interplay between magnetic fields and turbulence is therefore essential to understanding the processs of star formation.

## 1.1 Magnetohydrodynamics in weakly ionized media

Here I will review some basic equations and properties for weakly ionized and magnetized fluids. In dense molecular clouds, ultraviolet star light would be insufficient to photoionize elements Draine (2011). Only a very small ionization fraction (e.g., $\zeta = n_e/n_H \approx 10^{-7}(10^4 cm^{-3}/n_H)^{1/2}$) in molecular clouds is maintained by the ionization from cosmic rays. Since Lorentz force

only acts upon ionized species, one might expect magnetic field might not take part in the dynamics of molecular clouds. To get a rough idea on the magnetic field-plasma coupling, we can compare the timescale that governs the dyanmics of ions and neutrals. The gyration frequency of the ions is given by $\omega = qB/mc$ where $q$ is the charge of the species, $B$ is magnetic field strength, $m$ is the mass of the species and $c$ is the speed of light. The collision frequency of ions with neutrals is given by $\omega_{in} = n < \sigma v >$ where n is the number density of the neutrals, $< \sigma v > \approx 1.9 \times 10^{-9}\mathrm{cm}^3\mathrm{s}^{-1}$ is the collision rate between ions and neutrals. For typical conditions in molecular clouds ($n = 10^4\mathrm{cm}^{-3}; \mathrm{B} = 50\mu\mathrm{G}$ Draine (2011)), $(\omega/\omega_{in})_{|electron} \approx 10^7; (\omega/\omega_{in})_{|ions} \approx 10^3 >> 1$. This suggests that plasmas are still well-coupled to the magnetic fields. Neutrals experience the influence of magnetic fields indirectly through their collisions /frictional force with the ions.

### 1.1.1 Governing equations

Consider a partially ionized gas with magnetic field $B$, the momentum equation for the plasmas (subscript p) and neutrals

(subscript n) can be written as

$$\rho_p(\frac{\partial u_p}{\partial t} + u_p \cdot \nabla u_p) = -\nabla P_p + \frac{J \times B}{c} + \rho_p g - \rho_p \rho_n \gamma_{pn}(u_p - u_n)$$
$$\rho_n(\frac{\partial u_n}{\partial t} + u_n \cdot \nabla u_n) = -\nabla P_n + \rho_n g + \rho_p \rho_n \gamma_{pn}(u_p - u_n) \tag{1.4}$$

where $\rho_i$, $u_i$, and $P_i$ are density, velocity, and pressure of $i$-th species, respectively, $J$ is the current density, $g$ is the gravitational acceleration, and $\gamma_{pn} =< \sigma v >_{in} /(m_i + m_n)$ is the collision rate coefficient Zweibel (2015). Here we approximate the electrons to have neglible inertia such that they are moving with the ions and keeping the overall fluid electrically neutral.

### 1.1.2 Flux Freezing

On large length scales, the plasma and neutrals are well coupled to each other. We can start by estimating the relative/drift velocity between plasmas and neutrals $u_D = u_p - u_n$. Assuming the plasma inertia is neglible, the balance of Lorentz force and the ion-neutral collision friction would hence give:

$$u_D = \frac{J \times B}{\rho_p \rho_n \gamma_{pn} c} = \frac{(\nabla \times B) \times B}{4\pi \rho_p \rho_n \gamma_{pn} c} \tag{1.5}$$

where in the last step we used the Ampere's Law.

This characteristic drift velocity is important in defining dif-

ferent regimes. The induction equation is given by:

$$\frac{\partial B}{\partial t} = -c(\nabla \times E) \tag{1.6}$$

where $E$ is the electric field. To relate the plasma equations to Maxwell equations, Ohm's law which states that the electric field in the comoving frame of plasma $E'$ is proportional to resistivity $\eta$ times current density $j$, is required:

$$E' = \eta j = E + \frac{u_p \times B}{c} \tag{1.7}$$

Since $\eta$ is small for astrophysical medium, $E$ can be eliminated from the induction equation with ohm's law (e.g., $E \sim -\frac{u_p \times B}{c}$):

$$\begin{aligned} \frac{\partial B}{\partial t} =& \nabla \times (u_p \times B) \\ =& \nabla \times (u \times B) + \nabla \times (u_D \times B) \end{aligned} \tag{1.8}$$

where $u$ corresponds to the center of mass velocity. Consider a surface $S$ defined by the normal $\hat{n}$, the magnetic flux threading $S$ at time t is

$$\Phi(t) = \int B \cdot \hat{n} dS \tag{1.9}$$

Differentiating the above equation and with the help of the induction equation, we arrive at:

$$\frac{d\Phi}{dt} = \int B \cdot (u_D \times dl) \tag{1.10}$$

This shows that the magnetic flux is changing at a rate depending on $|u_D|$. When drift velocity is small, flux freezing ($\frac{d\Phi}{dt} \approx 0$)

would be a good approximation. This gives a more intuitive understanding on the plasma equations. As the plasma moves, it drags the field lines along with it. Studying how the fluids flow would get us a glimpse of the magnetic fields. Under flux-freezing condition, the two fluids can be treated as an single fluid by adding the momentum equation of plasmas and neutrals:

$$\begin{aligned} \rho(\frac{\partial u}{\partial t} + u \cdot \nabla u) =& \nabla P + \frac{J \times B}{c} + \rho g \\ \frac{\partial B}{\partial t} =& \nabla \times (u \times B) \end{aligned} \tag{1.11}$$

These sets of equations are called the strong coupling approximation where plasmas and neutrals follow almost the same dynamics. The interaction between ions and neutrals comes from the last frictional term while only ions feel the magnetic fields. The single fluid description is a good approximation when timescale longer than ion-neutral collision time is considered.

## 1.2 Turbulence

### 1.2.1 Size-Linewidth relation

Larson (1981) discoverd that the velocity dispersion of molecular clouds can be well-described the relation:

$$\Delta v \approx 1.1 kms^{-1} (\frac{l}{1pc})^{0.38} \tag{1.12}$$

where $l$ is the size of the cloud. Larson noted that this power-law index is consistent with the Kolmogorov theory for incompressible turbulent cascade. Turbulence is therefore not negligible in understanding molecular clouds.

### 1.2.2 Statistics of Turbulence

The classical theory from Kolmogorov (1941) has achieved great success in describing incompressible turbulent flows. It predicts the self-similarity of turbulent flows over a range of scales, e.g., inertial range. Kolmogorov envisaged the energy flux is independent of the size of the eddies for scales larger than the dissipation scale. In the inertial range $l$ where $l_{drive} >> l >> l_{diss}$, ($L_{drive}$ is the drving scale of turbulence and $L_{diss}$ is the turbulent dissipation scale) the behavior of eddies of size $l$ is independent of viscosity as the shear stress is very weak for $l >> l_{diss}$. The energy transfer rate between larger eddies to smaller eddies $\epsilon$ is assumed to be conserved and equal to the energy dissipation rate. By dimentional analyses, it has the form of $\epsilon = u(l)^2/\tau(l)$ where $u$ is the characteristic velocity of eddies with size $l$ and $\tau(l)$ is the eddy turnover time. This eventually predicts a scaling of $u(l) \approx (\epsilon l)^{1/3}$ and energy spectrum $P(k) \sim E/k \sim u^2/k \propto k^{-5/3}$.

### 1.2.3 Magnetized turbulence

Strong magnetic field (i.e. $V_A >> v(l)$ where $V_A$ is the Alfven wave speed) introduces a preferential direction to the magneized system. Considering a mdeium filled with Alfven waves, Goldreich & Sridhar (1995) introduced the idea of critical balance to describe strong MHD turbulence which postulates that the nonlinear time at which energy transferred to smaller scale $t_\perp \approx l_\perp/v_\perp$ is comparable to the wave propagation time along the magnetic field $t_{||} \approx l_{||}/v_A$, e.g., $k_{||}v_A \approx k_\perp v_\perp$. As counter-propagating waves interact, the energy cascades more rapidly along the lateral direction $k_\perp$ than along the parallel direction $k_{||}$ The cascading rate is given by $v(l_\perp)^3/l_\perp \sim$ constant. This gives a relation $k_{||} \propto k_\perp^{2/3}$. Eddies become more elongated along the direction of the local magnetic field. However, it is still debatable whether such anisotropy would remain observable in the global frame of reference.

## 1.3 Observing Dust Polarization

Magnetic fields leave its trail on the polarized interstellar radiations. Sub-millimeter thermal dust emission is a powerful probe that reveals the morphology of magnetic fields in inter-

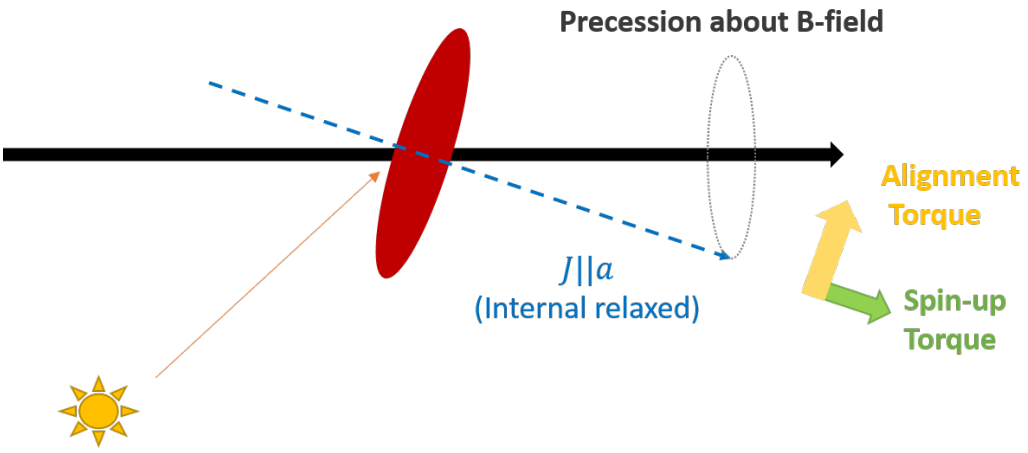


Figure 1.1: Demonstration of the alignment of the dust grains with magnetic fields in the presence of radiative torques. The state when the angular momentum axis $J$ coincides with the magetic fields direction is a stationary point where the alignment torque averaged out.

stellar clouds and cores. One of the main assumptions is that spinning dust grains are aligned with their shorter axis parallel to the magnetic fields.

An extensive review on interstellar dust grain alignment theories can be found in Andersson et al. (2015). Radiative alignment torque, proposed by Dolginov & Mitrofanov (1976) and extended by Lazarian & Hoang (2007), is currently the most widely accepted theory for aligning interstellar dust grains with ambient magnetic fields.

In order to generate significant polarization, the angular momentum of the grains has to be alignend with the axis of max-

imum moment of inertia (usually is the shorter axis of the grains $a$), and the ambient magnetic field direction. Spinning dust grains accquire its magnetic moment through Barnett effect. The magnetization caused by Barnett effect would be continually reoriented as the grains spin. This will lead to a dissipation of energy in the forms of heat at the expense of rotational energy. Meanwhile, the total angular momentum of the grains system would conserve when some of the macroscopic (mechanical) angular momentum of the dust grains transferred to the spin systen by turning some electron spins over. This process is termed 'internal relaxation' (Purcell (1979); Lazarian & Hoang (2007)) and is responsible for aligning the angular momentum of grains about their shorter axes $a$. The shorter axes of the grains eventually undergo Larmor precession about the magnetic fields.

Radiative torque alignment is believed to the dominant mechanism for aligning dust grains. It originates from the assumption that dust grains are spheriods with net helicities (e.g., the differential extinction cross section for incidental left hand polarized and right hand polarized components of light.) The anisotropic radiation can spin the grains up to suprathermal velocities, making them less sensitive to the thermal gas bombardments. Apart from spinning up the grains, these radiative alignments torque

tends to align the angular momentum axis $J$ with the external magnetic field direction. According to Lazarian (2009), radiative torque can be decomposed to two components $H$ and $F$, with $H$ being the spin-up torque parallel to the grain momentum $J$, and $F$ being the alignment torque acting perpendicular to $J$ . Since $F$ is perpendicular to $J$, the alignment torque would be averaged out over the grains' Lamor precession period when $J$ lies closer and closer to being parallel to magnetic field. The case when $B$ lies parallel to $J$ is therefore a stationary point of this grains system. However, detailed calculation is required to determine the exact dynamics of the dust grains under external radiative torques (Purcell (1979); Lazarian & Hoang (2007); Andersson et al. (2015)).

Chandrasekhar & Fermi (1953) proposed a method to estimate magnetic field strength with interstellar polarization. The idea starts with considering a fluid filled with Alfven waves. The wave velocity of Alfven waves is given by:

$$V_A = \frac{B}{\sqrt{4\pi\rho}} \tag{1.13}$$

The transverse motion of these Alfven waves takes a simple wave form:

$$y = a \times cos[k(x - V_A t)] \tag{1.14}$$

where $k$, $y$, $x$ are the wavenumber, the lateral displacement of

the line of force and $x$ is the wave propagation direction respectively. This line of force follows the wave equation:

$$\begin{aligned} V_A^2\overline{y'^2} =& \overline{\dot{y}^2} \\ y' =& \frac{dy}{dx} = \delta\phi \\ \dot{y} =& \frac{dy}{dt} = \delta v \end{aligned} \tag{1.15}$$

The lateral velocity of the line of force $\dot{y}$ is equal to the turbulent velocity of the gas lateral motions $v$ assuming the magnetic field structures are induced by the turbulent gas motion. The term $y'$ corresponds to the dispersion of the magnetic field direction on the plane of sky $\delta\phi$. Rearranging the terms in the above equation, we arrive at the conclusion from Chandrasekhar & Fermi (1953):

$$B = \sqrt{4\pi\rho}\frac{\delta v}{\delta\phi} \tag{1.16}$$

It is found to be a suprisingly good estimate when applying to numerical simulations. A correction factor of unity order has been proposed by Ostriker et al. (2001); Falceta-Gonçalves et al. (2008) to account for the anisotropies in velocity, inhomogenity of the density distribution and etc.

## 1.4 Outline of the thesis

In Chapter 2, we study polarization data from different scale and try to understand the low polarization fraction observed in cloud cores as a consquence of the interaction between magnetic fields and turbulence. In Chapter 3, we present our observation towards NGC 6334. We find evidence of the decoupling of the neutral flows from magnetic fields, and we present a recipe for estimating the magnetic field strength in molecular clouds with the turbulent energy spectrum of ions and neutrals.

---

□ **End of chapter.**

# Chapter 2

# Understanding Polarization Hole

Probing deeper into higher density region, thermal emission from dust grains usually show a lower degree of polarization comparing to the outskirt of the cloud with single dish telescope. It is often termed as 'polarization hole' (e.g. Girart et al. (2006); Li et al. (2009a); Liu et al. (2013)). One common explanation is that dust alignment efficiency decreases with increasing density. For example, Padoan et al. (2001) suggested dust grains are no longer aligned when $A_v > 3mag$. With the polarization data archives from CARMA and JCMT, we show that their proposal is insufficient to explain the observation from interferometers where much larger polarization fraction is observed when we zoom into the 'polarization hole'. We also imitate syn-

thetic beams of single dish polarization observation with interferometers data and find such volume smearing can significantly bring down the polarization fraction observed with interferometers. Motivated by the above results, we propose that the line of sight magnetic field structures may significantly lower the observed polarization and may be the prime reason for the observed phenomenon.

## 2.1 Introduction

Linear polarization has been used to study magnetic fields in molecular clouds. It is believed to be produced by aspherical dust grains, with their shorter axes (rotational axis) aligning along the ambient magnetic fields (for a detailed review go to this Lazarian (2007); Andersson et al. (2015)). As a result, thermal dust emissions, polarized preferentially along the longer axes of the dust grains, should reveal the plane of sky magnetic field direction with a 90 degree rotation. In many previous sub-mm polarization observations, the degree of polarization, which is the ratio of the polarized flux to total flux, from cloud cores are often found to decrease toward their flux peak (e.g. Girart et al. (2006); Li et al. (2009a); Liu et al. (2013)). Such phenomenon is often termed the "Polarization Hole" and vari-

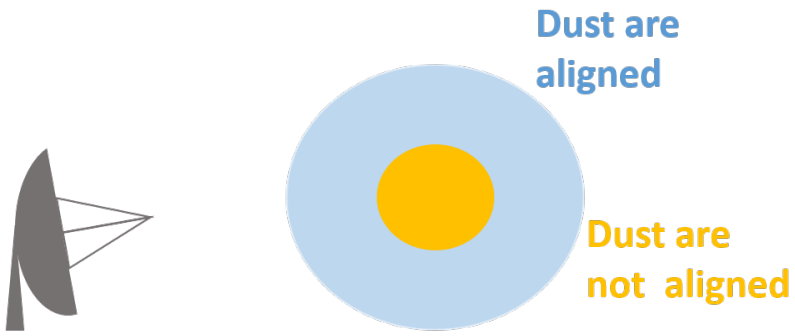


Figure 2.1: An illustration of the proposal by Padoan et al. (2001)

ous ideas have been proposed to explain this. Changes in dust properties or shapes (e.g. the growth of spherical grains) (Vrba et al. (1993)) might give rise to the observed depolarization. Another common interpretation is that the grain alignment efficiencies in cloud cores is low, owning to the high density and temperature (Hildebrand et al. (1999)). Padoan et al. (2001) for example attempted to simulate the observed depolarization pattern from self-gravitating cores from their super-Alfvenic MHD simulation. The steep decrease of polarization with increasing density/dust emission can only be recovered by assuming grains are no longer aligned at $Av > 3mag$. They concluded that the sub-mm polarization do not map the magnetic field in cores with $Av > 3mag$.

Some others (e.g. Matthews et al. (2005), Li et al. (2009b)) proposed that polarization holes arise from the low resolution

power of the telescope. Any fluctuations of magnetic fields within a telescope beam would only add up and contribute to a lower degree of polarization. In this chapter, we put the latter idea to a test with polarization data obtained from single dish telescopes and interferometers . With the spatial filtering effect and the high resolution interferometers offered, polarized emission from deeply embedded dense cores can be revealed and shed light on the degree of alignment of dust in these regions. In the first section, we compare the polarization fraction from interferometers with those from single dish telescopes from the same pointing of the sky. If the low polarization fraction, or 'polarization hole' effect seen from single dish telescopes were to be caused by the misalignment of dust grains in high density region, interferometers, zooming in into the cores unresolvable by single dish, should see an even lower polarization fraction. On the other hand, without assuming the change of alignment efficiency with density, unresolved B-field structures can also give rise to the low observed polarization fraction. In the second section, we try to smooth the interferometer data to the resolution of single dishes. This thus allows us to understand to what extent tangled B-field unresolvable by the beam can bring down the degree of polarization. The B-field morphologies of these

clumps/cores are shown in Figure 1.2 - 1.15.

## 2.2 Sub-mm polarization data

SCUPOL 850$\mu m$ legacy survey (Matthews et al. (2009)) with James Clerk Maxwell Telescope (JCMT) and TADPOL 1.3$mm$ survey (Hull et al. (2014)) with The Combined Array for Research in Millimeter-wave Astronomy (CARMA) offered respectively polarization data from single dish telescope and interferometer. On one hand JCMT with an approximate $\sim 20''$ resolution offered a bigger picture of the field morphology of the clump, CARMA zoomed deeper into the cloud cores with $\sim 2.5''$ resolution. We compare the polarization measurements of the overlapping sets of objects from these two archives. The list of objects are tabulated in Table 2.1.

| Object | Location of the new synthesized beam | |
|---|---|---|
| W3Main | $2^h25^m40^s$ | 62°5'47" |
| | $2^h25^m39^s$ | 62°5'53" |
| | $2^h25^m37^s$ | 62°5'58" |
| | $2^h25^m38^s$ | 62°5'47" |

| | | |
|---|---|---|
| W3OH | $2^h27^m4^s$ | 61°52'24" |
| | $2^h27^m3^s$ | 61°52'19" |
| L1448N | $3^h25^m36^s$ | 30°45'12" |
| SVS13 | $3^h29^m3^s$ | 31°16'1" |
| | $3^h29^m3^s$ | 31°15'51" |
| IRAS4A | $3^h29^m10^s$ | 31°13'31" |
| | $3^h29^m11^s$ | 31°13'8" |
| HH211 | $3^h43^m56^s$ | 32°0'48" |
| | $3^h43^m55^s$ | 32°0'52" |
| L1527 | $4^h39^m53^s$ | 26°3'10" |
| OrionKL | $5^h35^m15^s$ | -5°22'5" |
| | $5^h35^m14^s$ | -5°22'16" |
| | $5^h35^m14^s$ | -5°22'32" |
| | $5^h35^m14^s$ | -5°22'42" |
| VLA1623 | $16^h26^m26^s$ | -24°24'30" |
| | $16^h26^m26^s$ | -24°24'28" |
| SerEmb8 | $18^h29^m47^s$ | 1°16'45" |
| | $18^h29^m48^s$ | 1°16'57" |

| | | |
|---|---|---|
| CB230 | $21^h17^m38^s$ | 68°17'29" |
| | $21^h17^m38^s$ | 68°17'39" |
| NGC7538 | $23^h13^m45^s$ | 61°28'15" |
| | $23^h13^m43^s$ | 61°28'11" |
| | $23^h13^m44^s$ | 61°28'12" |
| | $23^h13^m45^s$ | 61°28'10" |

Table 2.1: The list of objects from CARMA and JCMT.

Since these polarization measurements are made in different wavelengths, 'calibration' must be applied to these sets of data to ensure a fair comparison of the polarization fraction. In a previous study by Vaillancourt & Matthews (2012), they compared polarizations observations of 17 molecular clouds with data archives of Hertz and SCUBA, and found that the median ratio of polarization fraction between $850\mu m$ and $350\mu m$ is $1.7 \pm 0.6$. Similarly for $1300\mu m$, Vaillancourt (2002) arrived at a ratio of $2.1 \pm 0.65$ when compared to $350\mu m$ measurements,

however with only one cloud DR 21 (Main). In analyses below, we would 'calibrate' the TADPOL 1300$\mu m$ data to 850$\mu m$ polarization, as if observed with SCUPOL with these 'correction factors' from Vaillancourt & Matthews (2012) and Vaillancourt (2002).

## 2.3 Observation I: Grains are aligned in regions of high density/extinction

Arrangement of antenna configurations in an interferometer will only have baselines with certain lengths, therefore, only structures of certain angular sizes can be detected. The shortest baseline usually defines the largest structures observable with that particular array configuration. Any structures with angular size larger than that would not be detected. This is often termed the spatial filtering effect of an interferometer and effectively allows observers to zoom deeper into the densest region with the relatively diffused region filtered. On the other hand, single dish telescope is free from the spatial filtering suffered by interferometer, capable of including the contributions from both the foreground and background.

If 'polarization hole' observed with single dish telescope is to

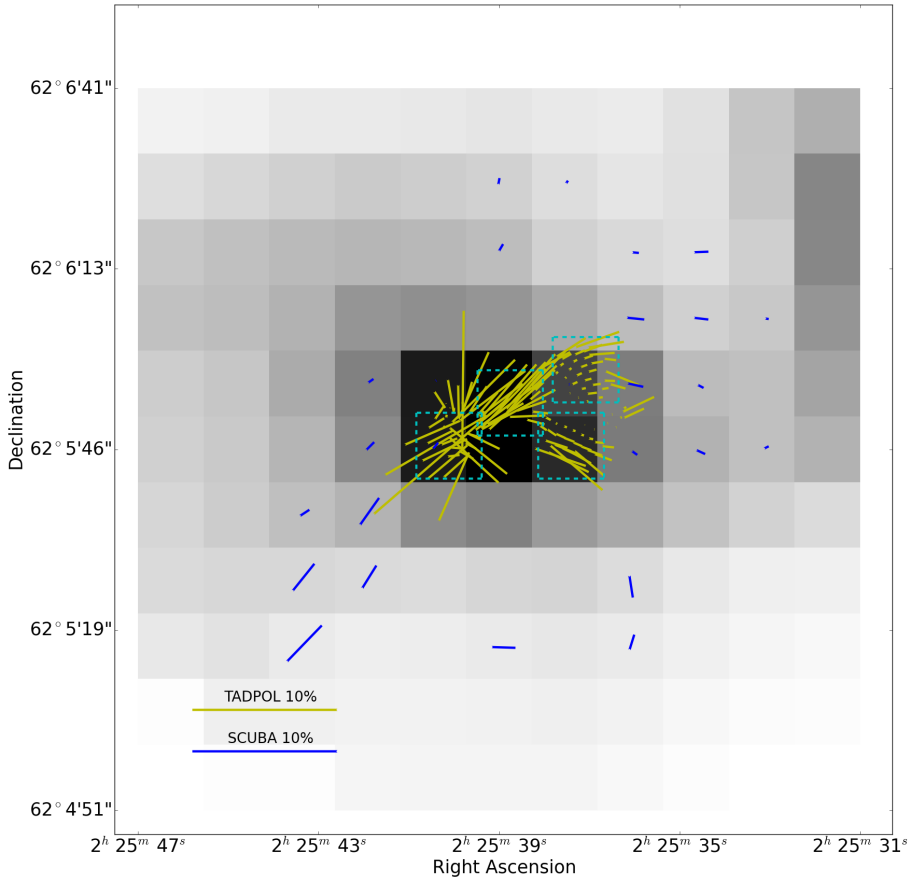


Figure 2.2: Maps of W3 Main. The grayscale image is proportional to the total intensity of the dust emission measured by SCUPOL. The blue and yellow segments showed the inferred B-field direction from SCUPOL and TADPOL respectively. The lengths of theses segments are proportional to the degree of polarization. The cyan dashed boxes show the location of the synthetic beams.

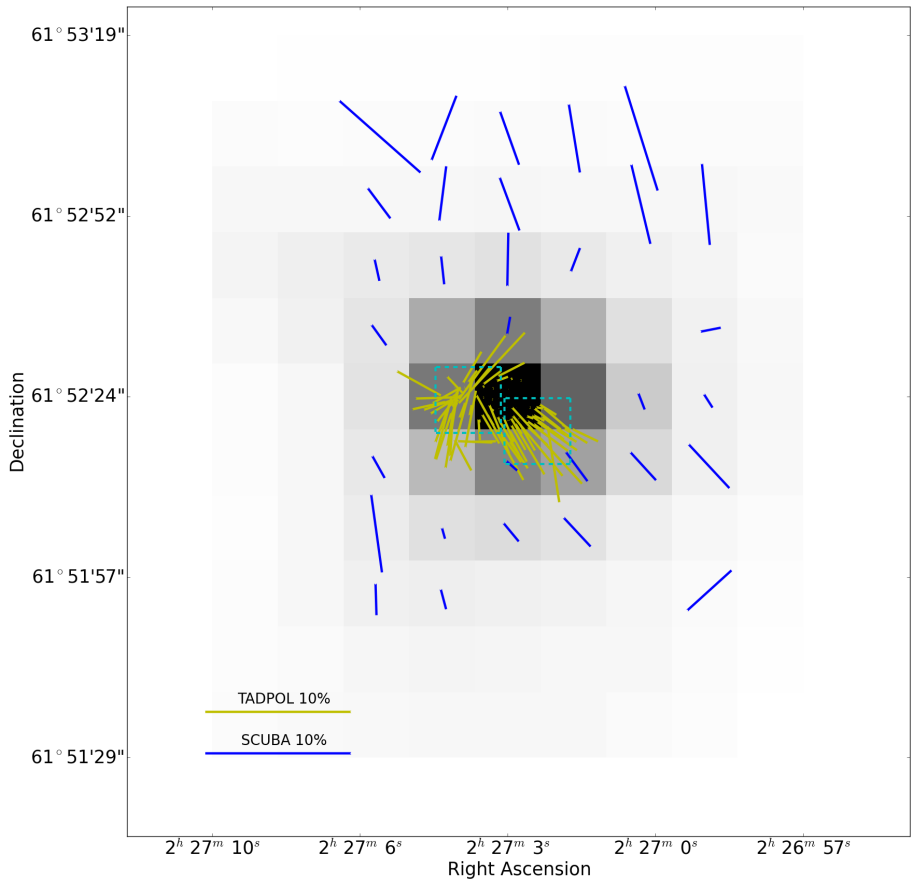


Figure 2.3: W3(OH). Same as Figure 2.2.

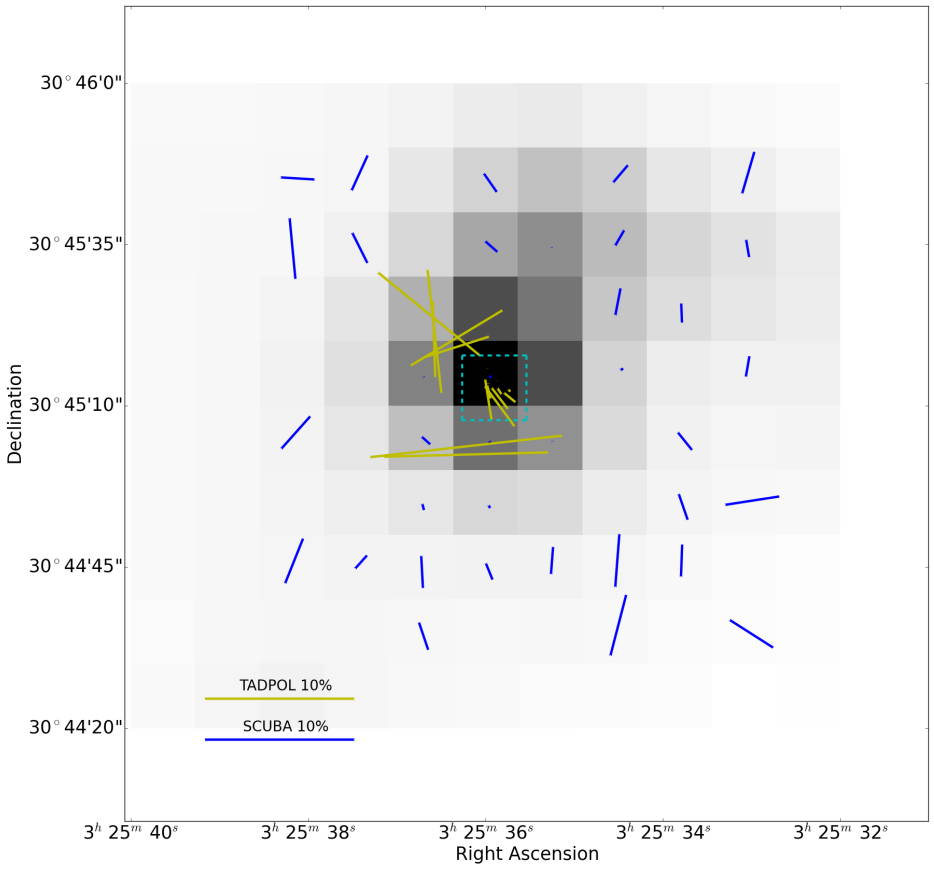


Figure 2.4: 1448N. Same as Figure 2.2.

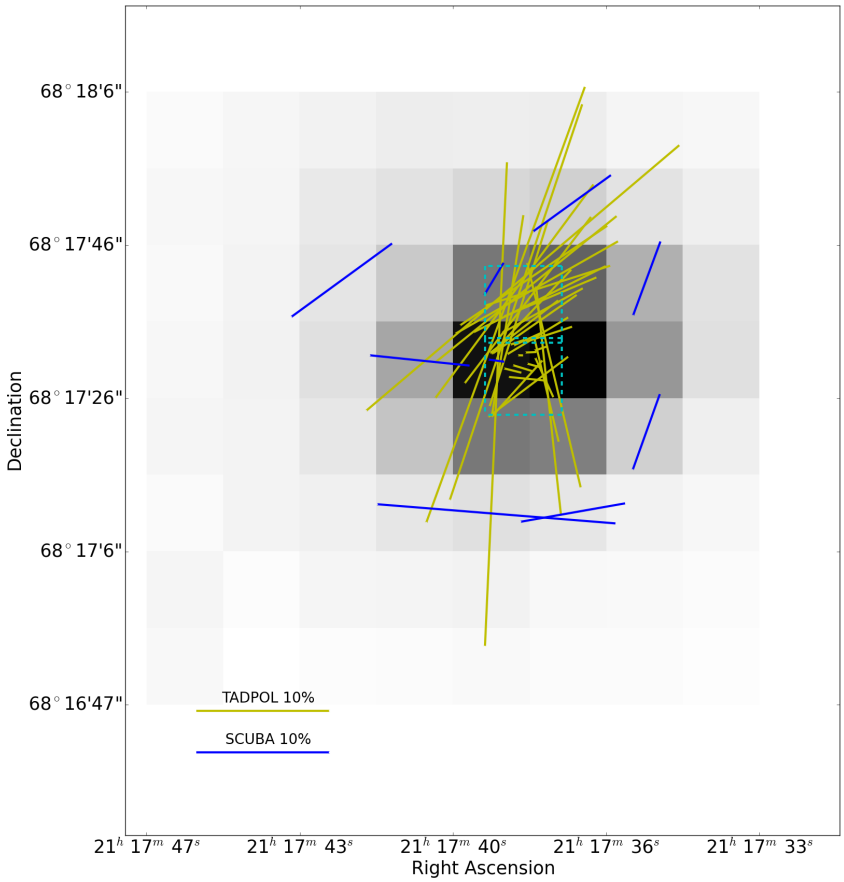


Figure 2.5: CB230. Same as Figure 2.2.

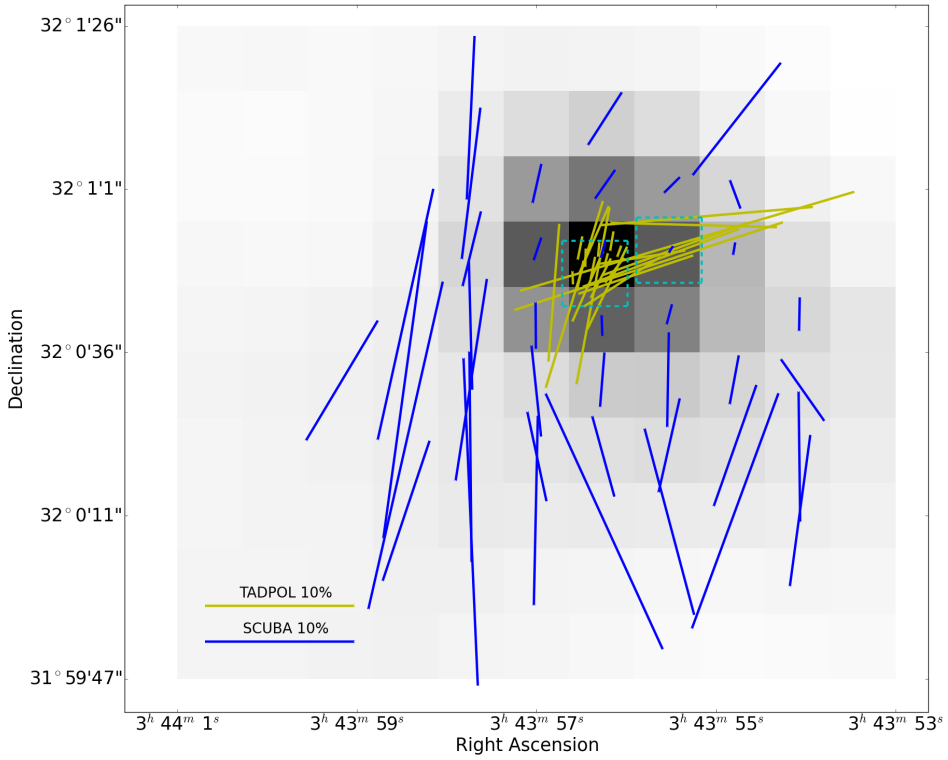


Figure 2.6: HH211. Same as Figure 2.2.

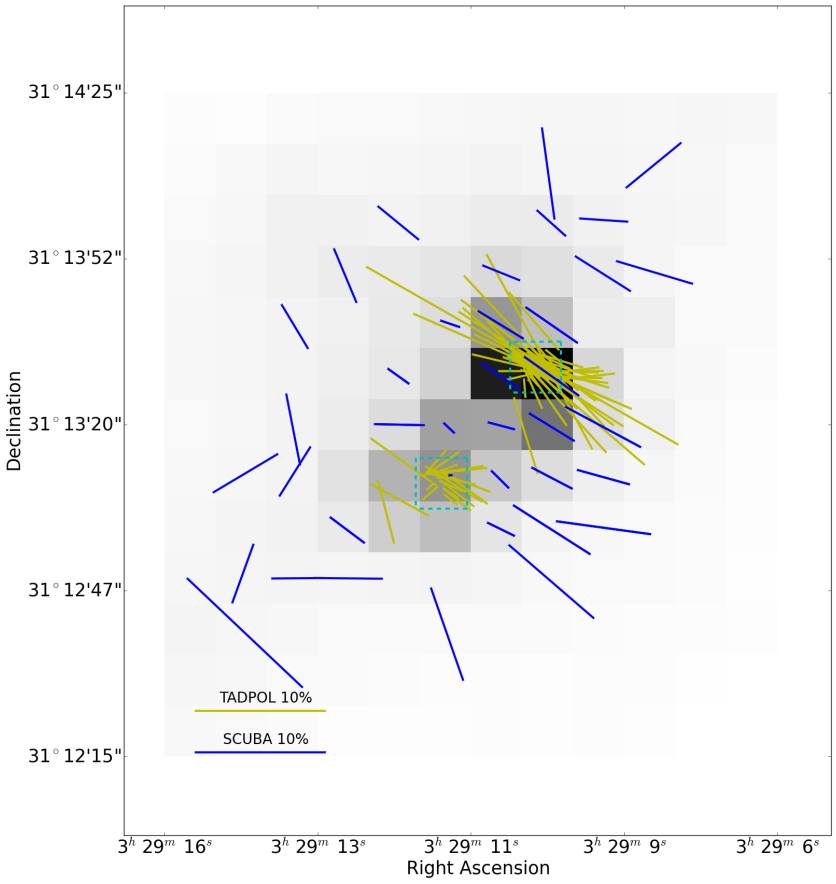


Figure 2.7: IRAS4A. Same as Figure 2.2.

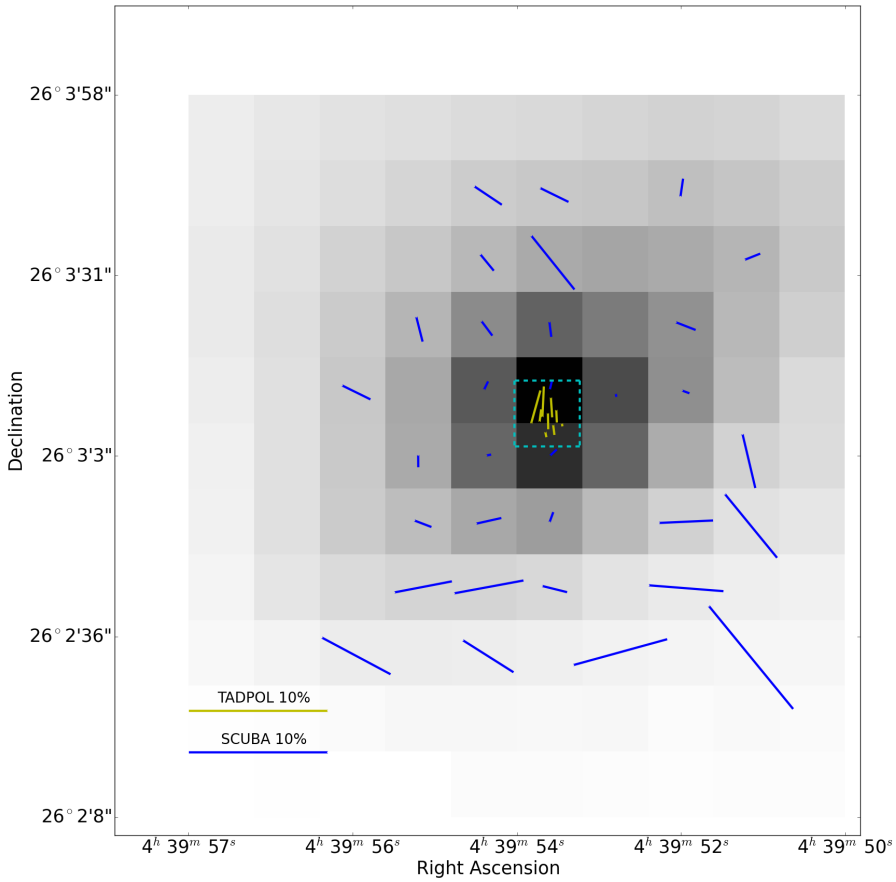


Figure 2.8: L1527. Same as Figure 2.2.

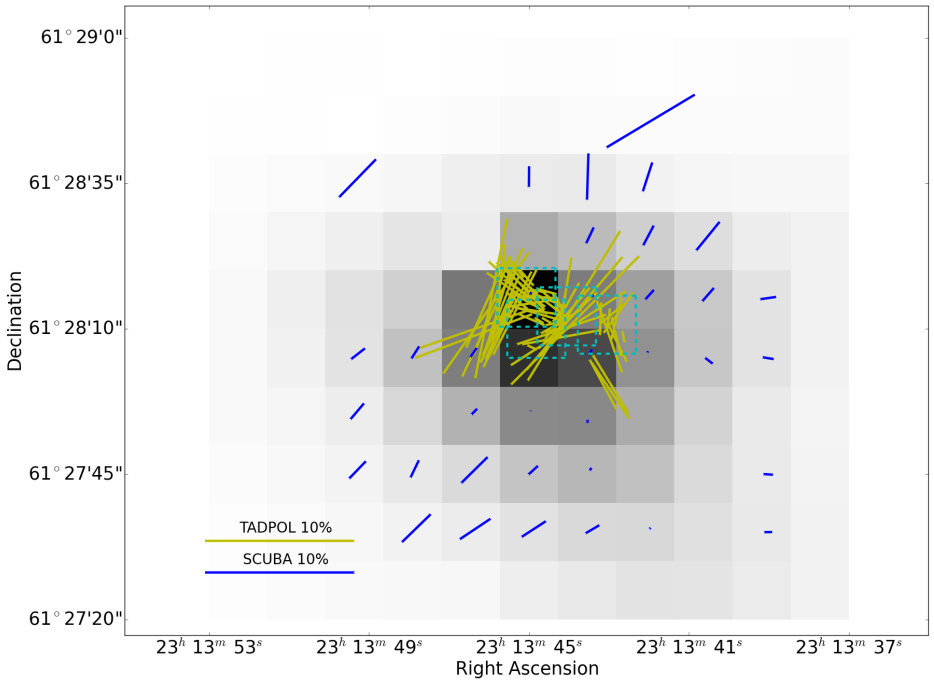


Figure 2.9: NGC7538. Same as Figure 2.2.

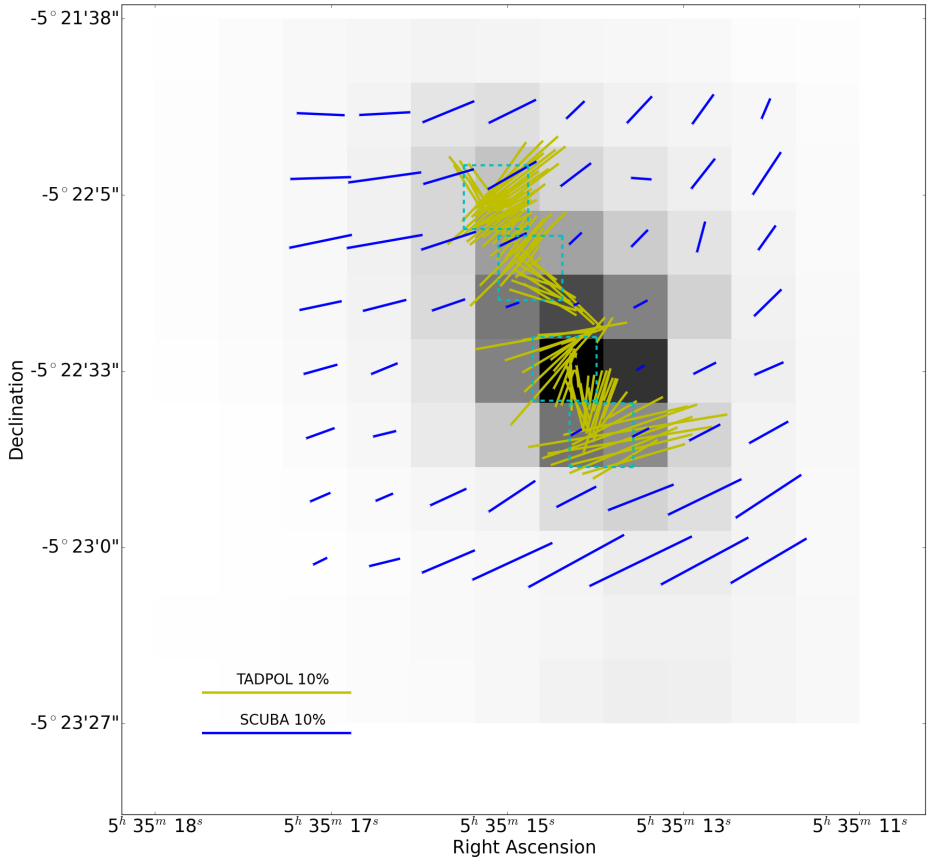


Figure 2.10: Orion KL. Same as Figure 2.2.

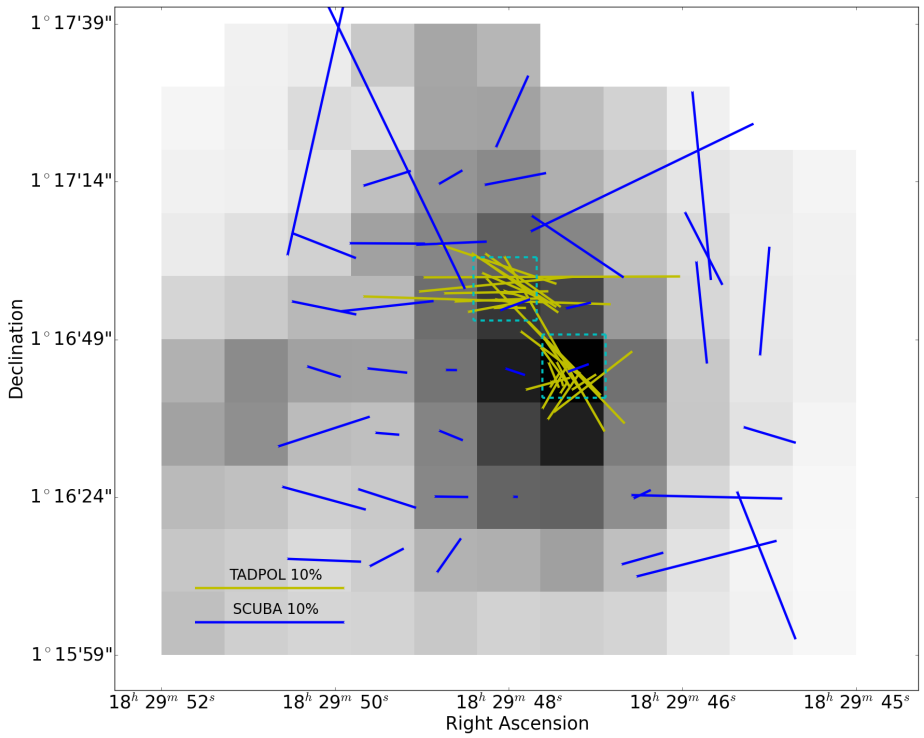


Figure 2.11: Ser-Emb8. Same as Figure 2.2.

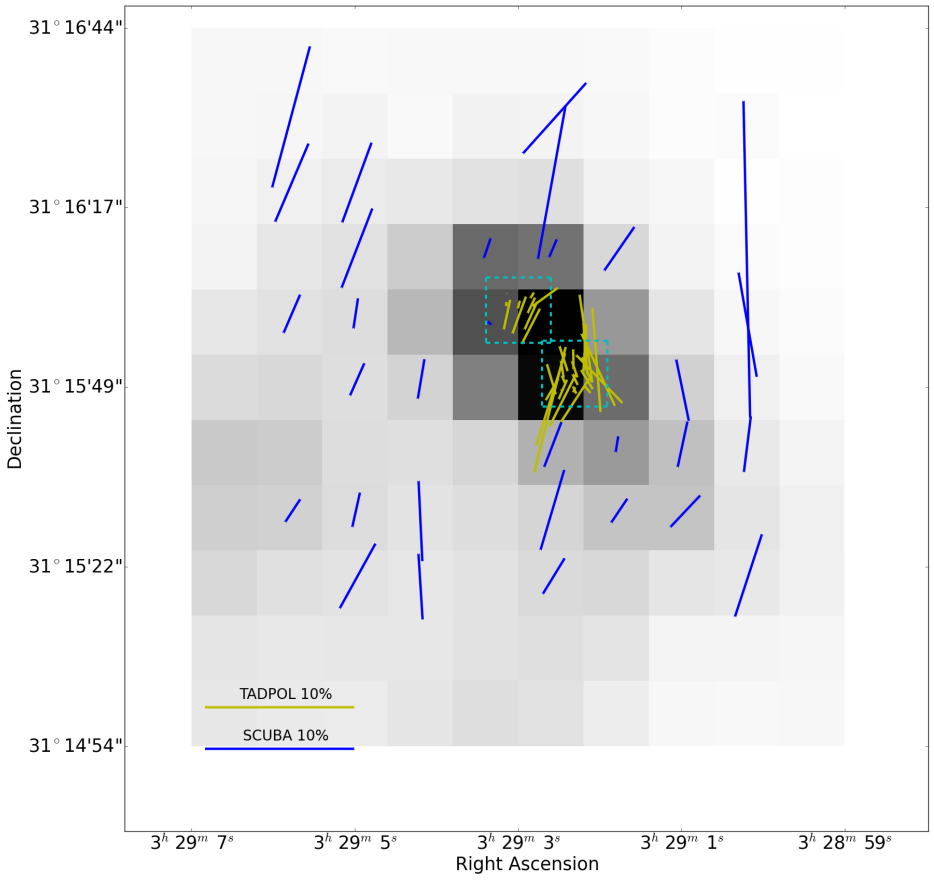


Figure 2.12: SVS13. Same as Figure 2.2.

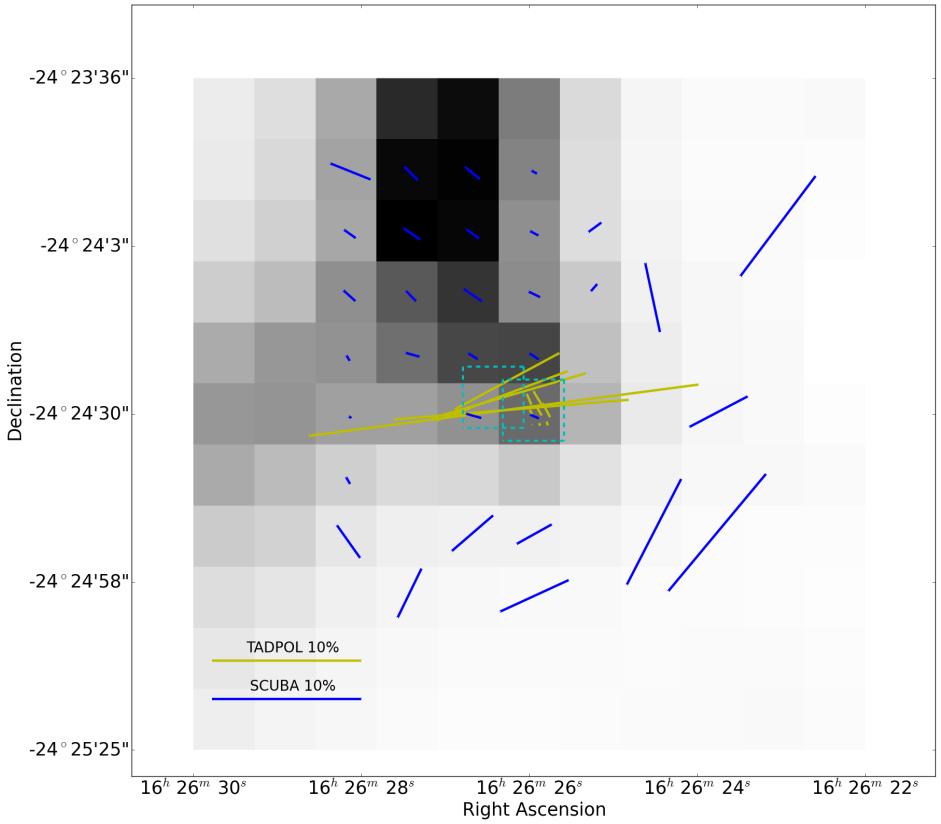


Figure 2.13: VLA1623. Same as Figure 2.2.

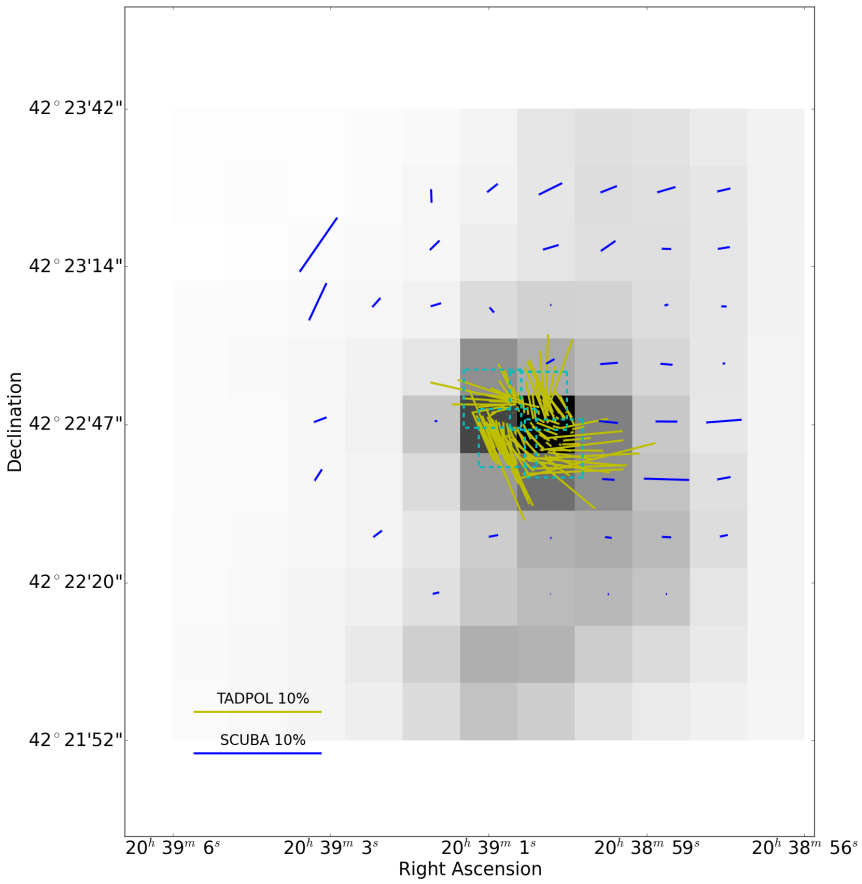


Figure 2.14: DR21(OH). Same as Figure 2.2.

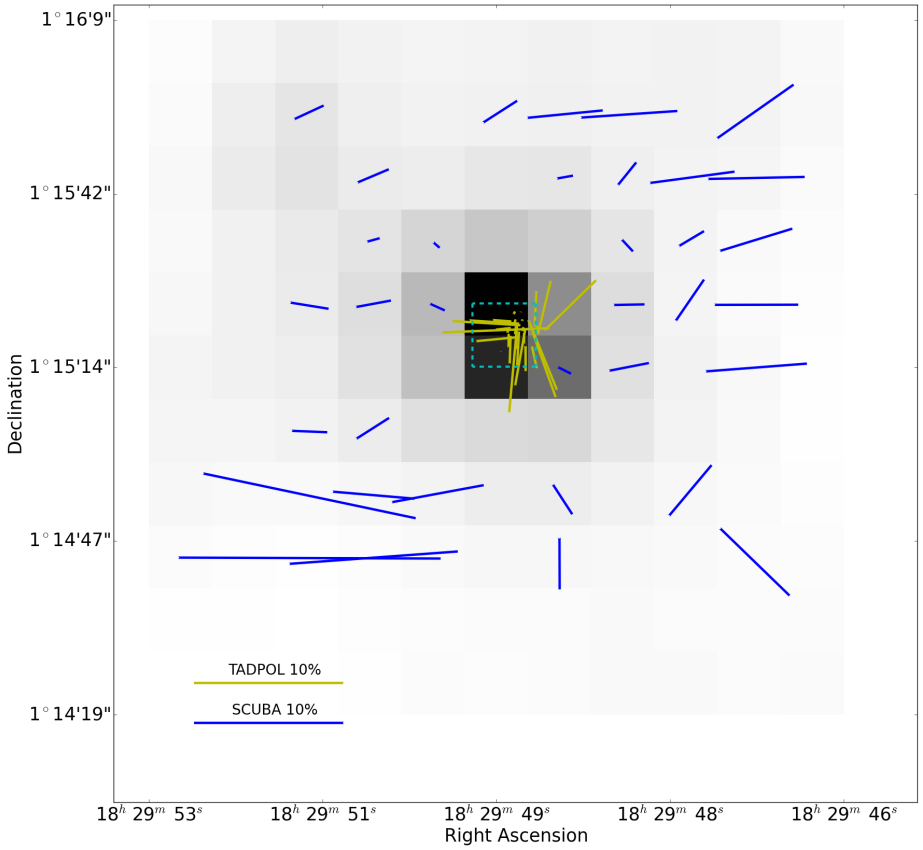


Figure 2.15: Ser-Emb6. Same as Figure 2.2.

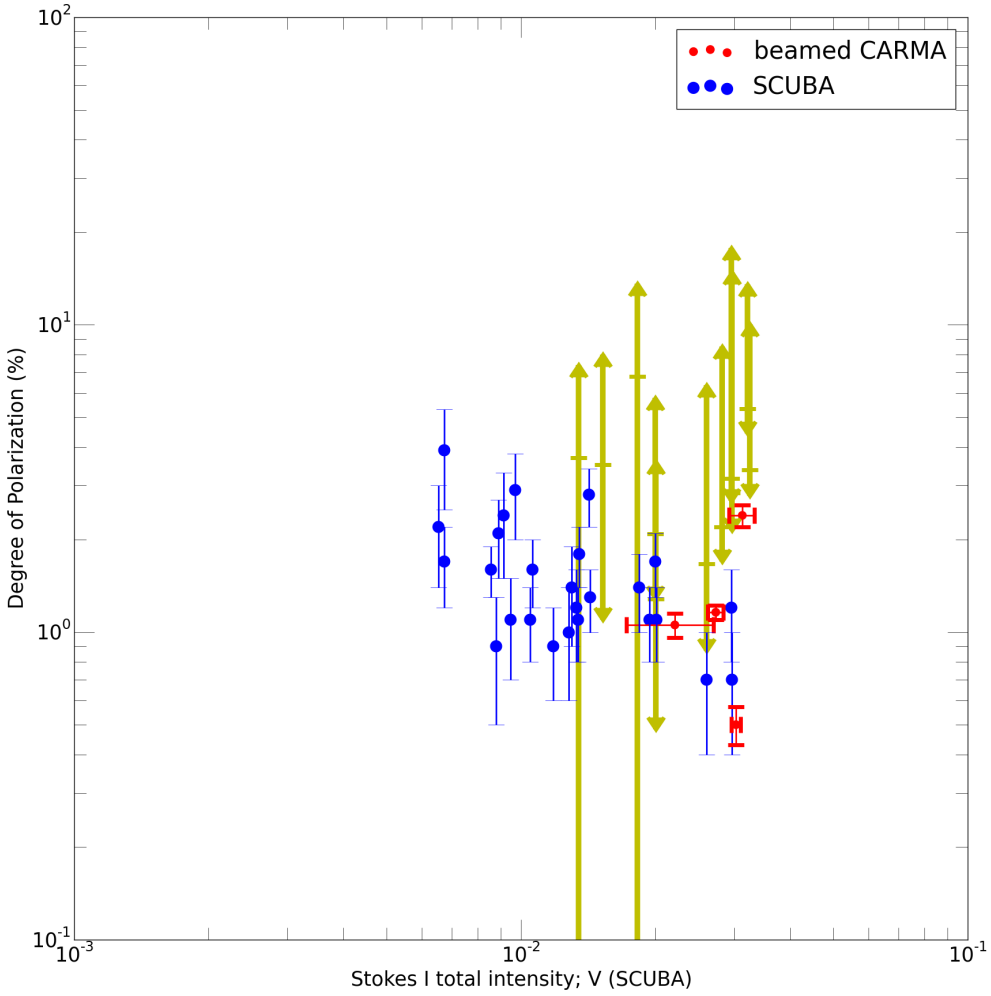


Figure 2.16: The distribution of polarization percentage with intensity for W3 Main. Data from SCUPOL and TADPOL are plotted in blue and yellow respectively. The yellow arrows demonstrate the range of polarization percentage spanned by TADPOL detections for the corresponding SCUPOL pointing they lie in. CARMA data are smoothed to the resolution of SCUPOL and are shown as the red scatter dots.

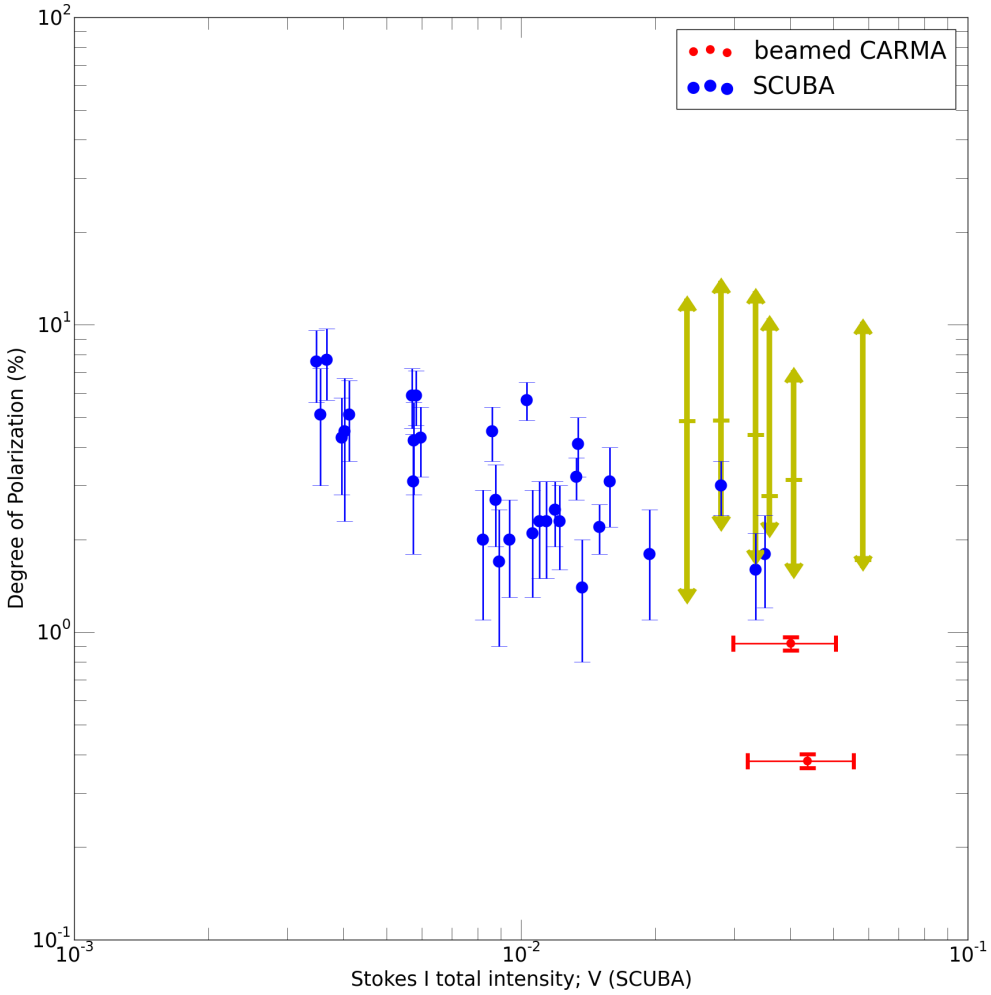


Figure 2.17: W3 (OH). Same as Figure 2.16.

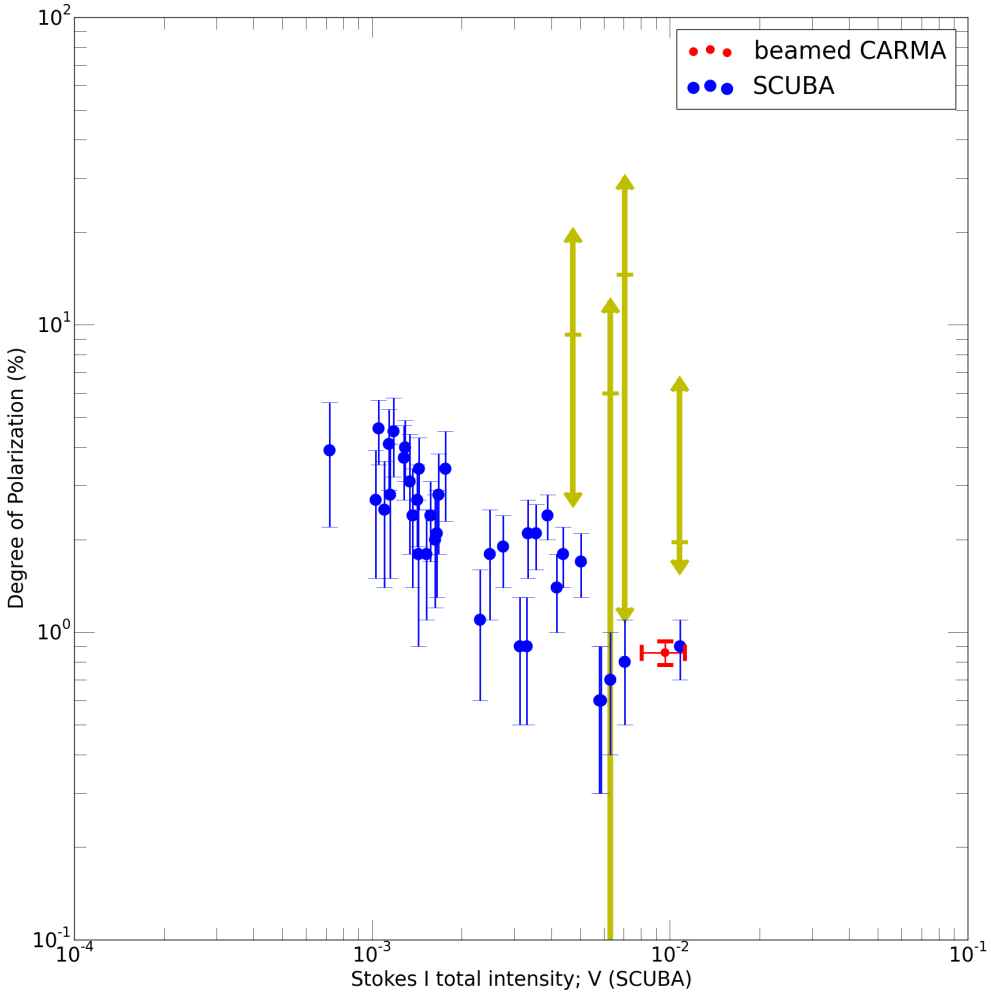


Figure 2.18: L1448N. Same as Figure 2.16.

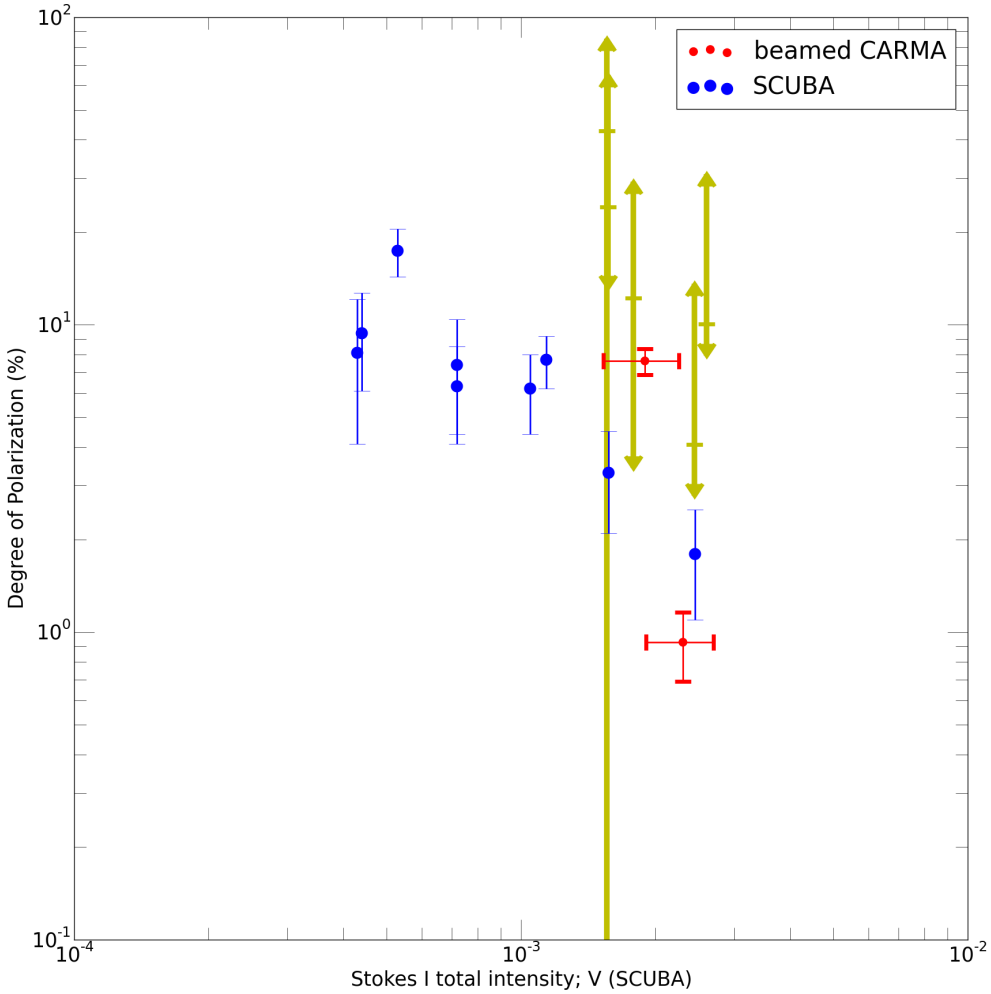


Figure 2.19: CB230. Same as Figure 2.16.

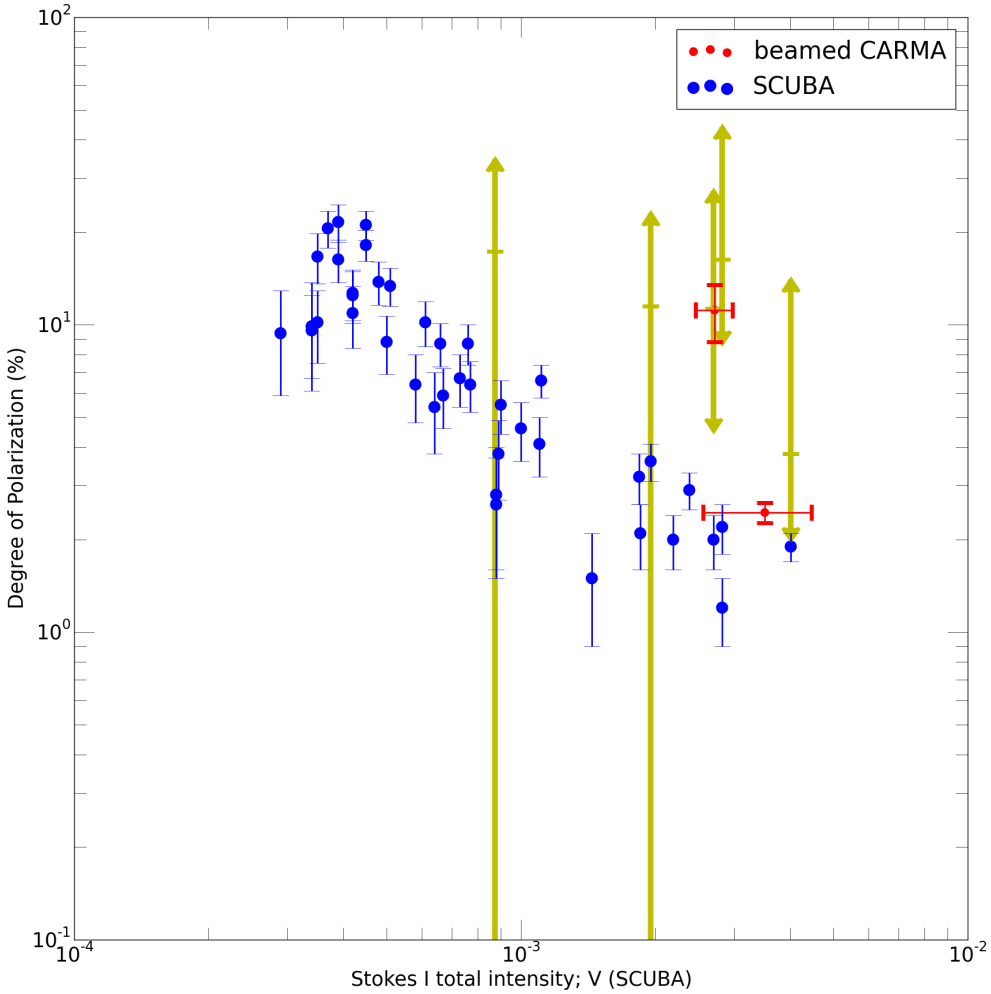


Figure 2.20: HH211. Same as Figure 2.16.

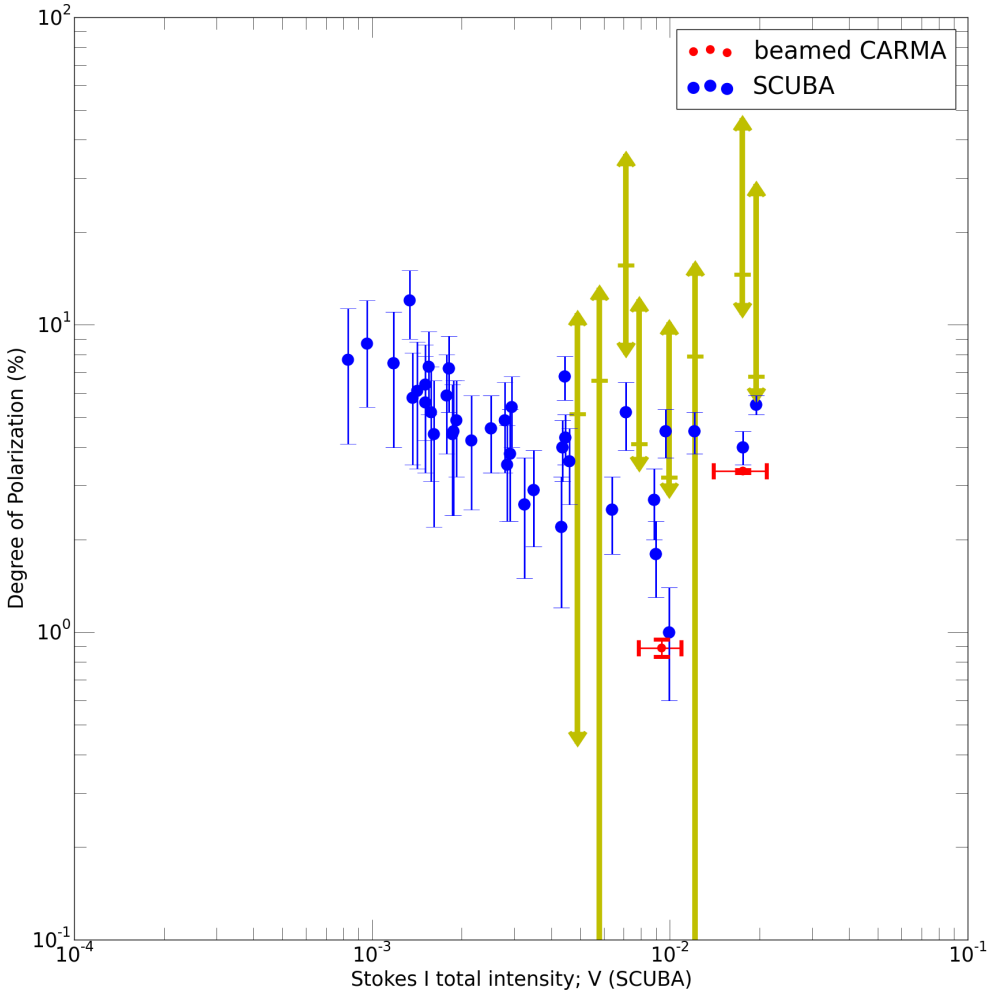


Figure 2.21: IRAS4A. Same as Figure 2.16.

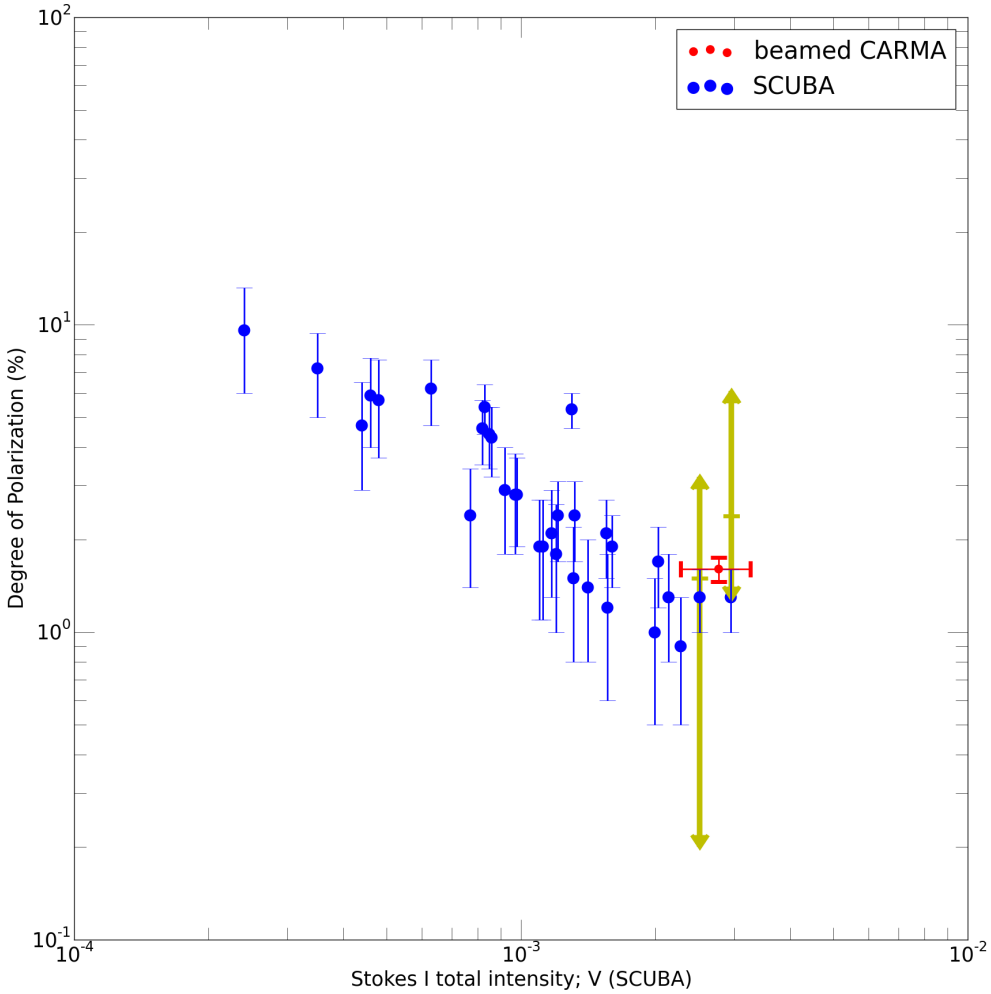


Figure 2.22: L1527. Same as Figure 2.16.

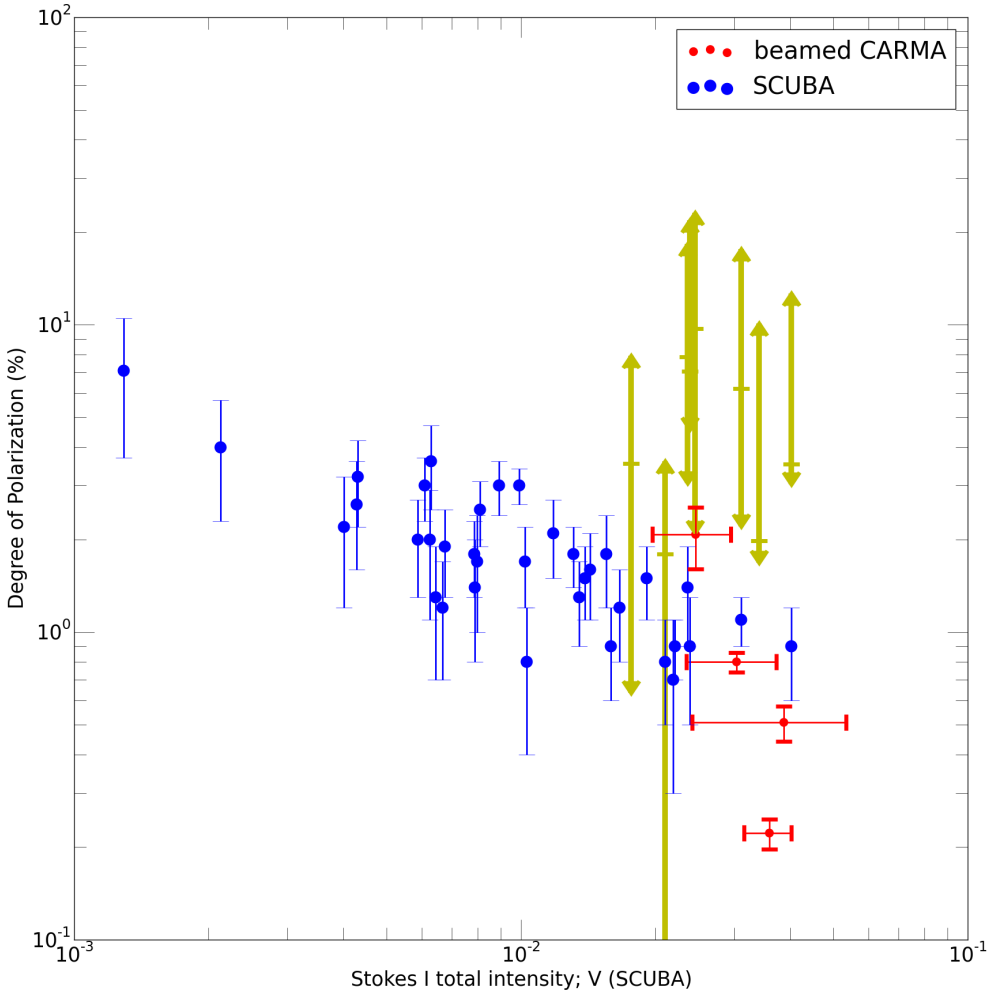


Figure 2.23: NGC7538. Same as Figure 2.16.

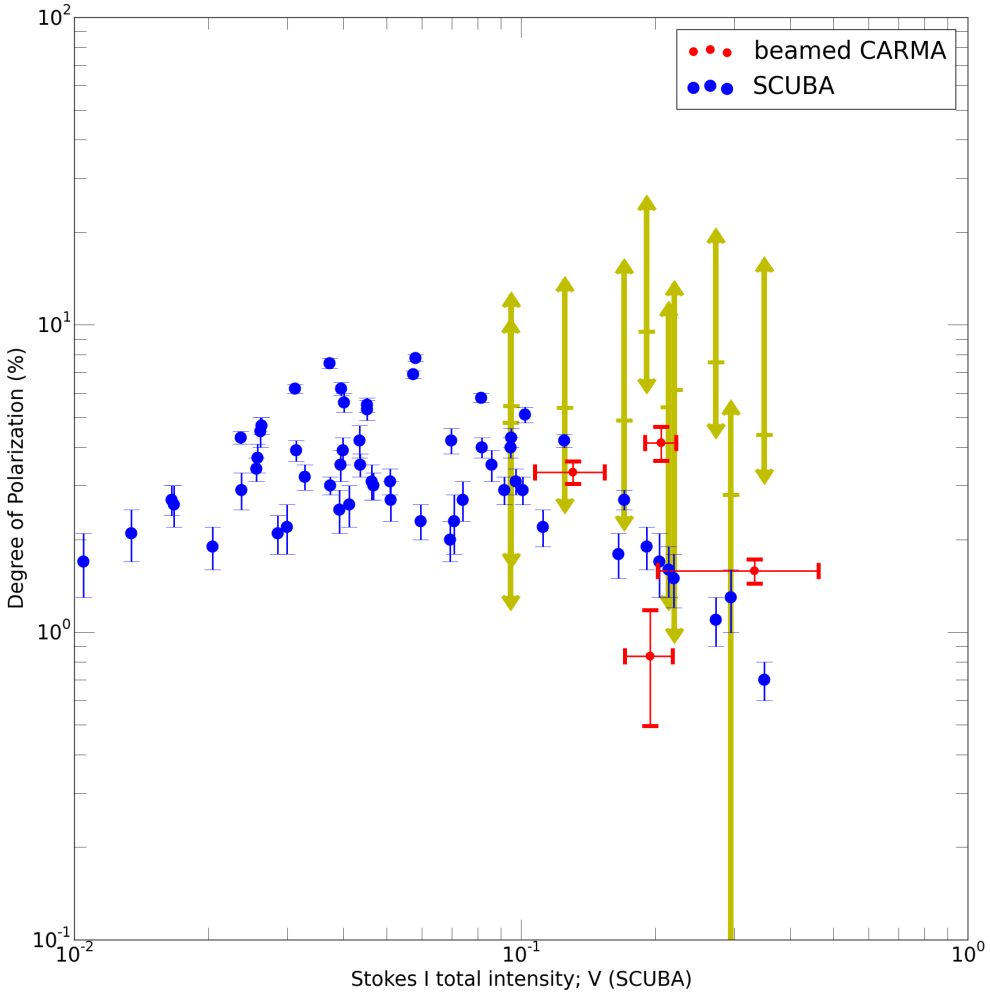


Figure 2.24: Orion KL. Same as Figure 2.16.

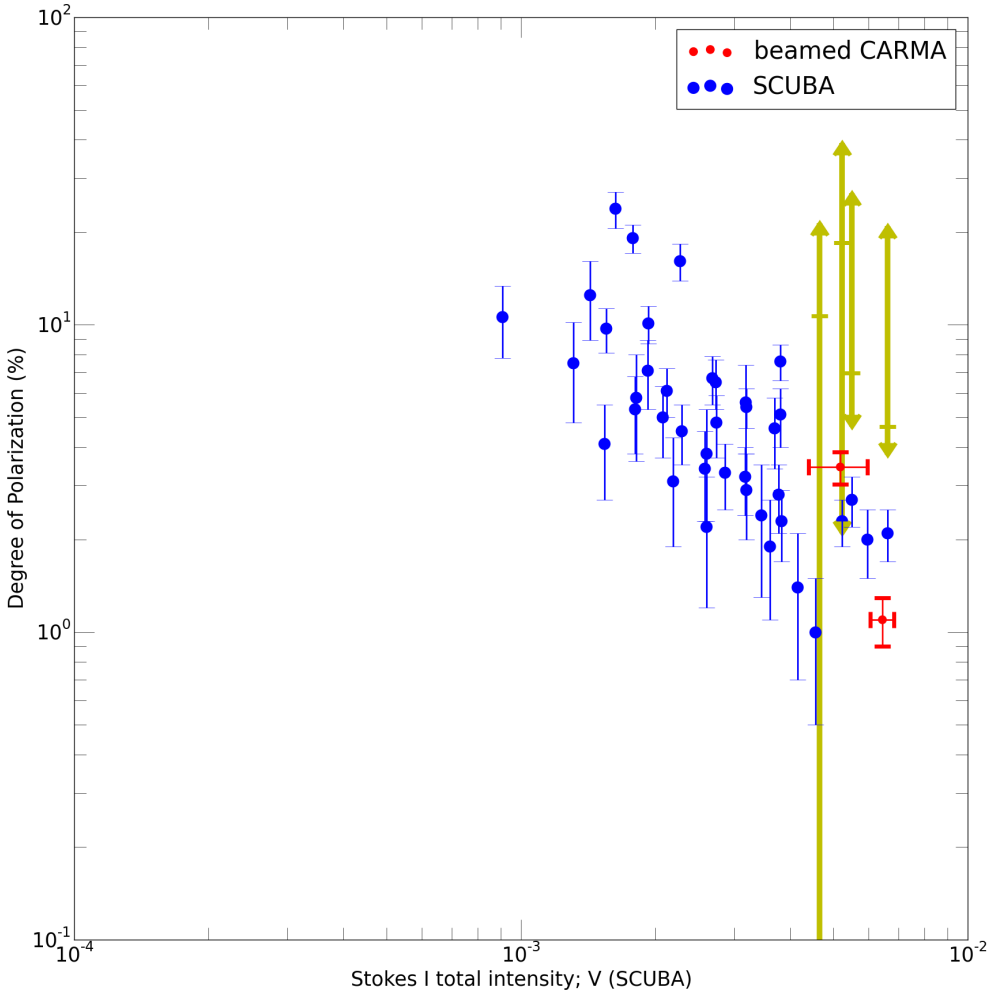


Figure 2.25: Ser-Emb8. Same as Figure 2.16.

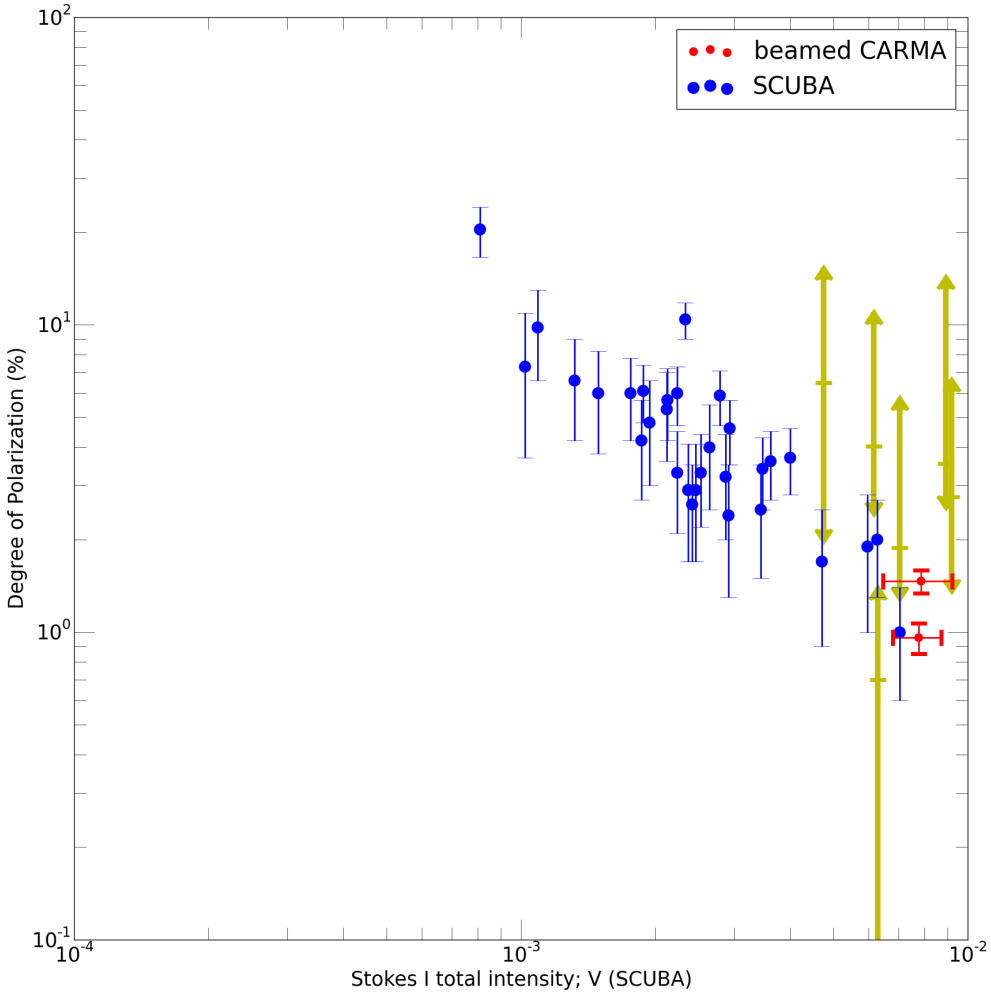


Figure 2.26: SVS13. Same as Figure 2.16.

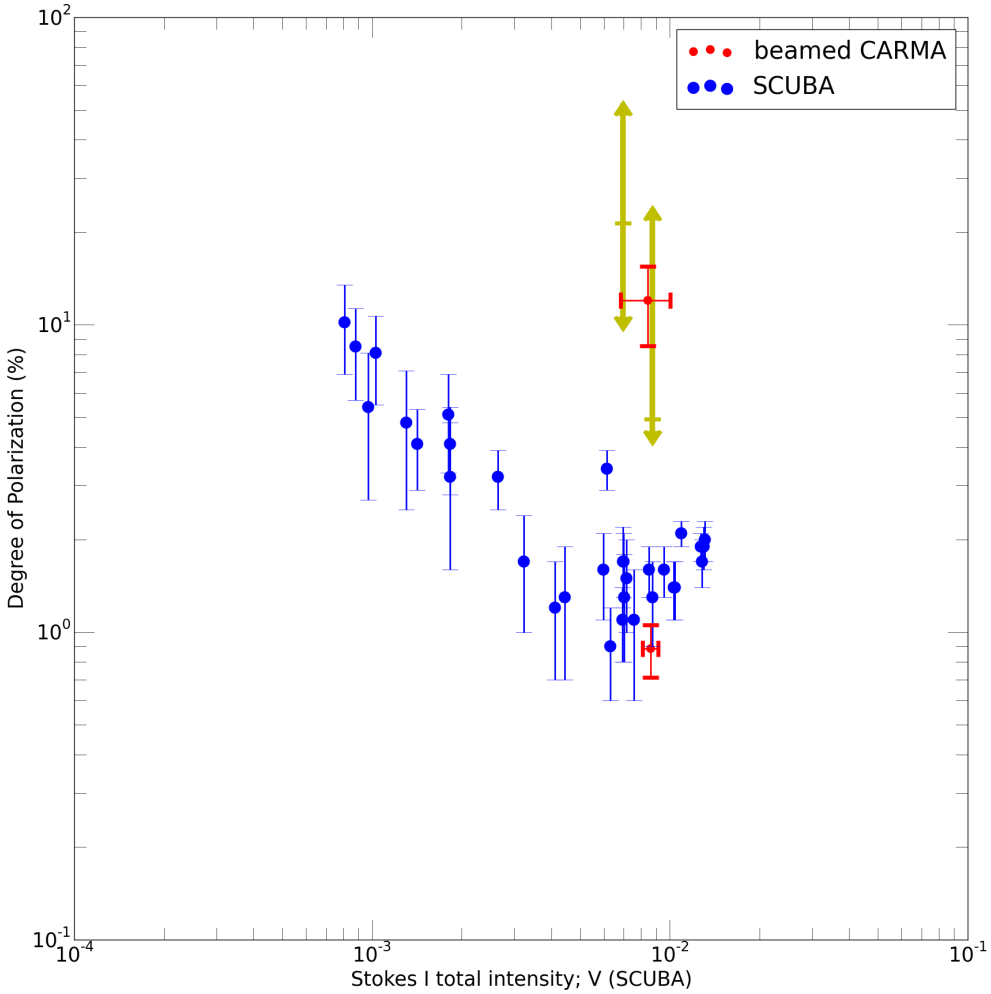


Figure 2.27: VLA1623. Same as Figure 2.16.

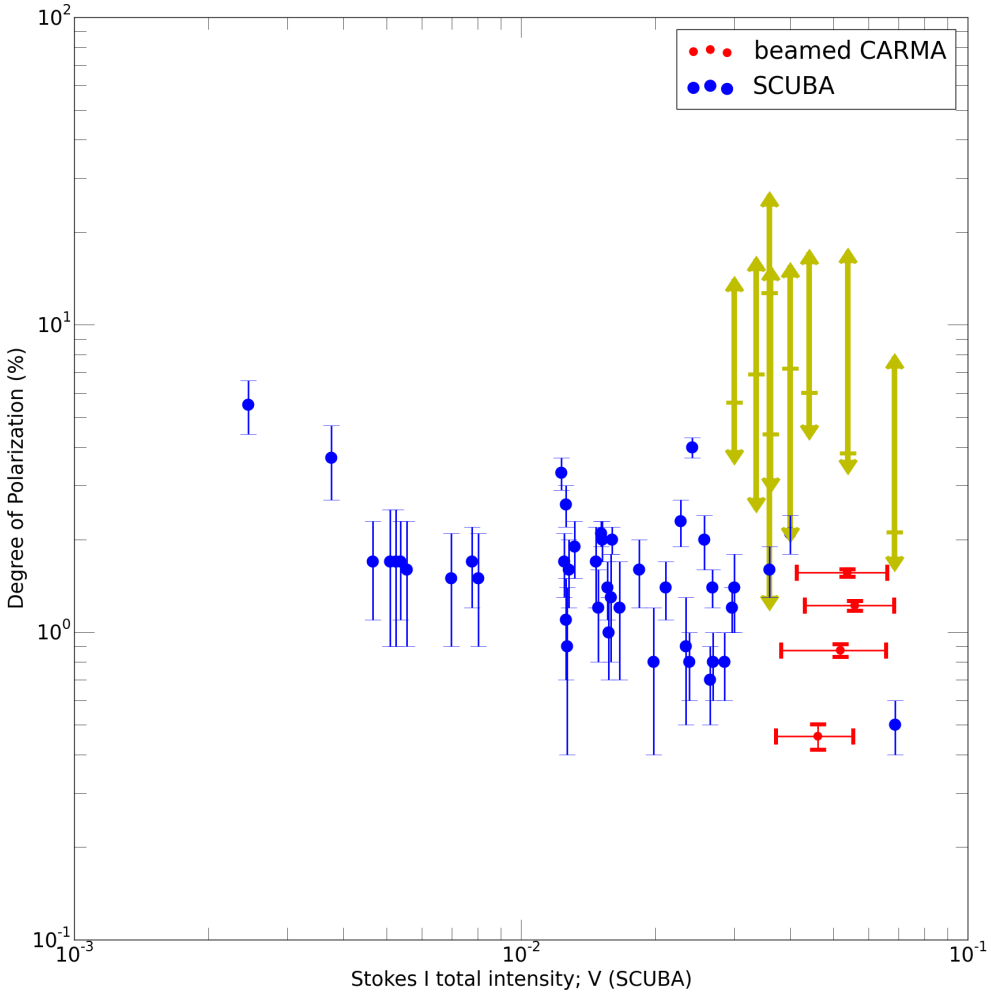


Figure 2.28: DR21(OH). Same as Figure 2.16.

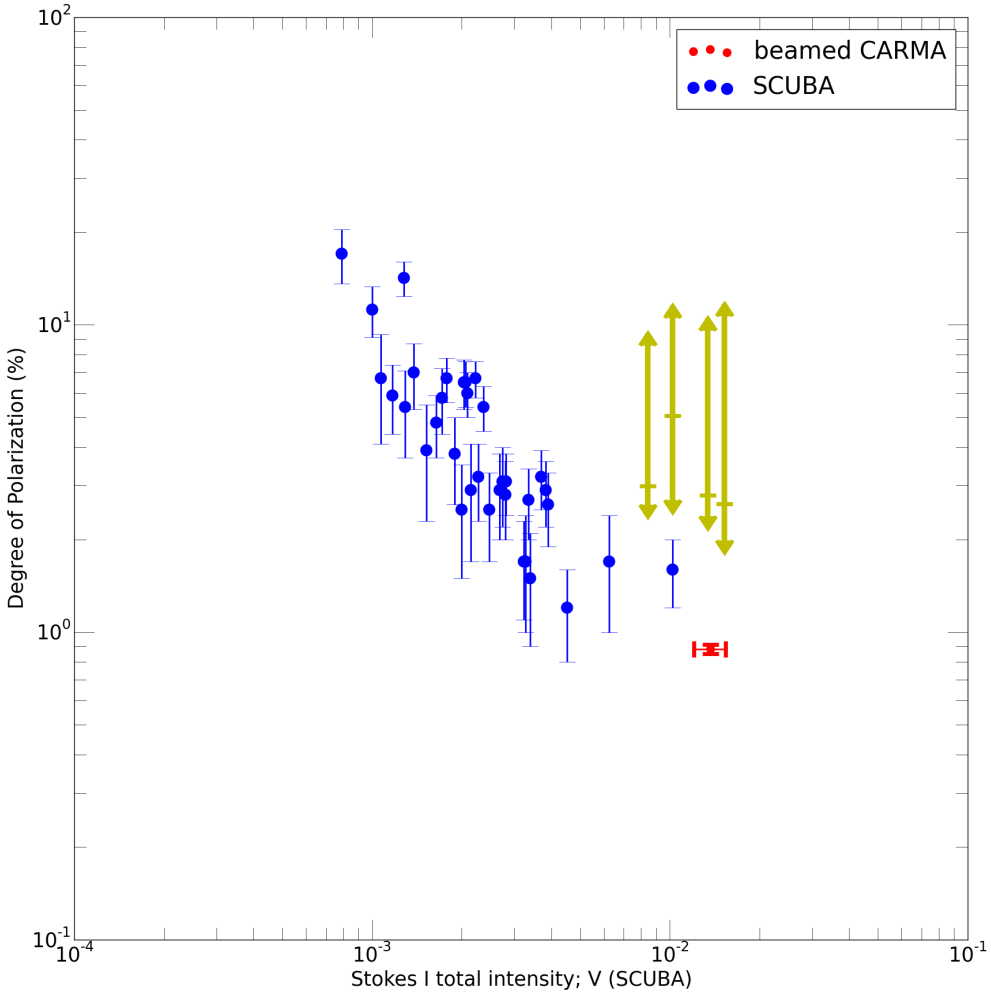


Figure 2.29: Ser-Emb6. Same as Figure 2.16.

be explained with the decrease in grains alignment efficiencies with increasing density, polarized emission from low density region should contribute most to the observed polarization (stokes Q and U) and high density region contributes mostly to intensity (stokes I) instead of the polarized intensity Padoan et al. (2001). This although explains why the polarization ratio observed from the region with highest density/extinction is low, it would be demonstrated in this section that it fails to interpret the high polarization fraction detected from interferometer.

Polarization detections from TADPOL are first allocated to different bins according to which SCUPOL telescope pointing they lie in, and are assigned with the corresponding SCUBA measured response voltage. In Figure 1.16 - 1.29, the degree of polarization is plotted against the intensity measured by 'SCUPOL' in log-log scale for these two sets of observation. Polarization measured SCUPOL and TADPOL are shown in yellow and blue respectively. Yellow arrows and filled circles demonstrate respectively the range of degree of polarization spanned, and the average degree of polarization from TADPOL within these SCUPOL pointing. Blue error bars are the measurement error from SCUBA. Zooming into high density regions with interferometer (higher intensity end) where low polarizations are detected by

single dish telescope, much higher polarization fractions (yellow arrows) are detected instead in the same telescope pointing. Object such as W3 (OH), SVS13, Ser-emb6 where single dish did not see any polarization from the core peak, there are still detections with interferometers. If grain alignment is turned off in high density regions, interferometer, which filters out the lower density part, should see even smaller degree of polarization. Yet, the contrary is observed.

## 2.4 Observation II: Smearing effect within the beam

TADPOL data ($\sim 2.5''$) has approximately 8 times better resolution than SCUPOL data ($\sim 20''$). Any unresolved magnetic field structures seen in interferometer at scales smaller than the resolution of the single dish telescope would bring down the observed polarization fraction. Here we try to synthesize a single dish observation with polarization data from TADPOL and check whether such fluctuations of polarization/B-field structures within a telescope beam constitute the prime reason to bringing down the polarization fraction. The pontings of these new mimicked beam are listed in Table 2.1. The cyan

dahsed boxes in Figures 1.2 -1.15 show the corresponding regions for smoothing the TADPOL data to 20″ resolution.

For each individual cloud core, $P, I, \theta$ from TADPOL are first converted to Stokes space $I$, $Q$ and $U$. Polarization detections from TADPOL that lie within the new telescope pointing (cyan dashed boxes) are then summed to mimick observations from single dish.

$$\begin{aligned} Q_i =& I_i P_i \cos 2\theta_i \\ U_i =& I_i P_i \sin 2\theta_i \\ U_{tot} = \Sigma U_i; \quad Q_{tot} =& \Sigma Q_i; \quad I_{tot} = \Sigma I_i; \\ < P > =& \frac{\sqrt{Q_{tot}^2 + U_{tot}^2}}{I_{tot}} \end{aligned} \tag{2.1}$$

The propagation of error during this coarse graining process can be estimated with Equation from section 2.1 of Stephens et al. (2011):

$$\sigma^2_{<P>} = \frac{Q^2_{tot}\sigma^2_{Q_{tot}} + U^2_{tot}\sigma^2_{U_{tot}}}{I_{tot^2}(U^2_{tot} + Q^2_{tot})} + \frac{(U^2_{tot} + Q^2_{tot})\sigma^2_{I_{tot}}}{I^4_{tot}} \tag{2.2}$$

The results are overlaid on Figure 1.16 - 1.29 and are shown as the red dots. The degree of polarization from TADPOL survey are significantly lowered when they are smoothed to the resolution of the SCUPOL survey. The trend of sharp decrease in polarization fraction with increasing intensity traced by SCU-

POL is nicely recovered for most of these new synthesized beam pointings. It demonstrates that the low polarization fraction observed with SCUPOL originates from the unresolvable polarization structures seen in single dish telescope resolution.

## 2.5 Discussions

The proposal by Padoan et al. (2001) is incapable of explaing the high polarization fraction observed in interferometers. We have also shown that the smearing of small scale polarization/B-field structures (unresolvable with the telescope beam, in our demonstration: single dish telescope) can give rise to the observed depolarization towards the core. Since sub-mm/mm thermal dust emission is usually optically thin, we can understand the observed polarization as an integration of the thermal dust emission along the line of sight. On one hand, the increase in dispersion of B-field along the line of sight can also lower the degree of polarization. For typical clumps/clouds, larger column density, suggesting a longer line of sight dimension $\Sigma \propto l_{los}^{a}$, should host more turbulent energy/larger velocity dispersion. $\sigma_v \propto l_{los}^{\beta}$. The dispersion of B-field can be related with the velocity dispersion through Chandrasekhar & Fermi (1953) method: $\delta\phi = \sqrt{4\pi\rho}\frac{\sigma_v}{|B_\perp|}$. Therefore, higher column density should host

larger dispersion in B-field along the line of sight which will naturally give rise to the low observed polarization fraction from high density region. On the other hand, the gravity is also at work. The pinching of B-field toward the gravitating center should be expected. When the B-field lie closer to the line of sight, lower polarization should arise naturally without involving the change in grain alignment efficiency. Gonçalves et al. (2005); Kataoka et al. (2012) simulated the polarized emission from the cloud cores. Without involving the change in alignement efficiency and the effect of turbulence, they showed the depolarization can arise simply due to the geometrical effect.

---

□ **End of chapter.**

# Chapter 3

# Studying Turbulent Ambipolar Diffusion in NGC 6334

It has been observed that, in molecular clouds, ions consistently showed a narrower linewidth than the coexisting neutrals. This has been proposed to be a signature of Turbulent Ambipolar Diffusion (TAD) and a potential tool to measure B-field strengths in molecular clouds. Here we present our recent observation of $HCN/HCO^+(4-3)$ towards a massive star forming filament NGC6334, where B-field strength had been measured at regions of different scales (1pc, 0.1pc, 0.01pc) and density ($10^3 - 10^5 cm^{-3}$) before by Li et al. (2015). Our analyses demonstrate that the difference of squared velocity dispersion between ions ($HCO^+$) and neutrals ($HCN$) $\Delta\sigma^2$ is positively correlated with B-field strength, reinforcing the validity of the explanation

put forward by Li & Houde (2008) and Li et al. (2010). We will discuss its ability to measuring B-field strengths and factors that could possibly influence the linewidths.

## 3.1 Introduction

Turbulence and magnetic fields are ubiquitous in the context of star formation, ranging from the formation of Giant Molecular Clouds (GMCs) to the formation of proto-stellar discs. Magnetohydrodynamic (MHD) turbulence is expected to play an important role in the understanding of star formation. Yet, little is known about how turbulence is being dissipated at the smallest scale of turbulent cascade.

In partially ionized GMCs, neutrals are well-coupled to the B-field through collisions with ions with the exchange of momentum. Moving towards smaller scales, the decoupling of neutrals flows from plasma/B-field becomes inevitable. This notion, also known as Ambipolar Diffusion (AD), was first introduced by Mestel & Spitzer (1956) to understand how stars can be formed in strongly magnetized molecular clouds. In this strong B-field model, molecular clouds are subcritical in mass, e.g. $M < M_\phi = \phi/(2\pi\sqrt{G})$ (Cylindrical Disk) where $M_\phi$ is the critical mass, $\phi$ is the magnetic flux, and $G$ is the gravitational

constant (Nakano & Nakamura (1978)). Initially the magnetic pressure is strong enough to prevent gravitational collapse. The relative drift of neutrals towards the gravitating center through the seas of B-fields and ions, which is known as the process of Ambipolar Diffussion, results in the increase of the mass of the cloud cores and B-field strength, however with a rate slower than total mass does. Eventually, the B-field is not strong enough to halt the collapse and cores mass exceeds $M_\phi$. And star formation can proceed.

In addition to the redistribution of magnetic flux, Ambipolar Diffusion is also shown to be an important mechanism for damping MHD turbulence. The friction between ions and neutrals will damp the motion of ions at the scale set by Ambipolar Reynold numbers $R_{AD} = 1$ (Zweibel (2015)). Li & Houde (2008) suggested that the differences between velocity dispersions of coexistent ions and neutrals can possibly be the observational signature of the dissipation of turbulent energy in ions for scales smaller than $L_{AD}$. It is supported by recent two-fluid MHD simulations (e.g. Tilley & Balsara (2010), Burkhart et al. (2015)) and further observational evidences from star-forming regions (e.g. Li et al. (2010)). One important implication that brought up by Li & Houde (2008) is its potential to estimate B-field strengths

in molecular clouds which has been known to be difficult to measure. However, more evidence is needed to understand this mechanism more thoroughly.

### 3.1.1 The Theory: Turbulent Ambipolar Diffusion

In this section, we review breifly the theoretical ideas behind the TAD. MHD turbulence can be viewed as a collection of turbulent cascades of different MHD wave modes: Alfvenic/ fast/ slow waves ( Cho & Lazarian (2003)). The linear analysis on two fluid MHD equations has shown Alfven waves, which is believed to carry most of the energy of MHD turbulence (Cho & Lazarian (2003)), are damped at scales smaller than the length set by TAD: $L_{AD}$ (Balsara (1996)). Thus, the turbulent energy spectrum would decay steeply beyond this scale $L_{AD}$, owing to the dissipation of these MHD perturbations. A rough estimate of such scale can be obtained through the induction equation. The governing equation of B-fields is given by the induction equation, that is,

$$\frac{\partial \mathbf{B}}{\partial t} = \nabla \times (\mathbf{v} \times \mathbf{B}) + \eta \nabla^{\mathbf{2}} \mathbf{B} \tag{3.1}$$

where $\mathbf{B}$ is the magnetic field, $\mathbf{v}$ the velocity of the (ionized) gas, and $\eta$ the magnetic diffusivity. The magnetic Reynold number is defined as the ratio between the convective term and the dif-

fusion term in the induction equation

$$R_M = \frac{\nabla \times (\mathbf{v} \times \mathbf{B})}{\eta \nabla^2 B} \tag{3.2}$$

When $R_M \gg 1$, the diffusion term can be neglected. Therefore,the dynamics of the ions and neutrals are well coupled according to the flux freezing theorem (Zweibel, 2015). Moving towards smaller scales, ion-neutral collision will begin to compete with and eventually dominate over the restoring force of B-fields/Alfven waves. It is expected that the flux freezing approximation breaks down and the neutral flows/turbulence would detach from the B-fields and evolve hydrodynamically while the motion of plasmas would be damped out by its collision with neutrals. To account for this scenario, the corresponding magnetic diffusivity is given by

$$\eta_{AD} = \frac{B^2}{4\pi \rho_i \rho_n \gamma_{in}} \tag{3.3}$$

where $B$, $\rho_i$, $\rho_n$ are B-field strength, mass density of ions and neutrals respectively. $\gamma_{in}$ is the collision rate coefficent.

The scale at which neutrals decoupled from B-fields, the AD scale $L_{AD}$ can be estimated by comparing the relative importance of the convection term and the diffusion term in the induction equation, or setting the $R_M = 1$,

$$L_{AD} = \frac{B^2}{4\pi \rho_i \rho_n \gamma_{in} V_n} \tag{3.4}$$

where $V_n$ is the characteristic velocity at the scale $L_{AD}$. A more sophisicated model to account for the dissipation of MHD turbulence is presented by Xu et al. (2015), by considering the turbulence cascading timescale and the dissipation timescale of different MHD wave modes.

In the absence of B-fields, hydrodynamic viscosity is the dominant mechanism of the dissipation of turbulence. Its diffusivity can be estimated by:

$$\eta_{\rm hydro} = \lambda_{\rm mfp} v_{\rm th} \approx 2 \times 10^{17} (\frac{n}{100 cm^{-3}})^{-1} (\frac{T}{10K})^{\frac{1}{2}} cm^2 s^{-1} \quad (3.5)$$

where $v_{th}$ is the thermal velocity of the fluid and $\lambda_{\rm mfp}$ is the mean free path of the fluid.

In typical condition of molecular clouds, (e.g. $B \approx 0.2mG, n_n \approx 10^4 cm^{-3}$, ionization fraction $10^{-7}$, neutral ion collision frequency: $\gamma_{in} \approx 1.5 \times 10^{-9} n_{\rm n} s^{-1}$, $T = 10K$), the effective hydrodynamic viscosity and the magnetic diffusivity originated from ambipolar diffusion are of the order $10^{16} cm^2 s^{-1}$ and $10^{22} cm^2 s^{-1}$ respectively. It is therefore not surprised that ambipolar diffusion will play a more important role in the dissipation of magnetized turbulence in molecular clouds.

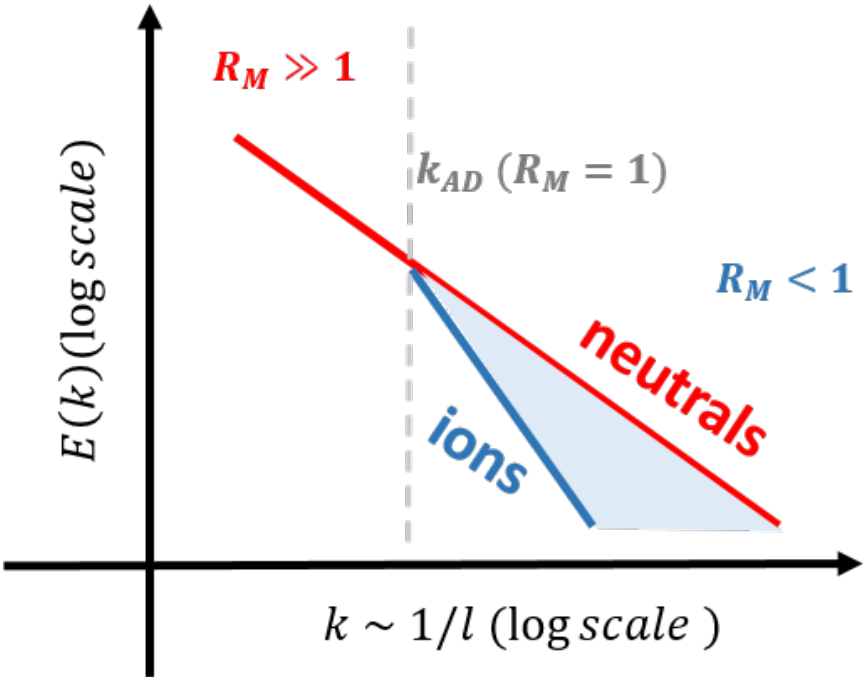


Figure 3.1: A Log-Log plot of the turbulent energy spectrum (energy density per unit wavenumber) versus scale in arbitrary units for demonstrative purposes. The velocity dispersion/linewidth of the tracers measured at scale $L$ is proportional to the integration of the turbulent energies contributed by all eddies of sizes smaller than L.

### 3.1.2 Observational Evidence of TAD

As a result of the dissipation of the turbulent energy in the ions in the presence of TAD, the linewidth of ions is expected to be smaller than that of the neutrals. This can be understood more easily with the help of Figure 3.1. The decoupling between neutrals and B-fields happens at scales smaller than $L_{AD}$ where $R_M < 1$. At scales where $R_M \gg 1$, neutrals and ions should be well-coupled to each other thanks to the flux-freezing phenomenon. When $R_M < 1$, turbulent energy possessed by ions which are tied to the B-fields are expected to be dissipated steeply. As for neutrals, the turbulent cascade would evolve hydrodynamically with the energy cutoff scale set by the hydrodynamic friction.

An observed spectral line width is usually an indicator of how turbulent the molecular cloud is. It depends on the volume traced by the telescope beam and the depth of the emitting source. Any turbulent eddies of scales smaller than the characteristic size $L$ of the emitting volume contributes to the observed level of turbulence/ linewidth $\sigma$. Mathematically, it can be expressed as an integration of turbulent energy spectrum from the

smallest scale to the characteristic size $L$:

$$\sigma^2(L) \propto \int_{2\pi/L}^{\infty} E(k)dk = bL^n \tag{3.6}$$

for a power law energy spectrum, e.g. $E(k) \propto k^{-n-1}$ (For Kolmogorov Type Turbulence, $n = 2/3$). Here $k$ and $E(k)$ denotes the wavenumber and the energy spectrum. The square of velocity dispersion $\sigma^2$ is illustrated as a function of scale $L$ for neutrals (red) and ions (blue) in Figure 3.2, assuming the steep decay of the energy spectrum of ions for scales smaller than $L_{AD}$ (Figure 3.1).

The area of the shaded region in Figure 3.1 corresponds to the observed $\Delta\sigma^2$ in Figure 3.2. The $\sigma$ saturates to the thermal speed $v_{th}$ as $\lambda$ is reached. When the size $L$ is larger than the $L_{AD}$, $\Delta\sigma^2$ does not vary with increasing $L$. The difference of the linewidth between these two species can be expressed with the knowledge of the turbulent energy spectrum and the $L_{AD}$

$$\Delta\sigma^2 = \begin{cases} b(L_{AD})^m - c(L_{AD})^{m_{dis}}, & \text{if } L \geq L_{AD} \\ bL^m - cL^{m_{dis}}, & \text{if } L < L_{AD} \end{cases} \tag{3.7}$$

with $m$ being the scaling exponent of the neutrals and $m_{dis}$ being the scaling exponent of ions for scales smaller than $L_{AD}$.

Li & Houde (2008) has assumed $L_{AD}$ set the cutoff scale for the turbulent energy spectrum of the ions and thus ignored

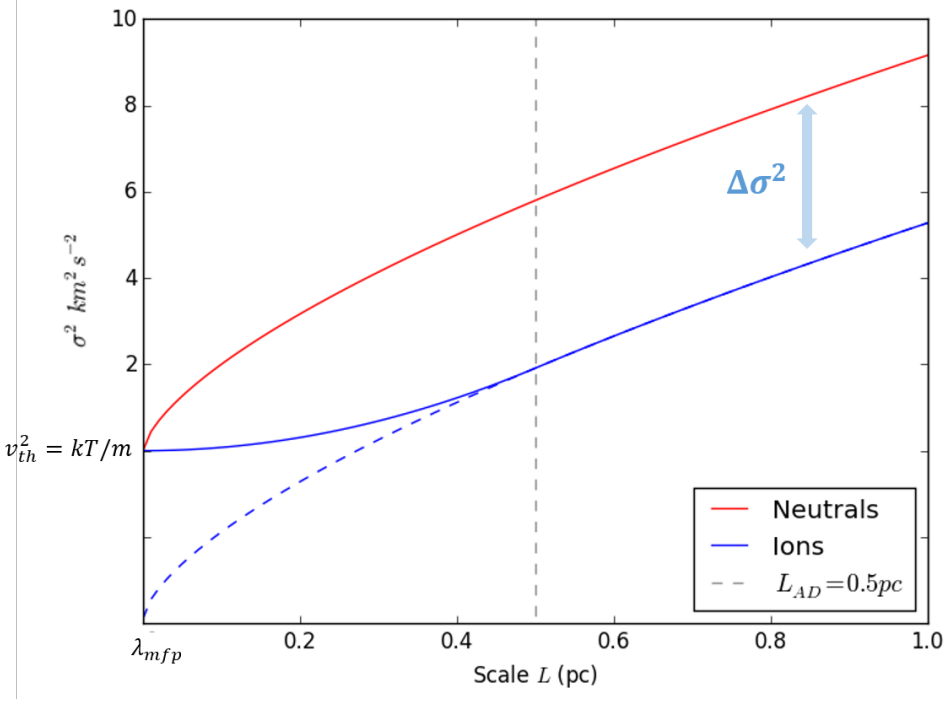


Figure 3.2: The square of velocity dispersion $\sigma^2$ as a function of scale $L$. The red line and blue line shows the trend traced by neutrals and ions respectively. The blue dashed line is downshifted by the line width difference measured at larger scale $\Delta\sigma^2$ for $L \gg L_{AD}$. Here we set $m = 0.67$, $m_{dis} = 2.0$, $L_{AD} = 0.5pc$.

the latter term. We note that in recent 2-fluid simulation by Burkhart et al. (2015) demonstrated that the turbulent energy in ions survived to scales much smaller than $L_{AD}$. This hints at the assumption made by Li & Houde (2008) may be over-simplified. Instead of assuming the $L_{AD}$ as the sharp cutoff for the ions' turbulent spectrum, we will derive the respective energy spectrum for the two species with the method developed by Lazarian & Pogosyan (2006) for the relatively diffuse filaments of NGC 6334.

## 3.2 Observation Data

The $HCN(4-3)$ and $HCO^{+}(4-3)$ observations of NGC6334 were made using MAC XF-type digital specto-correlator on the Atacama Submillimeter Telescope Experiment (ASTE), a 10-m dish located at Pampa La Bola in the Atacama Desert of Chile, at an altitude of 4800 m. $HCN(4-3)$ (354.505 GHz) and $HCO^{+}(4-3)$ (356.734 GHz) lines were simultaneously observed in the two sidebands with a spectral resolution of $0.11\,kms^{-1}$ with a noise level of $0.1\,K$ over the velocity channel. The observations were made in 2015 September, remotely from an ASTE operation room in the Mitaka campus of the National Astronomical Observatory of Japan. NGC 6334 (I), (IN) and (III)

with recent B-field estimate by Li et al. (2015) were mapped with the OTF observing mode. The data are reduced by the NOSTAR package from Sawada et al. (2008).

These two tracers are chosen as they are observed to be well-correlated spatially in previous observations towards star forming regions of different environments (e.g. Houde et al. (2000), Li & Houde (2008), Lo et al. (2009)). This is in agreement with our sets of data. Figure 3.3 and 3.4 show the integrated intensity map of both $HCN$ and $HCO^+$, the contours and the colorplots are highly correlated spatially. This indicates that we are comparing the neutrals and ions that trace the similar volume of the molecular clouds.

## 3.3 The Systematic Linewidth difference between Ions and Neutrals

The resulting data cubes were processed with Python script. We fitted Gaussian profiles

$$I(v) = Ae^{\frac{-(v-v_0)^2}{2\sigma_v^2}} \tag{3.8}$$

to the two species $HCN/HCO^+$ to determine the corresponding velocity dispersion $\sigma_v$, and thus the squared velocity dispersion difference between $HCN/HCO^+$ $\Delta\sigma^2$, with the curvefit func-

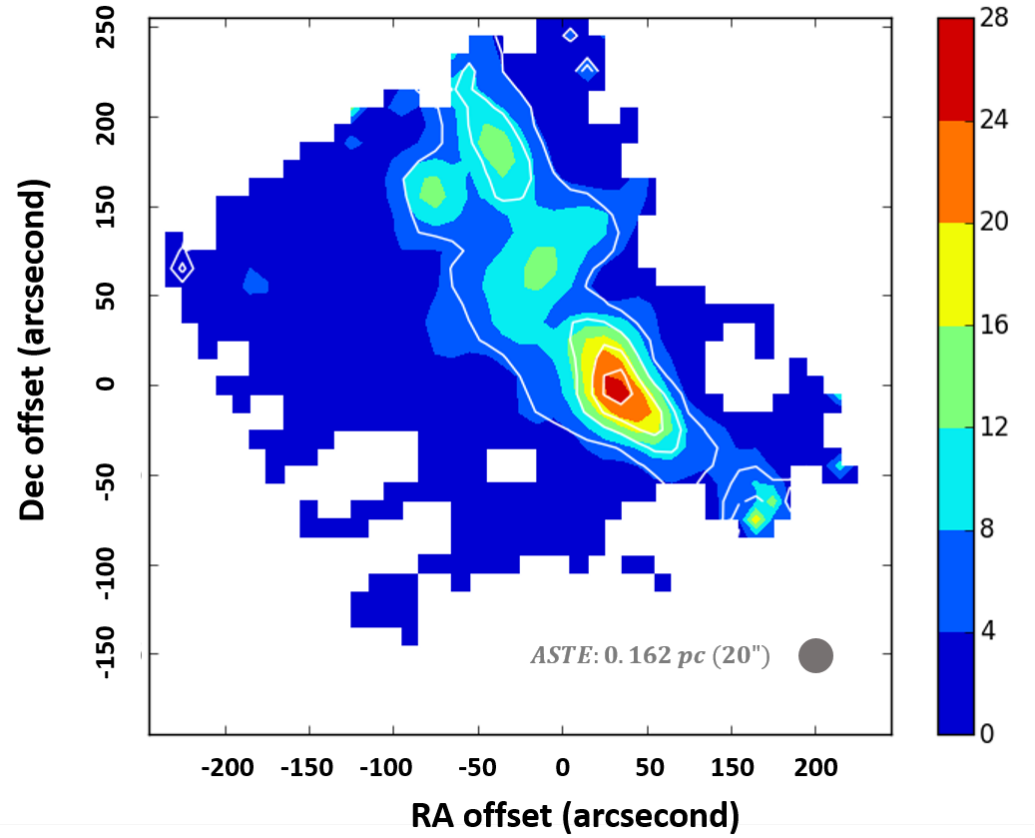


Figure 3.3: Integrated Intensity maps of HCN (white contours) and $HCO^+$ (colored plot) in NGC6334 III. The reference coordinate of this map is $17h20m36.8s, -35°51'26''$. The highest contour levels corresponds to an integrated intensity of 20 $Kkms^{-1}$; each following levels are lowered by $5Kkms^{-1}$ accordingly. The colorbar is in the scale of $Kkms^{-1}$.

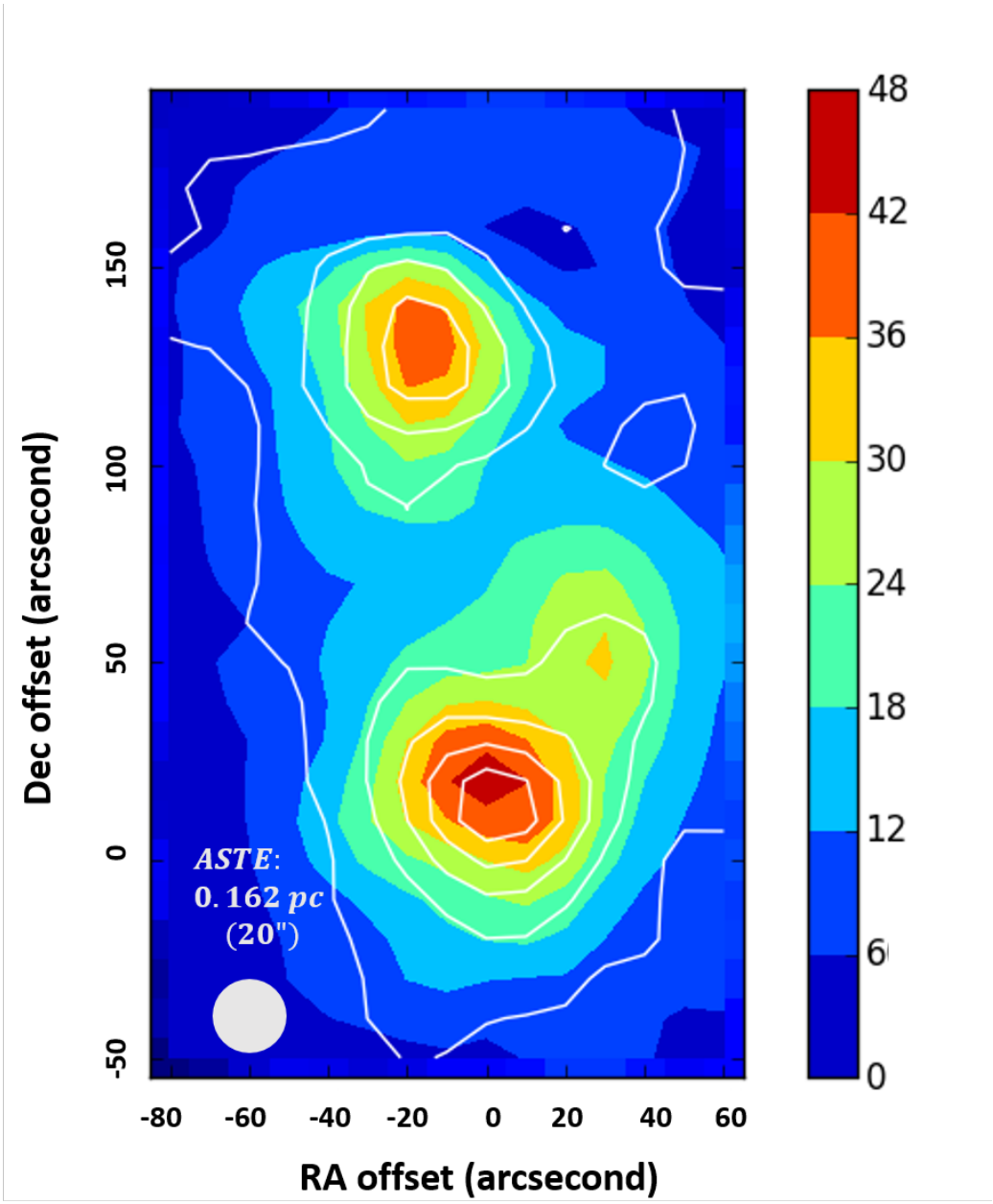


Figure 3.4: Integrated Intensity maps of HCN (white contours) and $HCO^+$ (colored plot) in NGC6334 (I) and (IN) . The reference coordinate of this map is $17h20m53.3s, -35°47'21''$. The highest contour levels corresponds to an integrated intensity of $50\,Kkms^{-1}$; each following levels are lowered by $10\,Kkms^{-1}$ accordingly. The colorbar is in the scale of $Kkms^{-1}$.

tion from Scipy optimize module. We noted that in dense regions (e.g: $n \geq 10^5 cm^{-3}$), the two lines get optically thick. In these cases, the self-absorbed peaks are avoided for the Gaussian fitting. The column density of $HCO^+$ and $HCN$ are estimated by integrating the spectral line approximated by the Gaussian fitting profile. The best-fit profiles are shown together with the observed spectral lines for regions in Figure 3.5, 3.6, 3.7, 3.8.

### 3.3.1 The positive correlation between $\Delta\sigma^2$ and B-field strength

Figure 3.9 compared the average $\Delta\sigma^2$ and the corresponding B-field strength derived by Li et al. 2015 Li et al. (2015). The estimate of B-field strength was based on the assumption of the balance between gravitational force and magnetic force, and therefore should only be valid between the clumps/cores. In producing Figure 3.9, we restricted our data samples to regions between the clumps/cores. As for NGC 6334 (IN), the resolution (0.02 pc) attained by previous SMA observation (Fig. 2c. Li et al. (2015)) is not resolvable by this ASTE observation ($\sim 0.16pc$). Only the peak region of core IN of the size ($\sim 0.2pc \times 0.2pc$ ; the map size of previous SMA observations) is included for this analysis. It is clear to see that they are

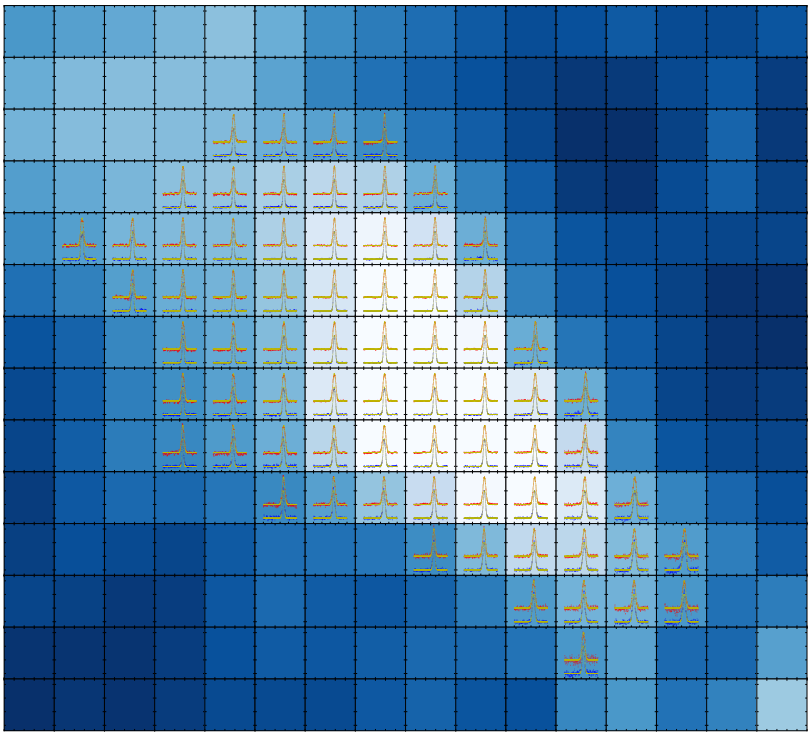

Figure 3.5: The result of the Gaussian Profile fitting for region NGC 6334 (III). The red and blue scatter plot are $HCN$ and $HCO^+$ respectively. Fitting results are plotted as the yellow lines. The intensity of these lines are normalized to the peak for better illustrations. The background color shows the integrated intensity of $HCO^+$.

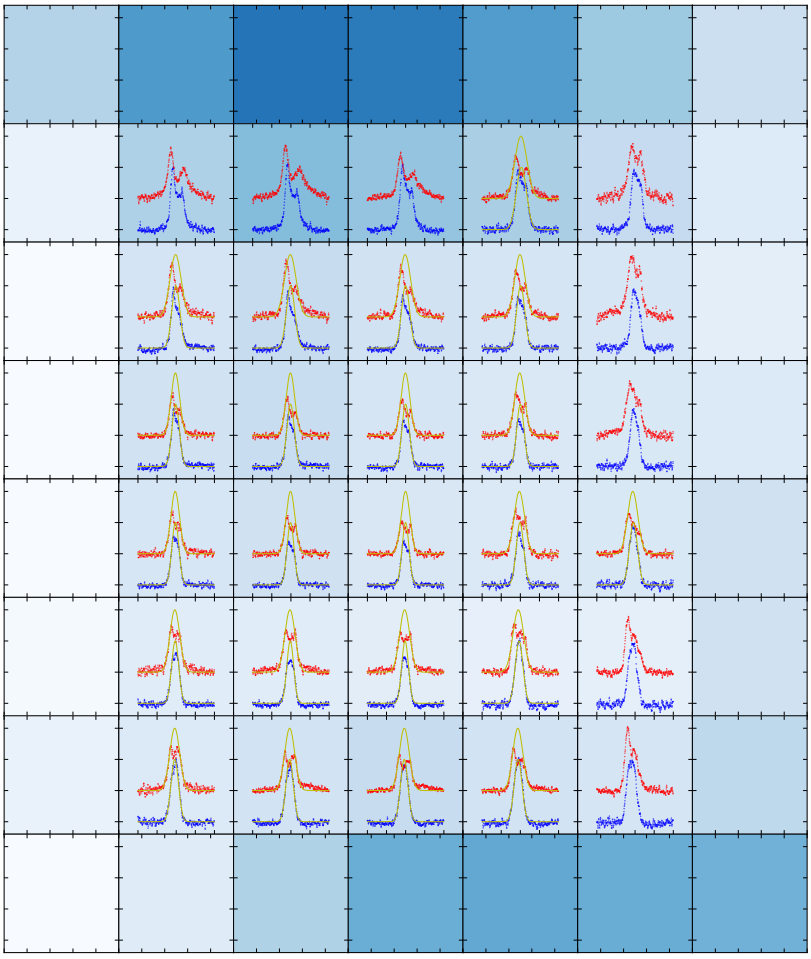

Figure 3.6: Same as Figure 3.5 but for regions between NGC 6334 (I) and (IN)

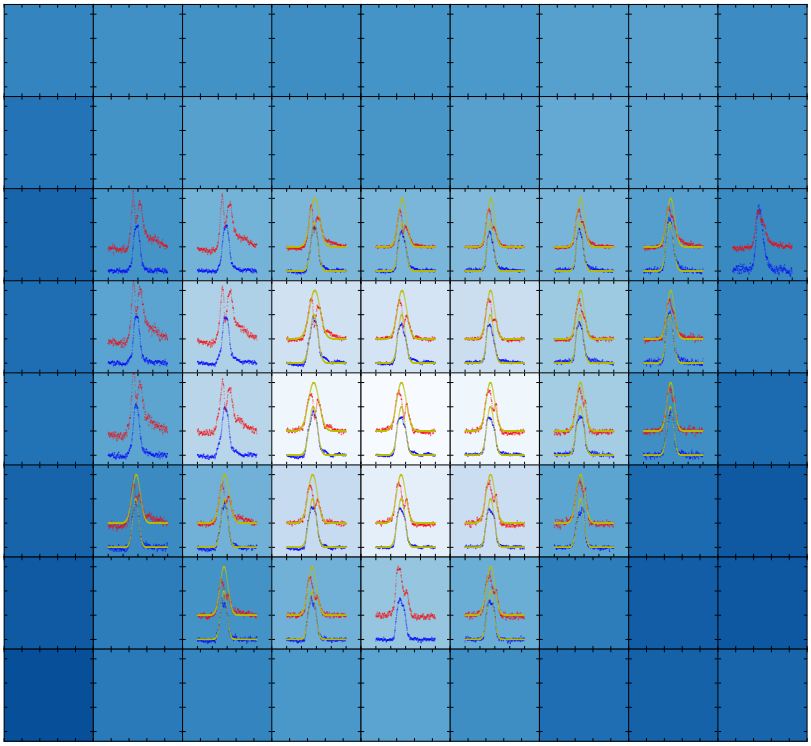

Figure 3.7: Same as Figure 3.5 but for regions NGC 6334 (I)

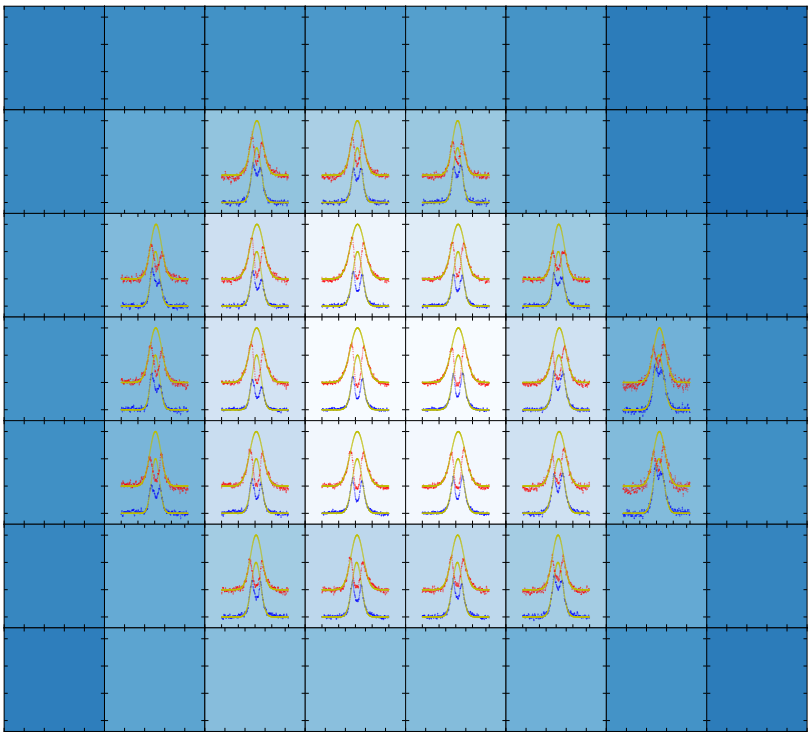

Figure 3.8: Same as Figure 3.5 but for regions NGC 6334 (IN)

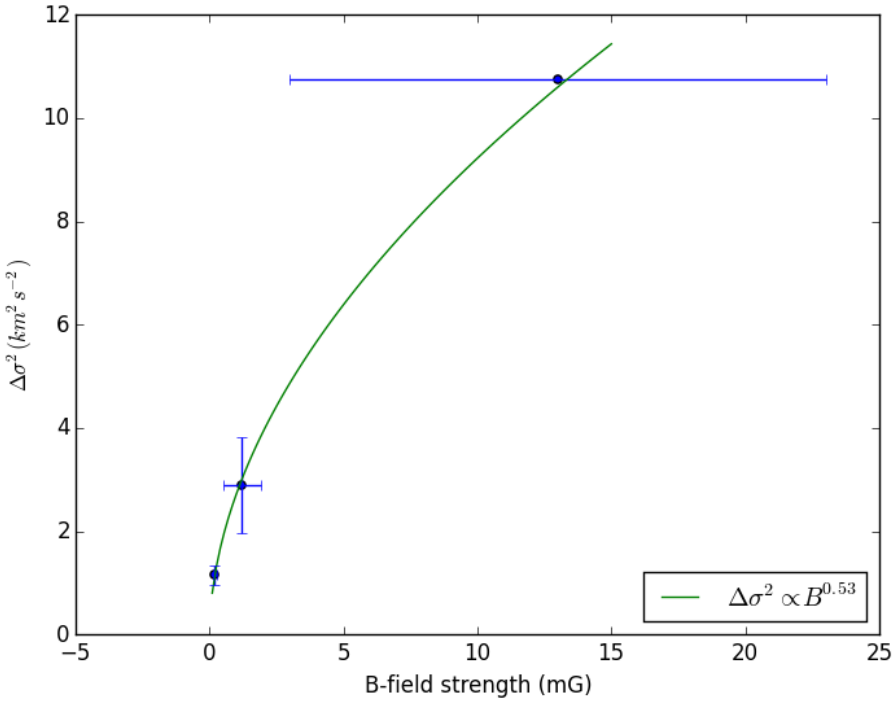


Figure 3.9: The average difference of the squared velocity dispersion between $HCN$ and $HCO^+$ or $\Delta\sigma^2$ as a function of B-field strength. It can be described by a power-law $\Delta\sigma^2 \propto B^{0.53}$. The errobar of $\Delta\sigma^2$ is given by the standard deviation of the $\Delta\sigma^2$ within each sample region.

positively correlated.

### 3.3.2 The dependence of $\Delta\sigma^2$ with column density

The turbulent energy/linewidth depends on the volume traced by the telescope beam size and the line of sight dimension. Despite the larger depth probed by pointings towards regions with higher column density, the linewidth difference should not be affected as long as the B-field strength does not vary from regions to regions since $\sigma^2$ varies in the same manner for both ions and neutrals for length scales larger than $L_{AD}$ (See Figure 3.2). The $\Delta\sigma^2$ and column density probed by $HCO^+$ is shown in Figure 3.14. At relatively low density region NGC 6334 III, the average $\Delta\sigma^2$ are $0.998 \pm 0.286\, km^2 s^{-2}$ and are roughly constant with the integrated intensity of $HCO^+$. The uniform density of B-field lines mapped by polarization data Li et al. (2015) suggested B-field strength does not vary within NGC 6334 (III). The $\Delta\sigma^2$ in the region between the clumps (I) and (IN) is $2.90 \pm 0.922\, km^2 s^{-2}$ and is systematically higher than that from (III) despite they are probing roughly the same column density. This could possibly due to the higher B-field strength (I)/(IN) hosts. TAD predicts a larger ambipolar diffusion scale $L_{AD}$ for (I)/(IN) and therefore a larger difference in the $\Delta\sigma^2$.

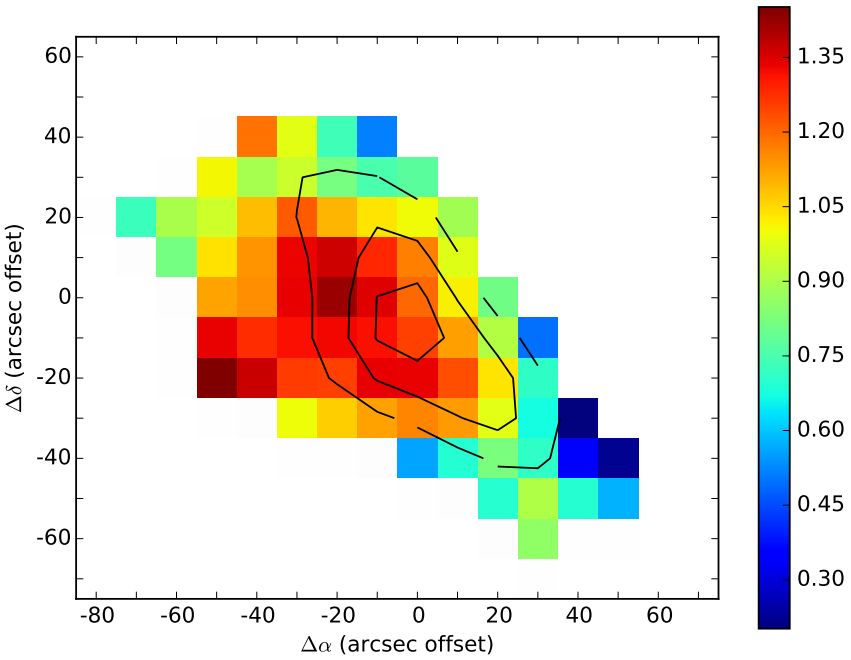


Figure 3.10: The colormap demonstrates the $\Delta sigma^2$ in the unit of $km^2 s^{-2}$. The column density of $HCO^+$ is overlapped onto the colormap.

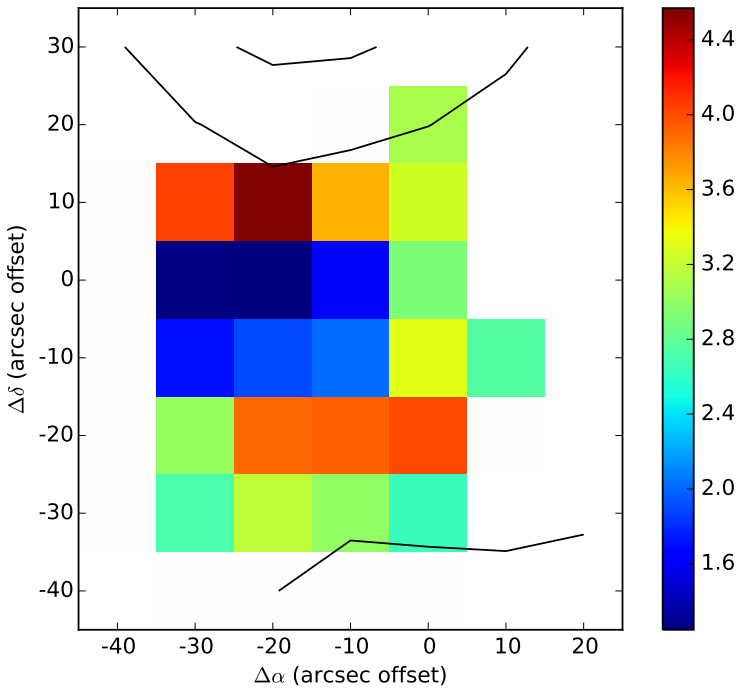


Figure 3.11: Same as Figure 3.10 but for regions between NGC 6334 (I) and (IN)

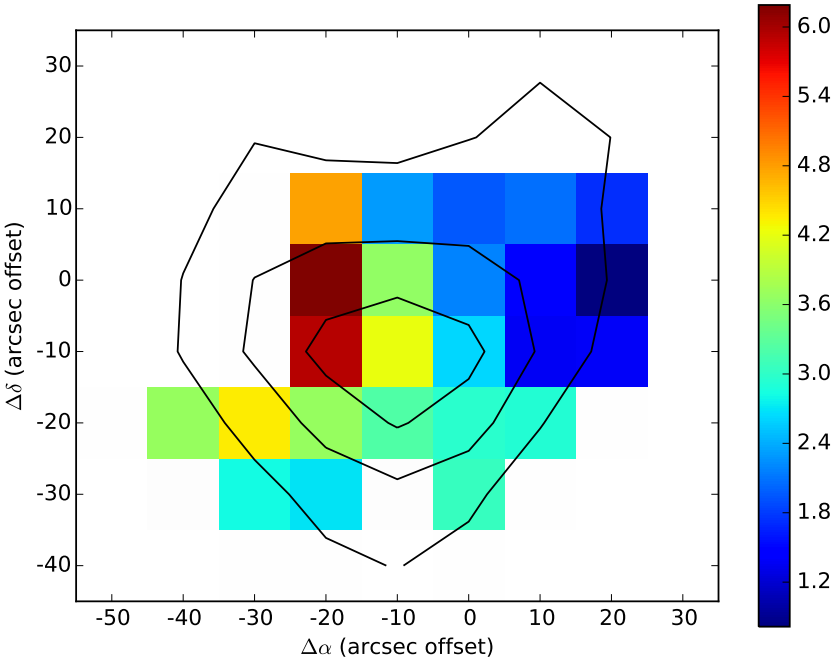


Figure 3.12: Same as Figure 3.10 but for regions NGC 6334 (I)

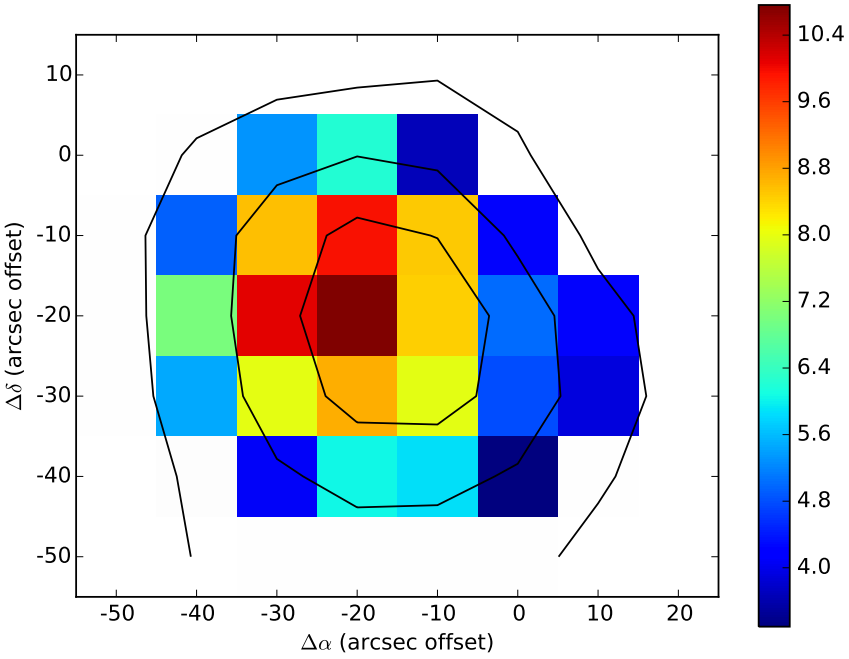


Figure 3.13: Same as Figure 3.10 but for regions NGC 6334 (IN)

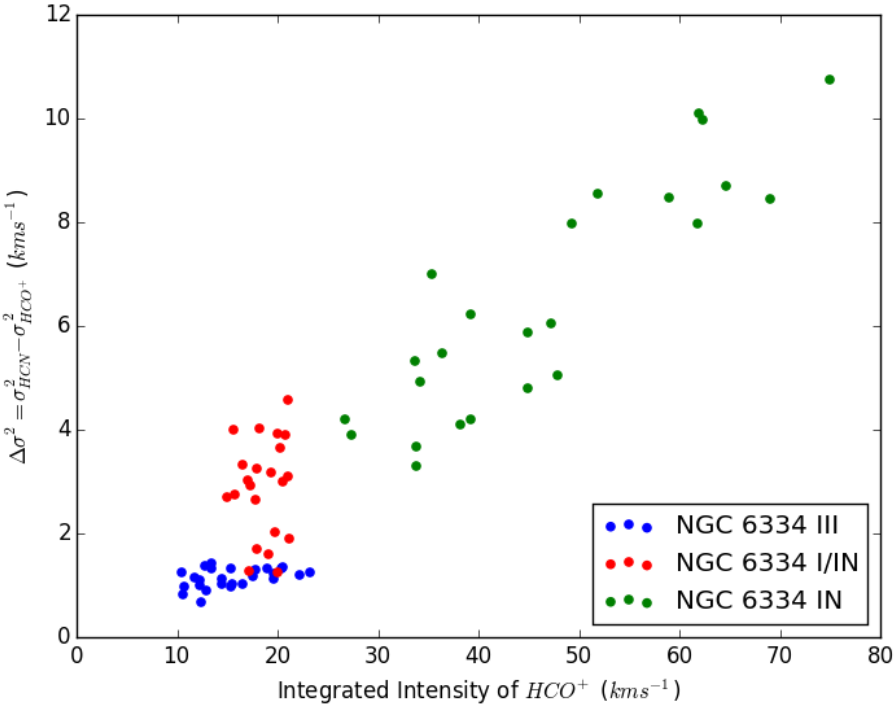


Figure 3.14: $\Delta\sigma^2$ and column density probed by $HCO^+$.

While in the vicinity of NGC 6334 (IN), the $\Delta\sigma^2$ is observed to increase with integrated intensity ($25 - 70\,Kkms^{-1}$). Hourglass B-field morphology was mapped with SMA towards the NGC 6334 (IN), suggesting the onset of gravitational collapse under the support of Lorentz force. The compression of B-field lines towards the gravitating center is expected to increase the B-field strength as a function of gas density (e.g. $B \propto \rho^{2/3}$ for isotropic collapse Crutcher et al. (2010) ). Pointings towards higher column density would intercept regions with higher B-field strength and should on average have a larger $L_{AD}$. However, we have to note that both $HCN$ and $HCO^+$ are heavily self-absorbed towards NGC 6334 (IN), the high optical depth may lead to the line broadening.

## 3.4 Do ions and neutrals really share different energy spectrum?

### 3.4.1 Lower Envelope of $\sigma^2$ distributions (Ostriker et al., 2001)

This method was adopted in Li & Houde (2008) and later in Hezareh et al. (2010) and Hezareh et al. (2014) to derive the turbulent energy spectrum. In order to understand how $\sigma^2$ varies

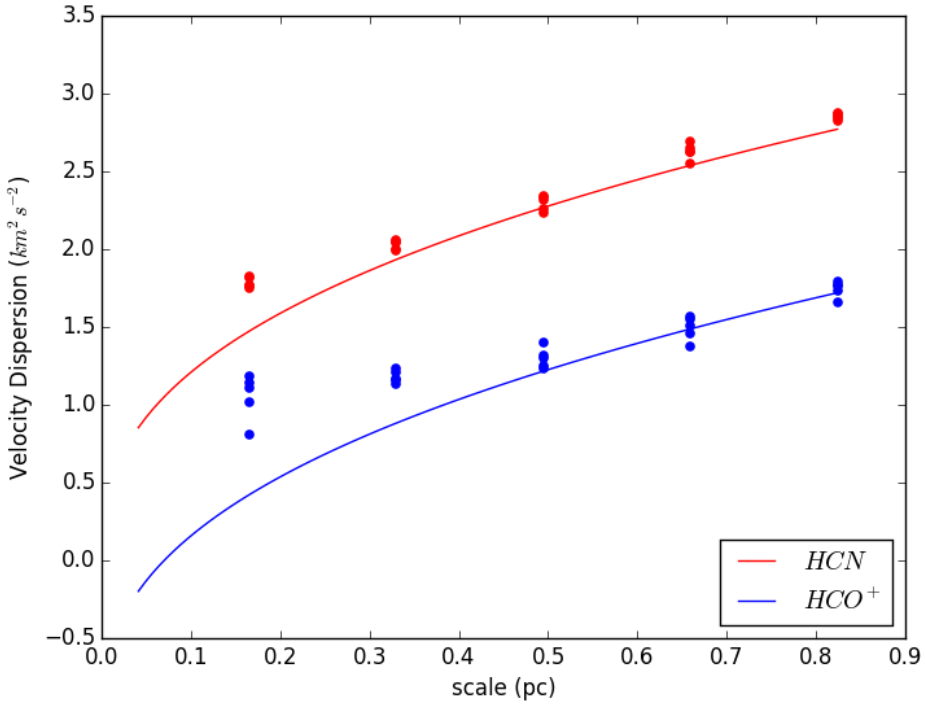


Figure 3.15: The lower envelope of the squared velocity dispersion of $HCN$ and $HCO^+$ as a function of Beam size $R$.

as a function of length scales, the spectral data cube is first coarse-grained to different resolutions/beam size as in Figure 3.15. The underlying turbulent velocity spectrum can be well-recovered by fitting the lower envelope of such velocity dispersion distributions, according to the simulation experiment performed by Ostriker et al. (2001). The method relies on the idea that the lower envelope of the $\sigma^2$ distribution traces regions that sample the shortest line of sights, such that the change in the beam size dominates the variation in the measured $\sigma^2$.

As the $\sigma^2$ of $HCO^+$ might be affected by the local variation in the B-field strength, the lower envelope of $\sigma^2$ might not faithfully reveal the information about the depth probed by the tracers. We first sample the lower envelope of $\sigma^2$ of $HCN$ as a function of (synthetic) beam size, and locate the pointings where $HCN$ samples the shortest line of sight. We then compare the $\sigma^2$ of $HCO^+$ from these locations.

The lower envelope of HCN can be well described by a power law fitting for $R \geq 0.3\,pc$ as shown in Figure 3.15:

$$\begin{aligned} \sigma_{HCN}(R)^2 &= 2.99 \left(\frac{R}{1pc}\right)^{0.393} km^2 s^{-2} \\ \sigma_{HCO^+}(R)^2 &= 2.99 \left(\frac{R}{1pc}\right)^{0.393} - 1.05\, km^2 s^{-2} \end{aligned} \tag{3.9}$$

We interpret the deviation of the $\sigma^2$ at $R \approx 0.16\,pc$ for $HCN$ and $R \leq 0.5pc$ for $HCO^+$ as the saturation of the $\sigma^2$ due to the finite line-of-sight probed by the tracers. The different 'saturation scale' for the two species could be explained by their different excitation condition. The critical density for exciting $HCO^+(4-3)$ transition is $\sim$ 4.7 times lower than that for exciting $HCN(4-3)$. $HCO^+$ is capable of tracing more diffuse regions and should probe a longer line of sight depth than $HCN$ does. Here we demonstrate the effect of line of sight depth on the measured $\sigma^2$ in Figure 3.16 with a simple model

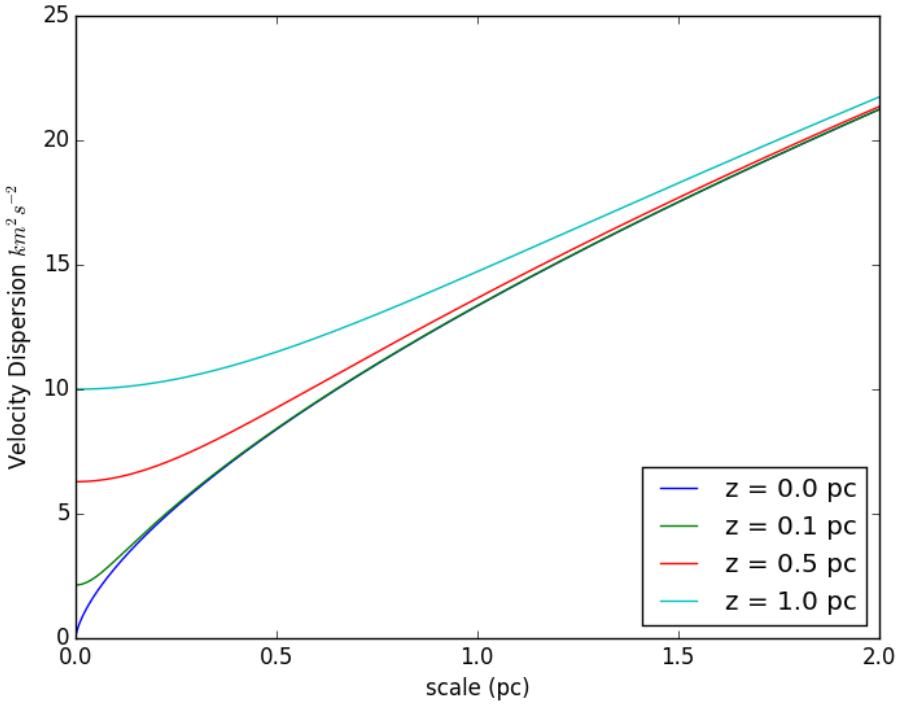


Figure 3.16: The dependence of $\sigma^2$ as a function of beam size $R$ on the line of sight scale $z$

$\sigma^2 \propto (\sqrt{R^2 + z^2})^m$, with $R$ being the beam size, $z$ being the line of sight depth and $m$ being the scaling exponent of turbulence. When the line of sight depth $z = 0\,pc$, the variation of $\sigma^2$ dominates by the change in beam size. This is the ideal scenario where this lower envelope method works best. For models with $z > 0\,pc$, when the beam size $R \leq z$, the $\sigma^2$ saturates to the $\sigma^2$ set by the line of sight scale $z$. The scaling of $\sigma^2$ recovers the trend traced by the blue lines for beam size with $R \geq z$.

Figure 3.16 might also explain why the slopes inferred from

this method Ostriker et al. (2001) to observation data ( Li & Houde (2008), Hezareh et al. (2010), Hezareh et al. (2014)) are consistently shallower than the expected scaling (Kolmogorov: $m = 2/3$; Compressible Turbulence: $m = 1$). Considering scales where $R \approx z$, the slope/scaling inferred from this plot is always shallower than the actual spectral index. As observers for most of the time has no accurate information about the line of sight depths, it is hard to determine whether we are in the regime where $R \gg z$ or $R \approx z$. Moreover, the inhomogeneous density structures along the line of sight could also affect the lineshape/linewidth. This renders the application of this method to observational data problematic.

### 3.4.2 Velocity Coordinate Spectrum (Lazarian & Pogosyan, 2006)

The Velocity Coordinate Spectrum (VCS) technique based on the study of the intensity fluctuations/ spectral lines along the velocity axis. The theoretical prediction of such power spectrum is backed by the assumption of: a power law like spectrum for both turbulent velocity and the density distribution. This method has been applied by Padoan et al. (2009), Chepurnov et al. (2010), Chepurnov et al. (2015). It has been proven suc-

cessful in retrieving statistical description of turbulences in simulation data cubes (Padoan et al., 2009; Chepurnov & Lazarian, 2009).

VCS is defined to be the power spectrum of the intensity fluctuations in the velocity coordinate along fixed line of sight:

$$P_{VCS}(k_v) = |\int_{-\infty}^{\infty} I(v)e^{ik_v v}dv|^2 \tag{3.10}$$

where $I_v$ is the spectral line intensity at velocity $v$ and $k_v$ is the wavenumber in the velocity coordinate (e.g., $k_v = \frac{2\pi}{v}$). It depends on the angular resolution of the telescopes. The velocity power spectrum can be recovered by investigating the change of VCS from high to low angular resolution as eddies of different size contributes to a different degree to VCS.

Lazarian & Pogosyan (2006) shows that the expression of VCS is of the following form

$$P_1(k_v) = \tilde{f}^2(k_v)P_0 \int C_\epsilon(r)g(r)dr \exp(-\frac{-k_v^2}{2}D_{vz}(r)) + N_0 \tag{3.11}$$

where $\tilde{f}$ is the fourier transform of the maxwellian distribution which depends on temperature,$P_0$ is the spectrum amplitude, $C_\epsilon(r)$ is the density correlation function, $g(r)$ is the geometric factor that accounts for the beam pattern and structures along the line of sight, $D_{vz}(r)$ is the structure function of the turbulent

velocity component along the line of sight and $N_0$ is a constant which depends on the noise level.

The temperature dependent term and the density correlation function term can be determined independently before the fitting of VCS. The temperature of this filament is of the order $20 - 30\,K$ (André et al., 2016). This translates to a thermal velocity of $0.1 kms^{-1}$ for both $HCN$ and $HCO^+$. It can be shown that the inclusion of this term would not change the fitting for the velocity range that we are interested in (See discussion part and Figure 3.21).

The density correlation function can be derived from the study of the 2D spatial power spectrum of the column density map as pointed out by Lazarian & Pogosyan (2000). The power spectrum would be in the form of $P_{2D}(K) \propto K^{-3+\gamma}$. The density correlation function is termed steep when $\gamma < 0$ and shallow when $\gamma > 0$. In fact, Lazarian & Pogosyan (2006) showed that the contribution of the density fluctuations has a weak dependence on the VCS when the density correlation function is steep. Here we showed the spatial power spectrum of the column density map from both $HCN$ and $HCO^+$ (Figure 3.17). The two species shared almost an identical trend which is again an indication of the high correlation between the two species. Since

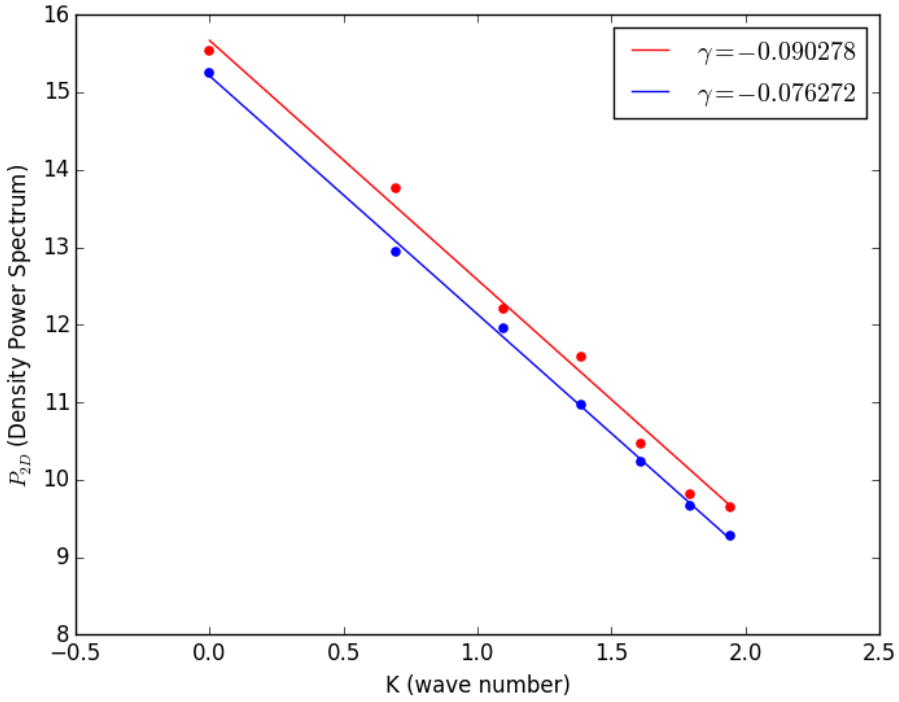


Figure 3.17: The 2D column density power spectrum of $HCN$ and $HCO^+$ in log-log scale. $\gamma < 0$ corresponds to a steep density power spectrum. The density correlation function $C_\epsilon$ can be factored out from the integration of the VCS. This simplifies the fitting procedures.

$\gamma < 0$ for both species, the density correlation term $C_\epsilon(r)$ can be factored out from the integration that follows.

VCS can now take a simpler form

$$P_{vcs}(k_v) = P_0 \int g(r)dr \exp(-\frac{-k_v^2}{2} D_{vz}(r)) + N_0 \qquad (3.12)$$

Free parameters needed to model the VCS reduces to $P_0$, $N_0$, $D_{vz}(r) =< (v_z(x) - v_z(x+r))^2 >$.

To begin with, the power spectrum of $HCN$ and $HCO^+$

(taken along the velocity axis) are first averaged spatially for all the line of sights respectively to lower the noise. We focus our analyses mostly towards the core region of NGC 6334 (III) as other region of this filament host multiple density structures along the velocity axis. In view of the description by the schematic Figure 3.1 and the simulation results from Burkhart et al. (2015), we understand the turbulent spectrum of $HCO^+$ cannot be simply described by a single spectral index turbulent spectrum. Therefore, in our modelling of VCS, we included one more spectral index to describe the damping effect induced by TAD for scales smaller than $L_{AD}$.

Assume a pure solenoidal turbulence spectrum, the structure function of the turbulent velocity component along the line of sight can be written as:

$$HCN : D_z(r,z) = \begin{cases} Cr^m[1+\frac{m}{2}(1-\frac{z^2}{r^2})], & \text{if } 0 \le r \le L_{cut} \\ C(L_{cut})^m[1+\frac{m}{2}(1-\frac{z^2}{r^2})], & \text{otherwise} \end{cases} \tag{3.13}$$

$$HCO^+ : D_z(r,z) = \begin{cases} C_{dis} r^{m_{dis}}[1 + \frac{m_{dis}}{2}(1 - \frac{z^2}{r^2})], & \text{if } 0 \leq r \leq L_{AD} \\ D + Cr^m[1 + \frac{m}{2}(1 - \frac{z^2}{r^2})], & \text{if } L_{AD} \leq r \leq L_{cut} \\ D + C(L_{cut})^m[1 + \frac{m}{2}(1 - \frac{z^2}{r^2})], & \text{otherwise} \end{cases} \tag{3.14}$$

The turbulence spectrum saturates at scales larger than the energy cut-off scale $L_{cut}$. The term $Cr^m$ accounts for the scaling of the velocity dispersion $V$ of the eddies of sizes r while the term $[1 + m/2(1 - z^2/r^2)]$ accounts for the projection of velocity components onto the line of sight direction. $C_{dis}$ and $D$ are set by the boundary condition imposed by the continuity of the turbulent energy spectrum at the scale $L_{AD}$, for a given $C$, $m$, $m_{dis}$.

$$\begin{aligned} C_{dis} = &\quad C\frac{m}{m_{dis}}(L_{AD})^{m-m_{dis}} \\ D = &\quad \frac{C(m - m_{dis})}{m_{dis}}(L_{AD})^m \end{aligned} \tag{3.15}$$

Input parameters for fitting VCS are listed in Table 3.1. The modelling of VCS begins by first fitting the power spectrum of $HCN$ as it has the least input parameters compared to $HCO^+$ and returns the information of the turbulent spectrum regarding larger scales (e.g. $C$, $m$, $L_{cut}$). These parameters are used in

| | $HCN$ | $HCO^+$ |
|---|---|---|
| Spectrum Amplitude | $\mathbf{P_0}$ | $\mathbf{P_1}$ |
| Constant (noise) | $\mathbf{N_0}$ | $\mathbf{N_1}$ |
| Spectral Index ($L \geq L_{AD}$) | $\mathbf{m}$ | $m$ |
| Velocity Dispersion ($L \geq L_{AD}$) | $\mathbf{C}$ | $C$ |
| Energy Cut off Scale | $\mathbf{L_{cut}}$ | $L_{cut}$ |
| Spectral Index ($L < L_{AD}$) | \ | $\mathbf{m_{dis}}$ |
| Decoupling Scale | \ | $\mathbf{L_{AD}}$ |

Table 3.1: Input parameters for fitting VCS to the power spectrum of $HCN$ and $HCO^+$. The bold face parameters are the free fitting parameters.

the further fitting of the spectrum of $HCO^+$. The resultant best fit parameters and their respective one standard deviation error returned from the scipy optimize module are listed in Table 3.2. The error of $C_{dis}$ and $D$ are estimated from the standard error propogation. The best fit curve is shown together with the power spectrum of the two species in Figure 3.18.

The spectral lines under the framework of VCS can be represented as (See Appendix for details):

$$< I(\vec{v}) >= \frac{\rho L}{\sqrt{\pi(D_z(L))}} e^{-\frac{v^2}{D_z(L)}} \tag{3.16}$$

The squared linewidth of the spectral lines $\sigma^2$ differed from $D_z$ by a factor of two, e.g. $\sigma^2 = D_z(L)/2$. The $\sigma^2$ distribution of $HCO^+$ traces a steeper slope than that of $HCN$:

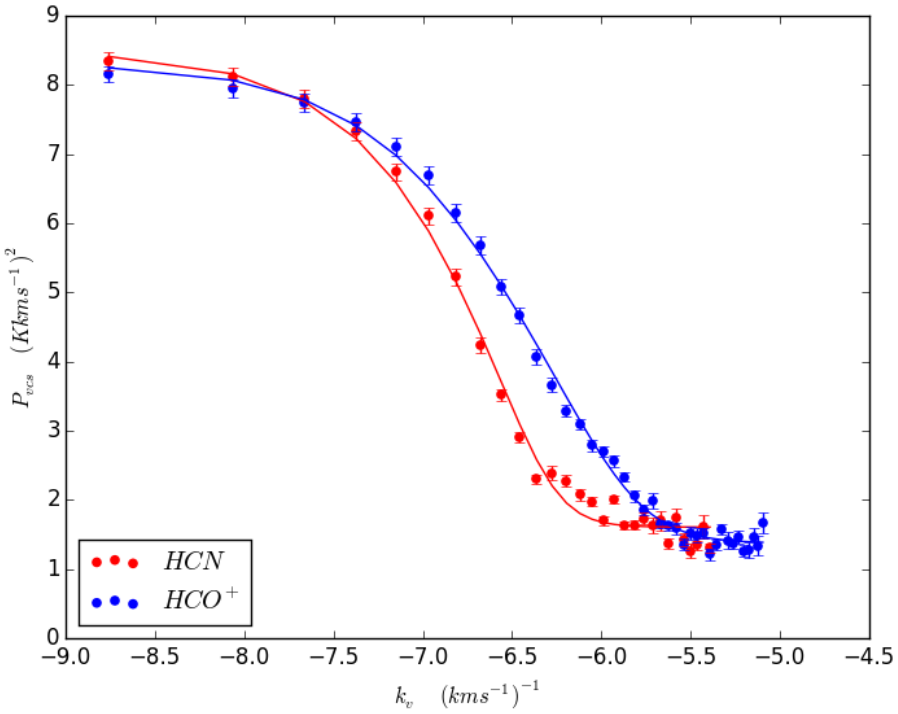


Figure 3.18: The best fit of VCS (solid line) is overlayed on the power spectrum of $HCN$ and $HCO^+$ (scatter plot). The errobars is the standard deviation of the mean value from taking spatial average.

| $HCN$ | | $HCO^+$ | |
|---|---|---|---|
| $C$ | $9.16 \pm 1.47\, km^2 s^{-2}$ | $m_{dis}$ | $1.01 \pm 0.049$ |
| $m$ | $0.655 \pm 0.0935$ | $L_{AD}$ | $0.484 \pm 0.158\, pc$ |
| $L_{cut}$ | $1.26 \pm 0.112 pc$ | $C_{dis}$ | $7.69 \pm 2.07\, km^2 s^{-2}$ |
| | | $D$ | $2.0 \pm 1.35\, km^s s^{-2}$ |

Table 3.2: The best fit result returned from fitting VCS to the power spectrum of $HCN$ and $HCO^+$

$m_{dis} = 1.01 > m = 0.655$ This corresponds to a steeper decay of turbulent energy of the charged species and is in agreement with the theoretical prediction which anticipates the dissipation of turbulent energy beyond the $L_{AD}$. However, the turbulent energy of $HCO^+$ is not dissipated totally as soon as it reaches the $L_{AD}$ as suggested by Li & Houde (2008) and Xu et al. (2015). The derived energy cutoff scale $L_{cut} = 1.26\,pc$ is roughly equal to the size of the filaments $\approx 1.5pc$. It is an indication that the turbulence is driven from the largest scale and cascades towards smaller scales.

The linewidth difference observed can be estimated from the fitting of the parameter $D$. The $\Delta\sigma^2$ predicted by the VCS fitting is $D/2 = 1.00 \pm 0.675 km^2 s^{-2}$. It is remarkable that this result resembles the $\Delta\sigma^2$ we obtained from the Gaussian profile fitting in the previous section.

In addition to deriving the spectral index, B-field strength can also be estimated with the knowledge of the decoupling scale $L_{AD}$ and the struture function $D_z(r)$ by the rearranged equation 3.4:

$$B = (\frac{L_{AD}}{0.5mpc})^{\frac{1}{2}}(\frac{V_n}{1kms^{-1}})^{\frac{1}{2}}(\frac{n_n}{10^6 cm^{-3}})(\frac{\xi_i}{10^{-7}})^{\frac{1}{2}} mG \qquad (3.17)$$

$V_n$ is the velocity dispersion that corresponds to eddies at the TAD scale $L_{AD}$. $n_n$ is the number density of neutrals. And $\xi_i$

is the ionization fraction. $V_n$ can be estimated by approximating the spread of eddies in spectral space as the full width half maximum of a Gaussian Function:

$$V^2(L) \approx E(k)\Delta k \approx E(k)\frac{\sqrt{8ln2}}{L} \tag{3.18}$$

The energy spectrum can be derived with the best fit obtained from VCS fitting by noticing:

$$E(k) = -\frac{d\sigma^2}{dk} = \frac{l^2}{2\pi}\frac{d}{dl}\sigma^2 \tag{3.19}$$

This gives $V(L_{AD}) \sim 0.84 \pm 0.36\, kms^{-1}$. Recent analyses on filaments in NGC 6334 was performed by André et al. (2016) with the use of a combination of multiwavelength dust continuum measurement. They estimated a column density of $0.7 - 1 \times 10^{23} cm^{-2}$ for this particular filaments that we are mapping. Assuming the line of sight scale is comparable to the width of the filament which is approximately 1.5 pc, this gives an average density $n(H_2) \approx (1.84 \pm 0.32) \times 10^4\, cm^{-3}$. For $n_n \approx 10^4\, cm^{-3}$, the ionization fraction is approximately $10^{-7}$ Draine (2011) for an assumed cosmic ray ionization rate of $\approx 10^{-16}\, s^{-1}$. Plugging these values into the rearranged equation, we arrived at an estimate of B-field strength $0.577 \pm 0.182\, mG$. We compare this estimate with the $B - n$ scaling relation derived by Li et al. (2015), $B = \quad 0.19(\frac{n}{10^3 cm^{-3}})^{0.41}\, mG$. For a number density of

$n \sim 1.84 \times 10^4\, cm^{-3}$, it predicts a B-field strength of $0.627\, mG$ which is close to our independent estimate.

## 3.5 Discussion

### 3.5.1 Self-absorption and Optical Depths

Signs of self-absoprtion is apparent towards the high density region (I/IN). One might wonder if the gaussian fitting of the spectral line wing would faithfully recover the intrinsic linewidth/ turbulence level at the region. We try to mimic the spectral lines with a simple model and see how reliable such fitting could be for heavily self-absorbed lines. The intensity distribution of the emission of a molecular line can be described by the radiative transfer equation Draine (2011).

$$I_\nu = (J_\nu(T_{ex}) - J_\nu(T_{bg})) \cdot (1 - e^{-\tau_\nu}) \tag{3.20}$$

$T_{ex}$ is the excitation temperature of the line, $T_{bg}$ the cosmic microwave background temperature, $\tau_\nu$ is the line opacity at the frequency of $\nu$ and $J_v(T) = \frac{h\nu/k}{\exp(k\nu/kT)-1}$. The opacity of the gas can be written as:

$$\tau_v = \tau_0 \cdot \exp(-\frac{-(v - v_0)^2}{2\sigma^2}) \tag{3.21}$$

with $\tau_0$ being the maximum opacity, $\nu_0$ being the line frequency and $\sigma$ is the velocity dispersion of the gas. With these two

equations, we can predict the resultant line shape for different $\tau_0$.

Line profiles with $\tau_0 = 0.1, 1, 10$ for a fixed $\sigma_0 = 2.0 kms^{-1}$ together with the Gaussian fitting of the line wings are shown in Figure 3.19. When $\tau_0 < 1$, the optically thin limit, the spectral line shape can be well modelled by a Gaussian function. The $\sigma_{fit} = 2.01 kms^{-1}$ recovered in this case is off by only $0.01 kms^{-1}$. This can be understood with the fact that the line wings are optically thinner, thus are less susceptible to the self-absorption. The spectral line starts to deviates from a perfect Gaussian profile and saturate as $\tau_0$ increases. The modelled Gaussian fitting $\sigma_{fit}$ increases as the optical depth increases. When $\tau_0 = 10$, the $\sigma_{fit}$ recovered differs from $\sigma_0$ by $0.15 kms^{-1}$.

Figure 3.20 shows the difference of the $\sigma_{fit}$ and $\sigma_0$ for a range of $\tau_0$. The error of the estimate with Gaussian fitting increases dramatically as $\tau_0$ increases from 0 to $\sim$ 1. It saturates for $\tau_0 \geq 5$ with a difference of $\sim 0.15 kms^{-1}$. For this simple model, the line-broadening effect for optically thick lines cannot explain the observed linewidth difference between $HCN$ and $HCO^+$.

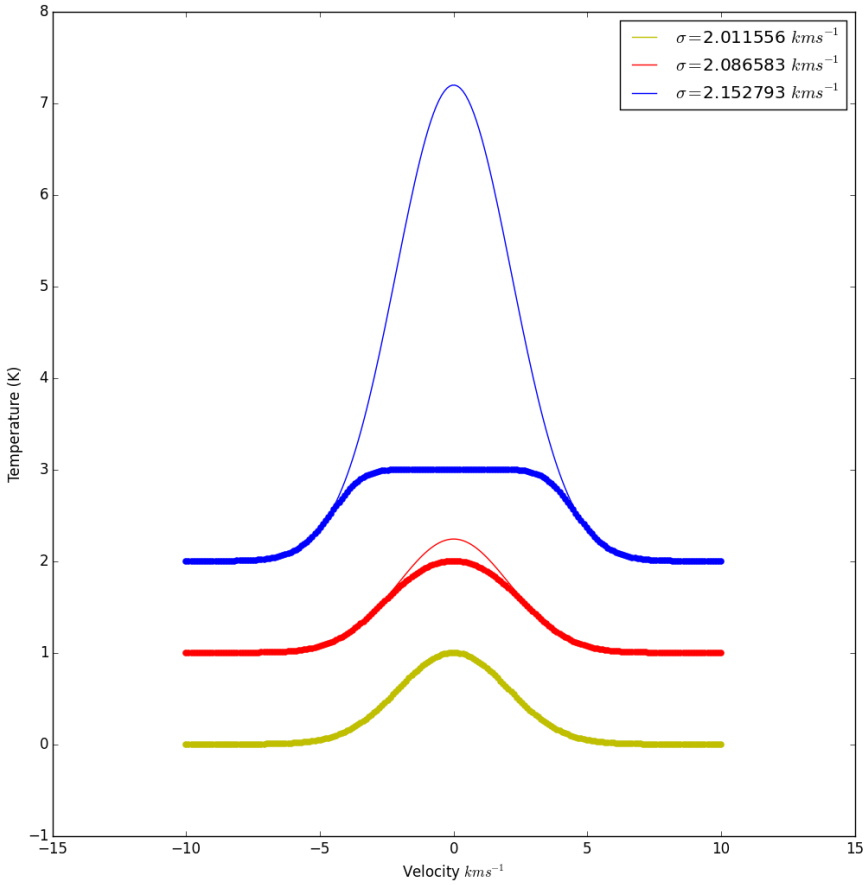


Figure 3.19: The scatter plot shows spectral lines modelled with the radiative transfer equation with typical conditions: $\sigma = 2.0 kms^{-1}$, $T_{ex} = 30K$, for a range of $\tau_0 = 0.1, 1, 10$. The Gaussian profile modelled with the line wings are overlapped on the respective modelled spectral lines.

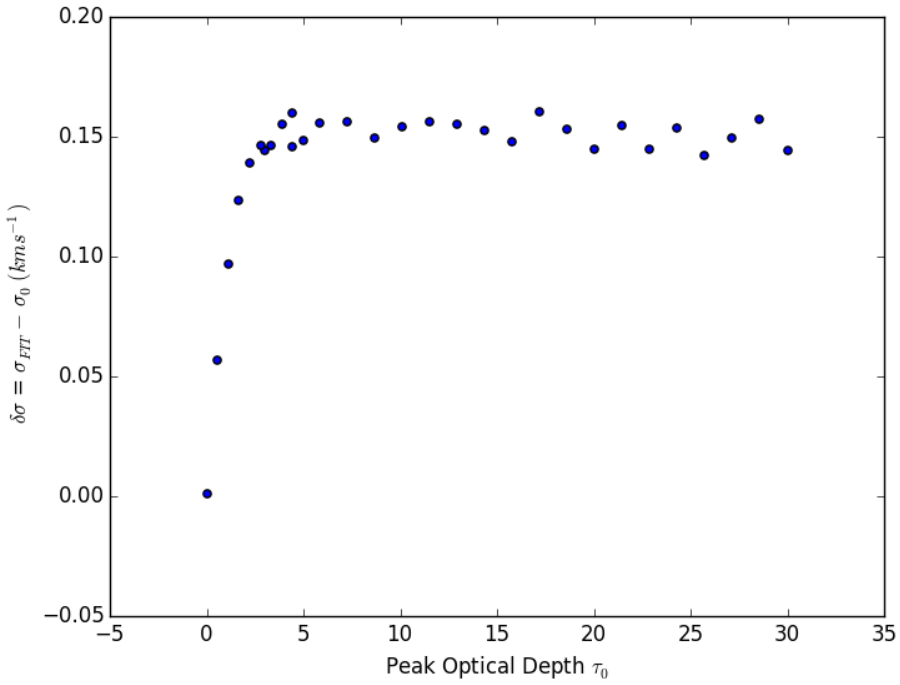


Figure 3.20: The error of $\sigma$ estimate arises from the Gaussian fitting as a function of $\tau_0$

| $F$ | $F'$ | $\Delta f(GHz)$ | Relative intensity of the transitions | $\Delta v(kms^{-1})$ |
|---|---|---|---|---|
| 4 | 4 | -0.001565 | 0.0208 | -1.324 |
| 3 | 2 | -0.000142 | 0.2379 | -0.12 |
| 5 | 4 | 0.000000 | 0.4084 | 0.00 |
| 4 | 3 | 0.000045 | 0.3121 | 0.038 |
| 3 | 4 | 0.000383 | 0.0003 | 0.324 |
| 3 | 3 | 0.001989 | 0.0208 | 1.683 |

Table 3.3: The hyperfines structures of $HCN(4-3)$ transitions. The relative intensity are calculated for the under local thermal equilibrium condition.

### 3.5.2 Hyperfine Structures of HCN

The quadrupole moment induced by the nitrogen atom of HCN is responsible for its widely spaced hyperfine structures. In particular for transitions from rotational level ($J = 4 - 3$), there are 5 transitions based on the calculations of Ahrens et al. 2002. Assuming local thermal equilibrium condition, the two brightest satellite lines are deviated from the main transition by $0.12kms^{-1}$ and $0.038kms^{-1}$ respectively. This offsets cannot account for the observed $\sigma^2$ difference between the two species in NGC 6334 (III) ($\sim 0.4kms^{-1}$). The separation of hyperfine structures is intrinsic to the molecular species and is independent of the external B-field strength. This however cannot produce B-field strength dependent linewidth difference as observed.

The effect of Hyperfine structures on the application of VCS would be addressed here. Assume the main line has the form of $I(v)$, the spectral line with the inclusion of 2 most probable satellite lines can be mimicked by

$$I_{hyper} = \alpha I(v-a) + I(v) + \beta I(v+b) \tag{3.22}$$

where $\alpha$ and $\beta$ are the relative peak intensity of the two satellite lines; $a$ and $b$ are the shift of the hyperfine satellites on the frequency/velocity axis with respect to the main lines. The resultant power spectrum of the spectral lines in the presence of hyperfines would be in the form of:

$$\begin{aligned} P_{hyper}(k_v) = & \quad |\int_{-\infty}^{\infty} I_{hyper}(v) e^{ik_v v} dv|^2 \\ = & \quad [1 + \alpha^2 + \beta^2 + \alpha\cos(k_v a) + \beta\cos(k_v b) \\ & + \alpha\beta\cos(k_v(a+b))] P_{vcs}(k_v) \\ = & \quad h(k_v, \alpha, \beta) P_{vcs}(k_v) \end{aligned} \tag{3.23}$$

The resultant power spectrum has an additional factor which depends on $k_v$.The effect of including this extra factor $h(k_v, \alpha, \beta)$ on the VCS is demonstrated in Figure 3.21. In the $k_v$ range that we are interested in, this additional term barely affects the fitting results for a range of $\alpha$ and $\beta$. Therefore we ignored these parameters in the fitting of HCN.

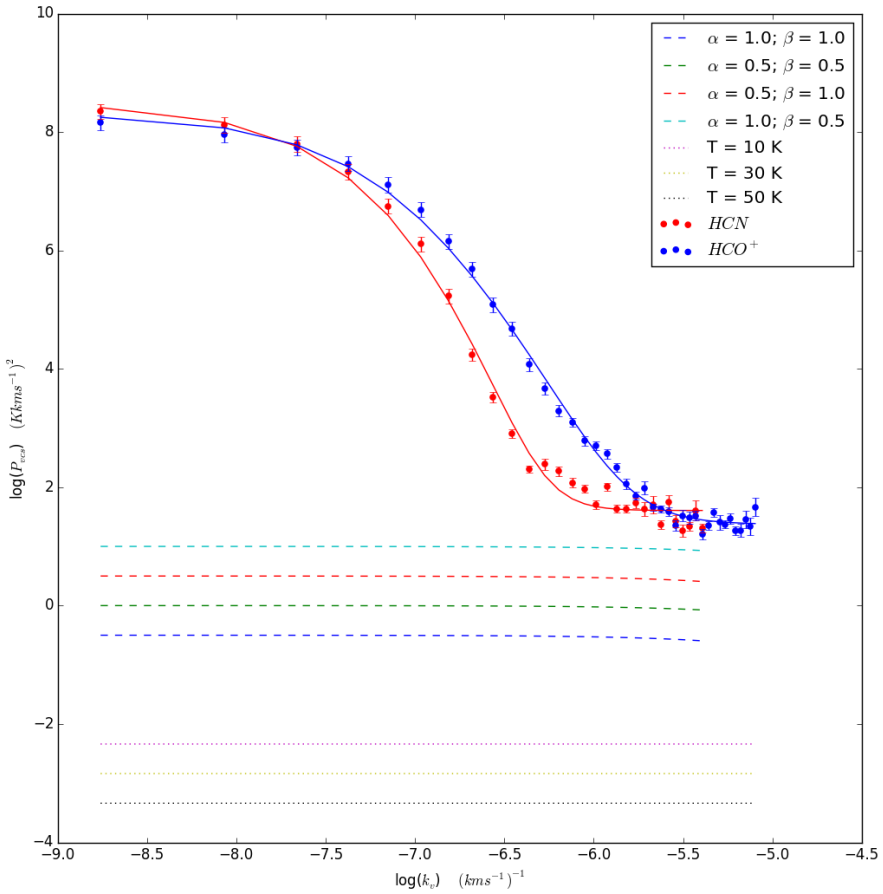


Figure 3.21: The variation of the temperature dependent term $\tilde{f}^2(k_v, T)$ and the prefactor that account for the hyperfine structures $h(k_v, \alpha, \beta)$ with $k_v$. The fitting on VCS would not be affected by the inclusion of these factors.

### 3.5.3 Chemistry of $HCN$ and $HCO^+$

Tassis et al. (2012) studied the chemical evolution of ions and neutrals in prestellar cores and demonstrated the variation of abundance ratio between $HCN/HCO^+$ spans several orders of magnitude in almost all the models with B-fields. In their simulations, they didn't include the effect of turbulence. In the absence of turbulent mixing, the relative abundance should vary to a lesser degree. Worthy to note is $HCO^+$ is shown to be more abundant at larger spatial scale which trace regions with higher levels of turbulence $\Delta\sigma^2 \propto l^n$. In principle it should give rise to a larger linewidth $\Delta$ than the neutral species. It is contrary to observations reported Li et al. (2010), Hezareh et al. (2010), Hezareh et al. (2014). In particular, Tassis et al. (2012) noted that at scales comparable to the size of the cores ($\approx 0.1pc$), the radial dependence of HCN/HCO+ abundance ratio flattens out. Our observation is incapable of resolving the core scale with a beam size of $\sim 0.16pc$ and are thus probing scales where the abundances ratio of $HCN$ and $HCO^+$ are roughly uniform.

The abundances of both $HCN/HCO^+$ are observed to be boosted in the presence of outflows. $HCN$ traces the most energetic outflows while $HCO^+$ generally traces regions close to the base of the outflowsWalker-Smith et al. (2014). The former

is reported to be more enhanced by a factor of $\sim 10-100$ times in the outflow linewings Tafalla et al. (2010). The effect of such enhancement is possibly present in one of our targets NGC 6334 (I). Previous observations (e.g. CO(7-6)/(4-3)/(3-2) emission Leurini et al. (2006)) revealed a bipolar outflows in the NE direction which covers a size of $40''$. The linewidth difference is observed to be amplified greatly towards this direction (Figure 3.12). The enchanced $HCN$ is more sensitive to the high velocity outflow wings than $HCO^+$ see Figure 3.7. This might consquently give rises to the widened linewidth of $HCN$. We therefore didn't include NGC 6334 (I) in our analyses above.

It has been reported that 6334 (IN) also hosts outflows detectable at the scale we are probing, with the mass and the outflow rate an order of magnitude smaller than the one emanating from 6334 (I) Zernickel (2015). This could possibly explain the discrepancy of the behaviour of the $\Delta\sigma^2$ between 6334 (I) and 6334 (IN).

## 3.6 Summary and Future Work

We test the theory of TAD in the massive star-forming filament NGC 6334 where B-field is dynamically dominant. The squared velocity dispersion difference between coexisting ions

and neutrals $\Delta\sigma^2$ is found to be postively correlated with B-field strength. We have also compared the dependence of $\Delta\sigma^2$ with column density from three different regions. We suggest this could be a potential probe of the $B - \rho$ relation. The turbulence spectrum of both ions and neutrals are derived with the new method VCS in the filament NGC 6334 (III). Our best fit parameters has shown ions trace a steeper slope than the neutrals for scales smaller $L_{AD} \sim 0.484pc$. It is a direct observational evidence of turbulent ambipolar diffusion in action. A B-field estimate of $0.577mG$ is derived for NGC 6334 (III).

Further observations would be extremely useful to verify the postulations we posted in this chapter. $H^{13}CN$ and $H^{13}CO^+$ would be needed to constrain the optical depth effect on the broadening of the $\sigma^2$. The thermal dust polarization map from NGC 6334 (III) enables us to verify the $L_{AD}$ derived from this chapter as the straightening of small-scale B-field structures should be expected from the damping of Alfven waves with $\lambda \leq L_{AD}$.

---

□ **End of chapter.**

# Appendix A

# Derivation of Velocity Coordinate Spectrum (VCS)

The Interstellar Medium is turbulent from AUs to kpc scale. Turbulence is of fundamental importance to the understanding of astrophysical process like star formation. This technique, velocity coodinate spectrum (VCS) proposed by Lazarian & Pogosyan (2006), opens us a new window to the studies of turbulent spectrum with the use of Doppler-Broadened emission/absorption lines.

## A.1 Basic Formalism

The spectral line signal measured at velocity $v_z$ at a beam pointing in$\hat{e}$ can be written as:

$$I(\hat{e}, v_z) = \int_0^\infty w(\hat{e}, \vec{r})\rho(\vec{r})\phi_{vz}(\vec{r})d\tilde{\mathbf{r}} \tag{A.1}$$

where $\rho$ is the density distribution function, $v_z$ is the line of sight velocity component, $\phi_{vz}$ denotes the fraction of molecules moving at the line of sight velocity $v_z$ and $w(\vec{r})$ is the window function that accounts for the instrument beam and the extent of structures along the line of sight.

The distribution function $\phi$ can be written as a Maxwellian shifted by the line of sight component of the turbulent velocity

$$\phi_{vz}(\mathbf{x}) = \frac{1}{(2\pi\beta)^{1/2}} \exp(-\frac{(v - v_{rz}(x))^2}{2\beta}) \tag{A.2}$$

where $\beta = k_B T/m$, with $T$, $m$ being the temperature and mass of the molecules respectively.

The correlation fucntion of the Fourier Transform of the spectral lines taken in two different directions is

$$\begin{aligned} K(\hat{e_1}, \hat{e_2}, k_v) &= < \tilde{I}(\hat{e_1}, v)\tilde{I}^*(\hat{e_2}, v) > \\ &= \tilde{\phi_{vz}}^2(k_v) \int w(\hat{e_1}, r)d\mathbf{r} \int w(\hat{e_2}, r')d\mathbf{r}' \\ &\quad < \rho(r)\rho(r') >< \exp(-ik_v(v_{rz}(r) - v_{r'z'}(r'))) > \end{aligned} \tag{A.3}$$

Assuming the velocity statistics are Gaussian, the ensemble average of the exponent can be written as

$$\begin{aligned} &< \exp(-ik_v(v_{rz}(r) - v_{r'z'}(r'))) > \\ &= \exp(-\frac{k_v^2}{2} < (v_{rz}(r) - v_{r'z'}(r'))^2 >) \\ &= \exp(-\frac{k_v^2}{2} D_{vz}(r - r')) \end{aligned} \tag{A.4}$$

where $D_{vz}$ is the structure function of turbulent velocity along the line-of-sight. For self-similar turbulent motion, the structure function can be written as $D_z \sim D(L)(r/L)^m$ where $D_z(L)$ and $L$ are the injection scale and variance of velocity of the turbulence at $L$. e.g. The scaling exponent $m = 2/3$ for Kolmogorov turbulence.

As most of the terms in the equation depends only on relative seperation $r - r'$, the expression can be further simplified with a transformation with $r$ and $r'$:

$$\begin{aligned} K(\hat{e_1}, \hat{e_2}, k_v) = &< \tilde{I}(\hat{e_1}, v)\tilde{I}^*(\hat{e_2}, v) > \\ =&\tilde{\phi_{vz}}^2(k_v) \int g(\hat{e_1}, \hat{e_2}, r) d\mathbf{r} \\ &C_\epsilon(r) \exp(-\frac{k_v^2}{2} D_{vz}(r - r')) \end{aligned} \tag{A.5}$$

where $C_\epsilon(r)$ is defined to be the correlation function of the density field. This correlation function consist of two parts: a constant part that depends on the mean density; a part that varies with $r$. For power-law like density spectrum, the correlation

fucntion can be written as $C_\epsilon(r) =< \rho >^2 (1+(r_0/r)^\gamma)$ Lazarian & Pogosyan (2006).

The geometric factor is given by:

$$g(\hat{e_1}, \hat{e_2}, r) = \int w(\hat{e_1}, r')w(\hat{e_2}, r'+r)d\mathbf{r}' \tag{A.6}$$

Chepurnov et al. (2010) showed that $g(r)$ can be expressed as

$$\begin{aligned} g(r) =& \frac{1}{\pi\theta_0^2}\int_0^\infty \frac{w(z')w(z'+|z|)}{z'^2+(z'+|z|)^2} \\ & \cdot \exp(-\frac{R^2}{\theta_0^2(z'^2+(z'+|z|)^2)})dz' \end{aligned} \tag{A.7}$$

to account for overlapping line-of-sight of a Gaussian Beam with resolution $\theta_0$

When we take $\hat{e}_1 = \hat{e}_2$, we arrive at the analytical form of the VCS technique:

$$\begin{aligned} P_{vcs}(k_v) =& K(\hat{e_1}, \hat{e_1}, k_v) \\ =& \tilde{\phi_{vz}}^2(k_v) \int g(r)d\mathbf{r} \\ & \cdot C_\epsilon(r)\exp(-\frac{k_v^2}{2}D_{vz}(r)) \end{aligned} \tag{A.8}$$

In the detailed analysis by LP06, for steep density spectrum ($\gamma < 0$), the density correlation term $C_\epsilon(r)$ has a weak logarithmic dependece on $r$ and can be factored out from the integrand. Based on the prediction of Velocity Channel Analysis (Lazarian & Pogosyan (2000)), this index can be inferred from

the 2D spatial power spectrum of the column density map:

$$P_{2D}(K) \sim K^{-3+\gamma} \tag{A.9}$$

In the regime where thermal velocity is small compared to the velocity scale that we are interested in and density spectrum is steep, the resultant VCS can be simplified as:

$$P_{vcs}(k_v) = P_0 \int g(r) d\mathbf{r} \exp(-\frac{k_v^2}{2} D_{vz}(r)) + N_0 \tag{A.10}$$

where $P_0$ is the amplitude of the spectrum and $N_0$ is a constant to account for the noise in the observational data.

---

□ **End of chapter.**

# Bibliography

Andersson, B.-G., Lazarian, A., & Vaillancourt, J. E. 2015, ARA&A, 53, 501

André, P., Revéret, V., Könyves, V., et al. 2016, ArXiv e-prints, arXiv:1605.07434

Balsara, D. S. 1996, ApJ, 465, 775

Burkhart, B., Lazarian, A., Balsara, D., Meyer, C., & Cho, J. 2015, ApJ, 805, 118

Chandrasekhar, S., & Fermi, E. 1953, ApJ, 118, 113

Chepurnov, A., Burkhart, B., Lazarian, A., & Stanimirovic, S. 2015, apj, 810, 33

Chepurnov, A., & Lazarian, A. 2009, apj, 693, 1074

Chepurnov, A., Lazarian, A., Stanimirović, S., Heiles, C., & Peek, J. E. G. 2010, Apj, 714, 1398

Cho, J., & Lazarian, A. 2003, MNRAS, 345, 325

Crutcher, R. M., Wandelt, B., Heiles, C., Falgarone, E., & Troland, T. H. 2010, ApJ, 725, 466

Dolginov, A. Z., & Mitrofanov, I. G. 1976, Apss, 43, 291

Draine, B. T. 2011, Physics of the Interstellar and Intergalactic Medium

Falceta-Gonçalves, D., Lazarian, A., & Kowal, G. 2008, ApJ, 679, 537

Girart, J. M., Rao, R., & Marrone, D. P. 2006, Science, 313, 812

Goldreich, P., & Sridhar, S. 1995, ApJ, 438, 763

Gonçalves, J., Galli, D., & Walmsley, M. 2005, AAP, 430, 979

Hezareh, T., Csengeri, T., Houde, M., Herpin, F., & Bontemps, S. 2014, mnras, 438, 663

Hezareh, T., Houde, M., McCoey, C., & Li, H.-b. 2010, apj, 720, 603

Hildebrand, R. H., Dotson, J. L., Dowell, C. D., Schleuning, D. A., & Vaillancourt, J. E. 1999, ApJ, 516, 834

Houde, M., Bastien, P., Peng, R., Phillips, T. G., & Yoshida, H. 2000, ApJ, 536, 857

Hull, C. L. H., Plambeck, R. L., Kwon, W., et al. 2014, ApJs, 213, 13

Kataoka, A., Machida, M. N., & Tomisaka, K. 2012, ApJ, 761, 40

Kolmogorov, A. 1941, Akademiia Nauk SSSR Doklady, 30, 301

Larson, R. B. 1981, MNRAS, 194, 809

Lazarian, A. 2007, JQSRT, 106, 225

Lazarian, A. 2009, in Astronomical Society of the Pacific Conference Series, Vol. 414, Cosmic Dust - Near and Far, ed. T. Henning, E. Grün, & J. Steinacker, 482

Lazarian, A., & Hoang, T. 2007, MNRAS, 378, 910

Lazarian, A., & Pogosyan, D. 2000, ApJ, 537, 720

—. 2006, apj, 652, 1348

Leurini, S., Schilke, P., Parise, B., et al. 2006, AAP, 454, L83

Li, H.-b., Dowell, C. D., Goodman, A., Hildebrand, R., & Novak, G. 2009a, apj, 704, 891

—. 2009b, ApJ, 704, 891

Li, H.-b., & Houde, M. 2008, Apj, 677, 1151

Li, H.-b., Houde, M., Lai, S.-p., & Sridharan, T. K. 2010, apj, 718, 905

Li, H.-B., Yuen, K. H., Otto, F., et al. 2015, nat, 520, 518

Liu, H. B., Qiu, K., Zhang, Q., Girart, J. M., & Ho, P. T. P. 2013, ApJ, 771, 71

Lo, N., Cunningham, M. R., Jones, P. A., et al. 2009, MNRAS, 395, 1021

Matthews, B. C., Lai, S.-P., Crutcher, R. M., & Wilson, C. D. 2005, ApJ, 626, 959

Matthews, B. C., McPhee, C. A., Fissel, L. M., & Curran, R. L. 2009, ApJs, 182, 143

McKee, C. F., & Ostriker, E. C. 2007, ARA&A, 45, 565

Mestel, L., & Spitzer, Jr., L. 1956, MNRAS, 116, 503

Murray, N., & Rahman, M. 2010, ApJ, 709, 424

Nakano, T., & Nakamura, T. 1978, PASJ, 30, 671

Ostriker, E. C., Stone, J. M., & Gammie, C. F. 2001, apj, 546, 980

Padoan, P., Goodman, A., Draine, B. T., et al. 2001, ApJ, 559, 1005

Padoan, P., Juvela, M., Kritsuk, A., & Norman, M. L. 2009, apjl, 707, L153

Purcell, E. M. 1979, ApJ, 231, 404

Sawada, T., Ikeda, N., Sunada, K., et al. 2008, PASJ, 60, 445

Stephens, I. W., Looney, L. W., Dowell, C. D., Vaillancourt, J. E., & Tassis, K. 2011, ApJ, 728, 99

Tafalla, M., Santiago-García, J., Hacar, A., & Bachiller, R. 2010, AAP, 522, A91

Tassis, K., Hezareh, T., & Willacy, K. 2012, ApJ, 760, 57

Tassis, K., & Mouschovias, T. C. 2004, ApJ, 616, 283

Tilley, D. A., & Balsara, D. S. 2010, MNRAS, 406, 1201

Vaillancourt, J. E. 2002, ApJs, 142, 53

Vaillancourt, J. E., & Matthews, B. C. 2012, ApJs, 201, 13

Vrba, F. J., Coyne, G. V., & Tapia, S. 1993, Aj, 105, 1010

Walker-Smith, S. L., Richer, J. S., Buckle, J. V., Hatchell, J., & Drabek-Maunder, E. 2014, MNRAS, 440, 3568

Xu, S., Lazarian, A., & Yan, H. 2015, ApJ, 810, 44

Zernickel, A. 2015, PhD thesis, I.Physikalisches Institut der Universitat zu Köln, Zülpicher Straße 77, 50937, Köln, Germany

Zweibel, E. G. 2015, in Astrophysics and Space Science Library, Vol. 407, Magnetic Fields in Diffuse Media, ed. A. Lazarian, E. M. de Gouveia Dal Pino, & C. Melioli, 285